

**APPLIED PHYSICS REVIEWS****A critical literature review of focused electron beam induced deposition**W. F. van Dorp<sup>a)</sup> and C. W. Hagen*Faculty of Applied Sciences, Delft University of Technology, Lorentzweg 1, 2628 CJ Delft, The Netherlands*

(Received 6 March 2008; accepted 11 August 2008; published online 17 October 2008)

An extensive review is given of the results from literature on electron beam induced deposition. Electron beam induced deposition is a complex process, where many and often mutually dependent factors are involved. The process has been studied by many over many years in many different experimental setups, so it is not surprising that there is a great variety of experimental results. To come to a better understanding of the process, it is important to see to which extent the experimental results are consistent with each other and with the existing model. All results from literature were categorized by sorting the data according to the specific parameter that was varied (current density, acceleration voltage, scan patterns, etc.). Each of these parameters can have an effect on the final deposit properties, such as the physical dimensions, the composition, the morphology, or the conductivity. For each parameter-property combination, the available data are discussed and (as far as possible) interpreted. By combining models for electron scattering in a solid, two different growth regimes, and electron beam induced heating, the majority of the experimental results were explained qualitatively. This indicates that the physical processes are well understood, although quantitatively speaking the models can still be improved. The review makes clear that several major issues remain. One issue encountered when interpreting results from literature is the lack of data. Often, important parameters (such as the local precursor pressure) are not reported, which can complicate interpretation of the results. Another issue is the fact that the cross section for electron induced dissociation is unknown. In a number of cases, a correlation between the vertical growth rate and the secondary electron yield was found, which suggests that the secondary electrons dominate the dissociation rather than the primary electrons. Conclusive evidence for this hypothesis has not been found. Finally, there is a limited understanding of the mechanism of electron induced precursor dissociation. In many cases, the deposit composition is not directly dependent on the stoichiometric composition of the precursor and the electron induced decomposition paths can be very different from those expected from calculations or thermal decomposition. The dissociation mechanism is one of the key factors determining the purity of the deposits and a better understanding of this process will help develop electron beam induced deposition into a viable nanofabrication technique. © 2008 American Institute of Physics. [DOI: 10.1063/1.2977587]

**TABLE OF CONTENTS**

I. INTRODUCTION.....	2	2. Width.....	10
II. FOCUSED ELECTRON BEAM INDUCED PROCESSES IN GENERAL.....	3	3. Composition and morphology.....	12
A. Substrate-precursor molecule interaction....	3	4. Density.....	13
B. Electron-substrate interaction.....	4	5. Conductivity.....	14
C. Electron-precursor molecule interaction....	4	B. Electron energy.....	15
D. Interplay between factors.....	5	1. Height and width.....	15
III. THEORETICAL MODEL.....	6	2. Composition and morphology.....	17
A. Basic model.....	6	3. Conductivity.....	17
B. Electron- and precursor-limited regimes....	6	C. Conclusions.....	17
C. Temperature.....	7	V. SCAN PATTERN AND SCAN STRATEGY.....	18
IV. BEAM PARAMETERS.....	8	A. Scan pattern.....	18
A. Current density.....	8	1. Height and width.....	18
1. Height.....	8	2. Composition and morphology.....	19
		B. Scan strategy.....	20
		1. Height and width.....	20
		2. Conductivity.....	21
		C. Scan speed.....	21
		D. Writing direction.....	22

<sup>a)</sup>Electronic mail: w.f.vandorp@tudelft.nl.

1. Height.....	22
2. Composition and morphology.....	23
E. Proximity effects.....	23
1. Deposit location.....	23
2. Composition and resistivity.....	26
F. Conclusions.....	27
VI. ADDITIONAL CIRCUMSTANCES.....	27
A. During experiments.....	27
1. Substrate heating.....	27
a. Height and width.....	27
b. Composition and morphology.....	28
c. Conductivity.....	29
2. Tilting during deposition.....	29
3. Biasing sample during deposition.....	29
B. Postdeposition treatment.....	29
1. Extra irradiation.....	29
2. Annealing.....	30
a. Composition.....	30
b. Conductivity.....	30
C. Conclusions.....	31
VII. SUBSTRATE.....	31
VIII. PRECURSOR.....	33
A. Introduction.....	33
B. Precursor gas only.....	33
C. Reactive gases.....	35
D. Precursor pressure.....	36
E. Conclusions.....	36
IX. CONCLUSIONS.....	37
APPENDIX.....	38

## I. INTRODUCTION

Focused electron beam induced deposition (EBID) is a lithography technique that allows the definition of patterns on a substrate using electron beams (e-beams). By scanning a focused e-beam over the sample in the presence of a precursor gas, the pattern is defined directly and (in principle) no pre- or postprocessing is required. It is mostly performed in electron microscopes, so direct *in situ* inspection of the fabricated structure is very easy. Since e-beams can be focused into spots with diameters varying from micrometers down to the subangstrom level, this direct-write process is suitable for

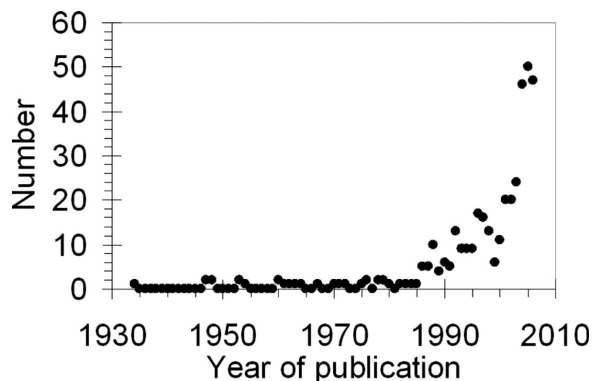


FIG. 1. Number of publications as a function of the year of publication. Since the first mention of contamination growth in 1934, FEBIP gained increasing interest since the end of the 1980s.

the micro- and nanometer regimes. Apart from deposition, the e-beam can also be used to induce other effects such as local etching or heating. Together, these processes are members of a family known as focused e-beam induced processing (FEBIP).

FEBIP is a lithography technique that has been around for many decades now, the first reports on the topic coming from Steward<sup>1</sup> in 1934. He found contamination growth in his electron optical system. While he considered the deposits as a “very insidious and prevalent source of errors,” something that clearly needed to be avoided, Christy<sup>2</sup> and Baker and Morris<sup>3</sup> were among the first to see a potentially useful side of the technique and deposited conducting films. In recent years, FEBIP is a field of growing interest (see Fig. 1).

Precursors used in FEBIP are contamination (carbon species from the residual gas in the electron optical system), metal-organic precursors [for instance,  $W(CO)_6$  or trimethylplatinum-cyclopentadienyl ( $Me_3PtCp$ )], or inorganic precursors (for instance,  $WF_6$  or  $XeF_2$ ). Typical examples of deposits are shown in Fig. 2. One of the major advantages of beam induced processing is that the pattern can be defined on flat [Fig. 2(a)] as well as topographical surfaces [Fig. 2(b)].<sup>4</sup> As long as it is possible to focus the e-beam properly on the sample, deposition or etching can be performed. Another advantage is that the fabrication of three-dimensional (3D) structures is possible. Regarding EBID, disadvantages are

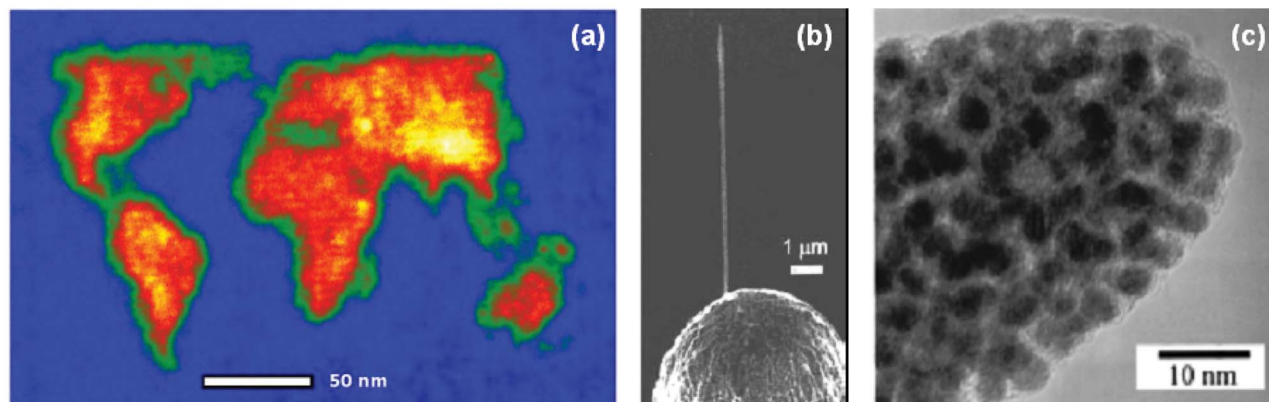


FIG. 2. (Color online) Typical examples of beam induced deposits. (a) A topographical map of the world on a flat substrate. Note the presence of the Himalayas, the Rocky Mountains, and the Andes. (b) A tip grown on a scanning tunneling microscopy probe. From Ref. 4. Copyright © 1992 by Elsevier. Reprinted by permission of Elsevier. (c) High-resolution TEM image of a typical deposit showing a nanocomposite material (nanometer-sized metal crystals in an  $\alpha$ -C matrix). From Ref. 5.

the low growth rates compared to other lithography techniques such as e-beam lithography and the deposit composition. The typical deposit created from metal-organic precursors consists of a nanocomposite material: metal crystals of a few nanometers in size embedded in a matrix of amorphous carbon (*a*-C). See also Fig. 2(c).<sup>5</sup> Such deposits contain around 10% metal and the other 90% is carbon and other elements originally contained in the precursor molecule. Inorganic precursors, especially the fluorine-based precursors, tend to yield deposits with higher metal concentrations.

In the course of time, many applications have been developed. Examples are probes (functionalized tips for scanning probe microscopy or for local conductivity measurements),<sup>6–14</sup> conducting or nonconducting joining technique,<sup>15–20</sup> conducting wires,<sup>21–24</sup> mask repair,<sup>25–27</sup> electron sources,<sup>28–30</sup> micro-Hall and micro superconducting quantum interference devices,<sup>31,32</sup> nanotweezers and gripping devices,<sup>33,34</sup> nano-optic patterns or photonic crystals,<sup>35,36</sup> entire miniature electron optical systems,<sup>37</sup> diodes,<sup>38</sup> and seeds for nanotube growth.<sup>39</sup>

Despite its long history, detailed knowledge of the process is still very much dispersed. Not only “a plethora of materials” has been studied, as Randolph *et al.*<sup>40</sup> put it, but the entire collection of publications on FEBIP can be described as a plethora of results. The fact that the deposition member of the FEBIP family is known under many names perfectly illustrates this unhelpful situation: EBID, e-beam induced resist, e-beam induced metal formation, e-beam assisted deposition, e-beam induced selective etching and deposition, e-beam induced chemical vapor deposition (CVD), e-beam stimulated deposition, e-beam induced surface reaction, e-beam writing, environmental e-beam deposition, e-beam assisted direct-write nanolithography, contamination lithography, additive lithography, or 3D deposition lithography.

Since FEBIP is a very complex phenomenon, it is important to have an overview of all available useful results that is as complete as possible. This is not the first review on FEBIP: reviews by Silvis-Cividjian and Hagen<sup>41</sup> and Randolph *et al.*<sup>42</sup> appeared earlier and summarized published results and achievements. It is felt that there is a need for a more critical review, in which it is determined to which extent the available models for FEBIP are valid and complete. To do this, it is important to compare as many results as possible and try to recognize the major trends. This overview is an attempt at such a study. Out of the approximately 400 articles that have appeared on FEBIP, we have selected nearly 200 articles. The results from these articles have been sorted and interpreted as far as possible using a model that is presented. We do not claim to be fully complete, but we have tried to make this overview extensive. Since deposition is the most studied member of the FEBIP family, we restrict ourselves to EBID. For a good review on e-beam induced etching, we refer the reader to Ref. 42.

This review serves three purposes: (1) To collect and summarize relevant information from available literature, (2) to interpret this information and, where possible, compare to available (qualitative) models, and (3) to suggest strategies for further research into EBID.

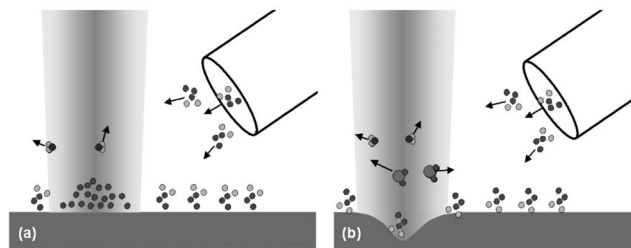


FIG. 3. A schematic drawing of (a) beam induced deposition and (b) etching. From Utke.

The review is organized as follows. After giving a short introduction in Sec. II on the various parameters that are important for the process, we discuss the effect of each of the parameters that can be varied in the deposition process: the e-beam (Sec. III), the scan pattern and the scan strategy (Sec. IV), additional circumstances, such as heating of the substrate during or after deposition (Sec. V), the substrate (Sec. VI), and finally the precursor (Sec. VII). We discuss the reported influence of these parameters on relevant properties of the deposition process and, if possible, we suggest a qualitative model. An explanation of the precursor names, the symbols, and the abbreviations that are used in this article are presented in the Appendix. Conclusions from all described results and an outlook for further work are presented in Sec. IX.

## II. FOCUSED ELECTRON BEAM INDUCED PROCESSES IN GENERAL

The basic principle of FEBIP is quite simple. Gas molecules (most commonly metal-organic molecules) are adsorbed on a substrate. Under the influence of the e-beam, the precursor molecules are dissociated into volatile and nonvolatile components. Depending on the type of precursor, the nonvolatile components adhere to the substrate and form a deposit (in the case of deposition) or react with the substrate and form volatile species (in the case of etching). Hence, a structure is grown [Fig. 3(a)] or the substrate is etched [Fig. 3(b)]. This beam induced reaction occurs only locally at or around the irradiated area. We now will go into more detail by describing the most important interactions playing a role in FEBIP.

### A. Substrate–precursor molecule interaction

The many different interactions complicate matters quite severely. To begin with, there are the interactions between the substrate and precursor molecules, such as diffusion, adsorption, and desorption. Adsorption of the precursor molecule may occur as chemisorption or physisorption depending on the combination of precursor, substrate, and temperature. The residence time  $\tau$  of the precursor molecule on the substrate also can affect beam induced processes. A longer  $\tau$  gives a higher probability of dissociation by the incoming or emitted electrons. Taking into account that the majority of the FEBIP experiments are done under non-UHV conditions, the precise condition of the vacuum and the substrate surface is generally unknown. Furthermore, as soon as the deposition process starts in the case of deposition, the

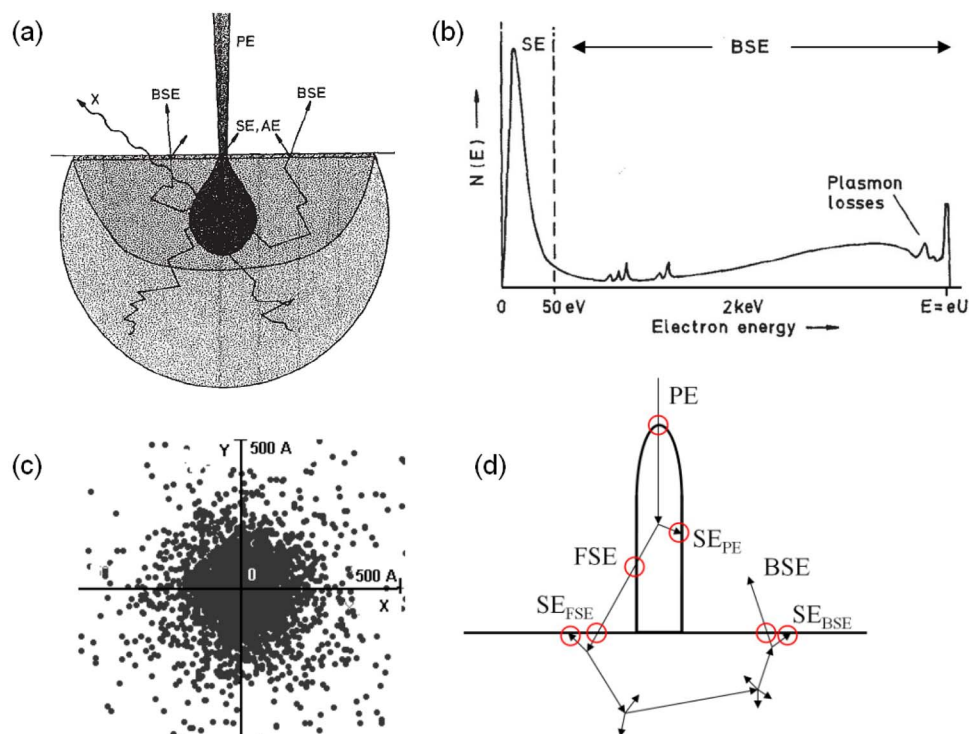


FIG. 4. (Color online) (a) A schematic of the electron scattering volume in a flat substrate (from Ref. 43). (b) A typical energy spectrum of electrons emitted from the substrate (from Ref. 43). The PE energy is equal to  $eU$ . (c) Top view of (simulated) SE emission sites on a flat substrate, showing the spatial distribution. From Ref. 44. (d) In the case of a growing 3D deposit, electrons can cross the target-vacuum interface in many different ways. For tips longer than the BSE range, the electron scattering volume will be more confined to the tip. Copyright © 1998 by Springer-Verlag. Reprinted with permission by Springer-Verlag.

interface of interest changes from the substrate surface to the deposit surface. This transition stage is specifically important for the fabrication of high-resolution structures, where the growth is stopped in or soon after the nucleation stage of the deposit.

## B. Electron-substrate interaction

Then there are the interactions between the e-beam and substrate. At the start of the FEBIP experiment, a beam of electrons [primary electrons (PEs)] is focused onto a clean substrate. In a simplified picture, the PEs collide with the solid and are deflected from their original trajectory. If an inelastic collision occurs, part of the initial energy can be transferred from the PE to other electrons in the solid. These electrons will in turn interact with the solid and scatter. The newly generated electrons are called secondary electrons (SEs) if their energy upon leaving the substrate is smaller than 50 eV and backscattered electrons (BSEs) if their energy is larger than 50 eV.

The average length these electrons travel between two collisions (the mean free path) is dependent on their energy. As a result of all these collisions, there is a (sort of onion shaped) volume of scattering events in the solid below the irradiated spot [Fig. 4(a)].<sup>43</sup> The shape and the size of this volume depend on the PE energy and the substrate. From this volume, SEs and BSEs can escape from the substrate and enter into the vacuum. So on the substrate surface, around the irradiated spot, there is an energy spectrum [Fig. 4(b)] and a spatial distribution [Fig. 4(c)]<sup>44</sup> of emitted electrons. Monte Carlo simulations have been developed to model this process.<sup>45–48</sup> Precursor molecule dissociation can occur every time an electron crosses the interface between the substrate and vacuum.

Matters become more complicated by the fact that the shape and often the composition of the target change during the FEBIP experiment. In the case of beam induced deposition, for instance, a pillar can grow and the electron scattering volume will become more confined to the pillar as it becomes longer. Electrons [for instance, forward scattered electrons (FSEs)] can also cross the target-vacuum interface several times [Fig. 4(d)]. As a result of the electron scattering, there is a constant energy transfer from the PEs to the substrate and/or the growing structure, which may lead to e-beam induced heating. Furthermore, if the target is electrically nonconducting, a difference between the fluxes of in-bound PEs and outbound SEs and BSEs can lead to charging of the sample. Finally, when the PE energy is around 50 keV or larger, physical sputtering of the target material by the high-energy PEs can occur.<sup>49</sup> This is especially relevant for FEBIP experiments in (scanning) transmission electron microscopes [(S)TEMs], where the acceleration voltage is usually 200–300 keV.

## C. Electron-precursor molecule interaction

Finally, there is the interaction between the electrons and the precursor molecules. Dissociation is the most important one for this review, but e-beam stimulated desorption also can occur. The probability that an electron induces the scission of a bond in a precursor molecule depends on the electron energy and is generally expressed as a cross section  $\sigma(E)$  ( $\text{cm}^2$ ). The larger the cross section, the larger the probability that a bond in the molecule is broken. The cross section for dissociation of adsorbed molecules is a difficult issue since it depends on many parameters. It depends, for instance, on the energy of the bonds within the molecule and is strongly influenced by the environment, the available reaction paths for

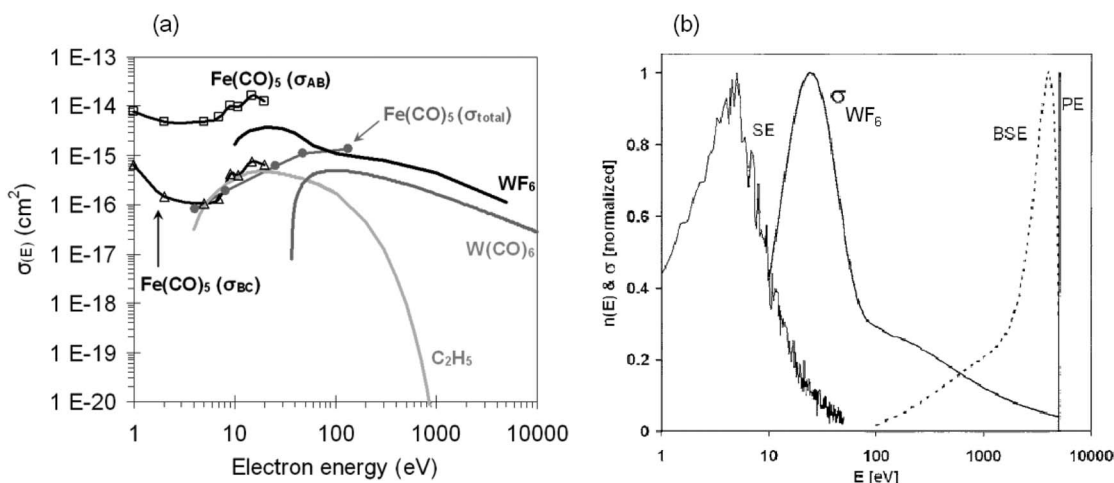


FIG. 5. (a) Measured and estimated cross sections for the dissociation of precursors often used in EBID. Cross sections for  $\text{Fe}(\text{CO})_5$  are reported by Rowntree ( $\sigma_{AB}$  and  $\sigma_{BC}$ ) (Ref. 54) and Henderson *et al.* ( $\sigma_{\text{total}}$ ) (Ref. 55). In Monte Carlo simulations, cross section for  $\text{C}_2\text{H}_5$  (Silvis-Cividjian *et al.*, Ref. 56),  $\text{WF}_6$  (Fowlkes *et al.*, Ref. 57), and  $\text{W}(\text{CO})_6$  (Mitsubishi *et al.*, Ref. 58) were used. (b) The simulated energy distribution of SEs and BSEs emitted from a Ge substrate and the estimated cross section for the dissociation of  $\text{WF}_6$  as a function of electron energy. All distributions are normalized. From Ref. 58.

the dissociation event, or even the specific geometry in which the molecule is adsorbed. Studies on the interaction between adsorbed molecules and low-energy electrons show that dissociative electron attachment (DEA) and dipolar dissociation (DD) are important processes.<sup>50</sup> Energies as low as a few eV can be sufficient to induce the scission of bonds in precursor molecules, such as for hydrocarbons present on a contaminated sample<sup>51</sup> and hexafluoro-acetylacetonate copper vinyl-trimethyl-silane (hfac-Cu-VTMS).<sup>52</sup> George and Beauchamp<sup>53</sup> used broad area UV irradiation to induce precursor decomposition and found that the yield was primarily dependent on the photoelectron yield of the substrate. There was no deposition when the photon energy was below the photoelectron emission threshold. In Fig. 5(a), three cross sections for low-energy electron induced dissociation are plotted for  $\text{Fe}(\text{CO})_5$ . Rowntree reported  $\sigma_{AB}$  and  $\sigma_{BC}$ , cross sections for a two-step dissociation, from the original  $\text{Fe}(\text{CO})_5$  molecule (A) into an intermediate species (B) and from B into the final material that remains after prolonged irradiation (C).<sup>54</sup> Henderson *et al.*<sup>55</sup> measured  $\sigma_{\text{total}}$ , the total cross section for the dissociation of a monolayer of adsorbed  $\text{Fe}(\text{CO})_5$ .

These studies clearly indicate that low-energy electrons (i.e., SEs) are relevant for the deposition process. However, they do not exclude the possibility that electrons with a higher energy can also contribute to the growth. This can be, for instance, by dissociative ionization (DI), which typically has a cross section (measured for molecules in the gas phase) with a peak at around 100 eV and decreases with increasing electron energy.<sup>59</sup>

The mentioned dissociation mechanisms (DEA, DD, and DI) have cross sections that have their maximum well below 1 keV. One may be tempted to conclude from this that the deposit growth is determined by electrons with energies <1 keV, but that could be premature. In the typical FEBIP experiment, the current density of >1 keV electrons in the area directly under the PE beam is very high compared to the current density of low-energy electrons. That means that, al-

though the absolute cross sections for high-energy electrons may be small, the absolute number may be high enough to make their contribution to deposit growth significant [see Fig. 5(b)]. Definite conclusions cannot be drawn since there is little information on the balance between the contributions of low- and high-energy electrons to the dissociation of adsorbed molecules.

As a result, there is no consensus yet on this particular topic in the field of FEBIP research. The lack of information becomes most evident in the different Monte Carlo simulations that have been developed to model the deposit growth. In these simulations, a dissociation cross section has to be assumed. Silvis-Cividjian *et al.*<sup>56</sup> concentrated on the effect of electrons with energies <1 keV, while Fowlkes *et al.*<sup>57</sup> took a more even balance between low- and high-energy electrons. Mitsubishi *et al.*<sup>58</sup> on the other hand used a cross section where the low-energy cutoff was set at 35.5 eV. The three cross sections are plotted in Fig. 5(a).

Apart from influencing the growth rates, it is also conceivable that the different dissociation processes (DEA, DD, and DI) influence the composition of the deposit. It is possible that the dissociation mechanism determines which fragment of the molecule desorbs after electron impact. Ideally, all carrier groups desorb and only the target material [for instance, Fe in the case of  $\text{Fe}(\text{CO})_5$ ] remains in the deposit. In any case, to advance the understanding and modeling of FEBIP, the progress of the study of dissociation processes such as DEA, DD, and DI is very important.

#### D. Interplay between factors

Looking at the three types of interactions discussed in Secs. II A and II C, it appears that there are many factors involved in the deposition process. One can think of the electron flux, the energy spectrum of the electrons that cross the substrate-vacuum interface, the spatial distribution of electron scattering in the irradiated target, the cross section of the precursor as a function of electron energy, the precursor adsorption behavior (physisorption, chemisorption), the precu-

residence time on the substrate, the precursor diffusion (electron stimulated) desorption, the e-beam induced heating, the gas flux, the orientation of the precursor source with respect to the deposition location, the deposit or surface geometry, the chemical reaction paths that are available, the background gas pressure and composition, or the thermal and electrical conductances of the substrate and deposit. All of these factors act simultaneously and many of them only locally in or around the irradiated area. The factors are not independent of each other and, since the shape of the irradiated target evolves during the process, the dependence is not constant. Furthermore, as if matters were not complex enough, most of the FEBIP experiments are performed under non-UHV conditions, so often quite a number of factors during the experiment are unknown and/or uncontrolled. The interplay between all these factors can lead to an immense variety of possible phenomena, of which perhaps only a small part has yet been observed and is reported in this overview.

### III. THEORETICAL MODEL

#### A. Basic model

Before discussing experimental results, it is helpful to see what we can expect based on the description of the process given in Sec. II. Many parameters were mentioned and not all of these parameters can be put into a theoretical model straight away. So to study the effect of some of the parameters, we start with a rather simple model similar to that suggested by Scheuer *et al.*<sup>60</sup> Starting with the precursor molecule coverage  $N$  ( $\text{cm}^{-2}$ ), it will depend on the number of molecules that adsorb from the gas phase, the number of molecules that are decomposed by the e-beam, and the number of molecules that desorb to the gas phase. This gives

$$\frac{dN}{dt} = gF \left( 1 - \frac{N}{N_0} \right) - \sigma(E)NJ - \frac{N}{\tau}, \quad (1)$$

with  $g$  the sticking factor,  $F$  ( $\text{cm}^{-2} \text{s}^{-1}$ ) the gas flux arriving at the substrate,  $N_0$  ( $\text{cm}^{-2}$ ) the available adsorption site density in a monolayer,  $J$  ( $\text{electrons s}^{-1} \text{cm}^{-2}$ ) the current density, and  $\tau$  (s) the residence time of precursor molecules on the surface. Usually, two simplifications are made. As explained in Sec. II C, the cross section for dissociation,  $\sigma_{(E)}$ , is dependent on the electron energy. Since  $\sigma_{(E)}$  is unknown,  $\sigma$  (the integral value of  $\sigma_{(E)}$ ) is used. Furthermore, in reality  $J = J_{\text{PE}} + J_{\text{BSE}} + J_{\text{SE}}$ , where  $J_{\text{PE}}$ ,  $J_{\text{BSE}}$ , and  $J_{\text{SE}}$  are the PE, BSE, and SE current densities, respectively. Since  $J_{\text{BSE}}$  and  $J_{\text{SE}}$  are usually not measured during experiments, it is assumed that  $J = J_{\text{PE}}$ . Steady-state situation for the coverage  $N$  is reached when  $dN/dt = 0$ , which means

$$N = N_0 \left( \frac{\frac{gF}{N_0}}{\frac{gF}{N_0} + \sigma J + \frac{1}{\tau}} \right). \quad (2)$$

If the growth rate  $R$  ( $\text{cm s}^{-1}$ ) is defined as

$$R = V_{\text{molecule}} N \sigma J, \quad (3)$$

with  $V_{\text{molecule}}$  ( $\text{cm}^3$ ) the volume of a deposited molecule, the combination of Eqs. (2) and (3) gives

$$R = V_{\text{molecule}} N_0 \frac{\left( \frac{gF}{N_0} \right) \sigma J}{\left( \frac{gF}{N_0} + \sigma J + \frac{1}{\tau} \right)}. \quad (4)$$

#### B. Electron- and precursor-limited regimes

We will now look at two simplified cases that give us insight into the deposition process. For simplicity, desorption is ignored. Two distinguishing regimes can be defined:  $gF/N_0 \gg \sigma J$  and  $gF/N_0 \ll \sigma J$ . This reduces Eq. (4) to

$$\frac{gF}{N_0} \gg \sigma J, \quad R = V_{\text{molecule}} N_0 \sigma J, \quad (5)$$

$$\frac{gF}{N_0} \ll \sigma J, \quad R = V_{\text{molecule}} gF. \quad (6)$$

In the first regime, the growth is limited by the current density and has become independent of the gas flux. This is defined as the electron-limited (e.l.) regime. In the second regime, the growth is limited by the number of molecules arriving at the irradiated area and has become independent of the current density. This is defined as the precursor-limited (p.l.) regime. The effect of the two different regimes can be large. For a constant area, a change in  $J$  is a change in the time scale at which a specific number of electrons is supplied. This not only affects  $R$  but it can also affect other deposit properties. The ratio of electrons per deposited molecule can change dramatically, which can give different degrees of fragmentation.

Practical reasons for measuring the growth rate are, for instance, to determine the rate of contamination growth in an electron optical system, to find suitable growth conditions for the fabrication of applications, or to study fundamental aspects of the deposition process. We will see in Sec. IV that measurements of the growth rate are presented in different ways in literature. Different units are used: some authors reported  $V_{\text{deposit}}$  ( $\text{nm}^3$ ), some reported  $R$  ( $\text{nm s}^{-1}$ ), and some reported the deposit height  $h$  (nm). This is measured as a function of  $J$ , beam current  $I$  ( $\text{electrons s}^{-1}$ ), or the accumulated charge  $Q$  (C). The relations are

$$V_{\text{deposit}} = R t_{\text{dwell}} A_{\text{deposit}}, \quad (7)$$

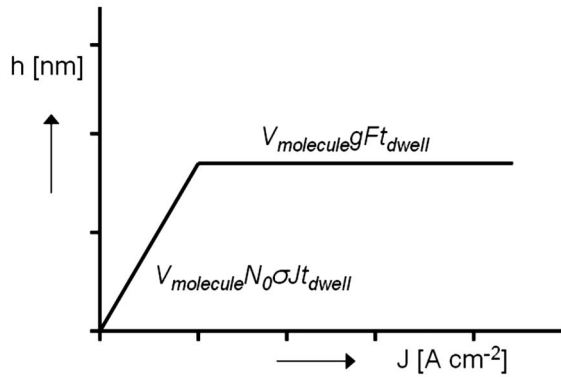
$$h = R t_{\text{dwell}}, \quad (8)$$

$$I = J A_{\text{beam}}, \quad (9)$$

$$Q = I t_{\text{dwell}}, \quad (10)$$

with  $t_{\text{dwell}}$  (s) the dwell time,  $A_{\text{deposit}}$  ( $\text{cm}^2$ ) the area of the deposit, and  $A_{\text{beam}}$  ( $\text{cm}^2$ ) the area of the e-beam.

The various ways results are presented complicate the comparison of results from the different sources. Another complicating matter is that in (nearly) every electron optical system, the beam diameter ( $d_{\text{beam}}$ ) changes when  $I$  is

FIG. 6. Schematic of the deposit height  $h$  as a function of  $J$ .

changed. A change in  $d_{\text{beam}}$  will affect  $R$  (if deposition is done in spot mode) because  $d_{\text{deposit}}$  will change accordingly. If  $V_{\text{deposit}}$  is kept constant and  $d_{\text{deposit}}$  decreases,  $R$  becomes higher. In many cases,  $d_{\text{beam}}$  or  $d_{\text{deposit}}$  are not measured or reported, in which case it is not clear how  $R$  or  $h$  should be interpreted precisely. To avoid this complication for cases where only  $I$  is reported, we restrict ourselves to measurements of  $V_{\text{deposit}}$  as a function of  $I$ . This complication is absent for measurements where  $h$  was reported as a function of  $J$  because both parameters are expressed per area, see Eqs. (7)–(9).

It was mentioned in Sec. II that the growth regimes can be of significant influence. It is interesting to see how the two regimes can be recognized in the various representations we have just discussed. The e.l. and p.l. regimes are indicated in Fig. 6. At low current densities,  $gF/N_0 \gg \sigma J$  and  $h$  is linearly dependent on  $J$  [according to Eq. (5)]. At high current densities,  $gF/N_0 \ll \sigma J$  and  $h$  becomes independent of  $J$  [according to Eq. (6)]. The same behavior is observed when  $V_{\text{deposit}}$  is used instead of  $h$  except for the scaling with  $d_{\text{deposit}}$ .

Alternatively,  $h$  can be plotted as a function of  $Q$ . According to Eq. (9), there are two ways to do this: either vary  $J$  (or  $I$ ) and keep  $t_{\text{dwell}}$  constant or vary  $t_{\text{dwell}}$  and keep  $J$  constant. Both cases are shown in Fig. 7. The first case, where  $J$  is varied [Fig. 7(a)], is the same situation as in Fig. 6. In the second case, where  $t_{\text{dwell}}$  is varied, the e.l. and p.l. regimes are characterized merely by a different slope [Fig. 7(b)].

Yet another representation of the deposit growth behavior is a plot of  $h$  as a function of  $t_{\text{dwell}}$  for a constant  $I$  [see Fig. 7(c)]. These are basically the same data as shown in Fig. 7(b), and both plots can be made for the same experiment. The difference is that in Fig. 7(c) the time scale is made visible. Similarly, the growth regime cannot be easily distinguished in the plot of  $h$  versus  $Q$  since the regimes are again characterized merely by a different slope.

The measurements of the deposited amount of material as a function of the growth conditions allow for a determination of the growth efficiency. This can be defined as the increase in  $h$  per PE (nm/electron). From the definition of the two regimes, it becomes clear that the growth efficiency is highest in the e.l. regime and lowest in the p.l. regime.

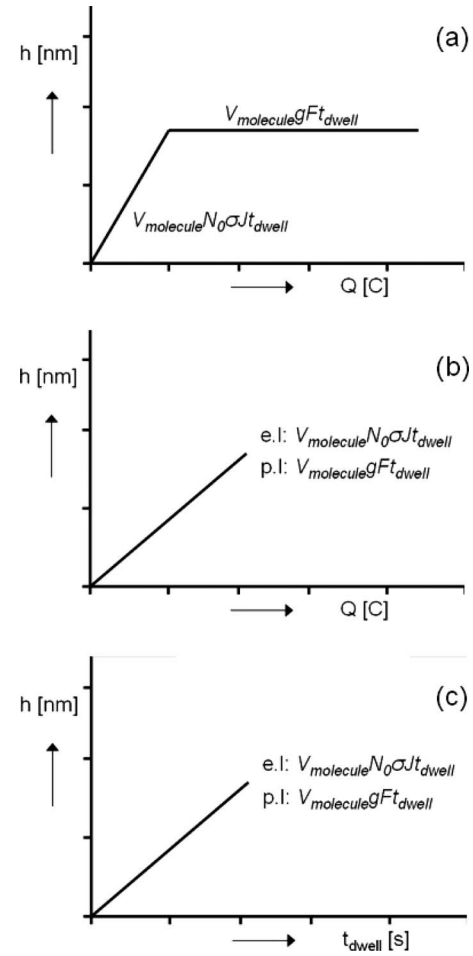


FIG. 7. Schematic of the deposit height  $h$  as a function of  $Q$ . The e.l. and p.l. regimes are indicated. (a) Behavior where  $J$  (or  $I$ ) is varied and  $t_{\text{dwell}}$  is kept constant. (b) Behavior where  $t_{\text{dwell}}$  is varied and  $J$  (or  $I$ ) is kept constant. (c) Same as (b) but now as a function of  $t_{\text{dwell}}$ .

### C. Temperature

The simplifications made in Sec. II are not allowed when the effect of desorption cannot be ignored. This is, for instance, the case when the temperature is varied to study the effect on the growth rate, composition, or conductivity or when the temperature is not constant during the deposition process. In these cases, the temperature will influence the residence time of molecules on the substrate. The relation between  $\tau$  and temperature can be expressed by

$$\tau = \frac{1}{\nu} \exp\left(\frac{E_{\text{des}}}{kT}\right), \quad (11)$$

where  $\nu$  is the vibrational frequency of an adsorbed molecule ( $\text{s}^{-1}$ ),  $E_{\text{des}}$  is the desorption energy (J),  $k$  is the Boltzmann constant ( $\text{m}^2 \text{kg s}^{-2} \text{K}^{-1}$ ), and  $T$  is the temperature (K). Qualitatively speaking, Eq. (11) shows that as the temperature increases,  $\tau$  will decrease. In Eq. (4), a decrease in  $\tau$  will lead to a decrease in  $R$ . Therefore, as the temperature increases, the growth rate will decrease.

How the temperature affects the growth rate quantitatively cannot be established that easily. A situation where the growth is either e.l. or p.l. limited can still be obtained, but the conditions under which this occurs are less straightforward to estimate.

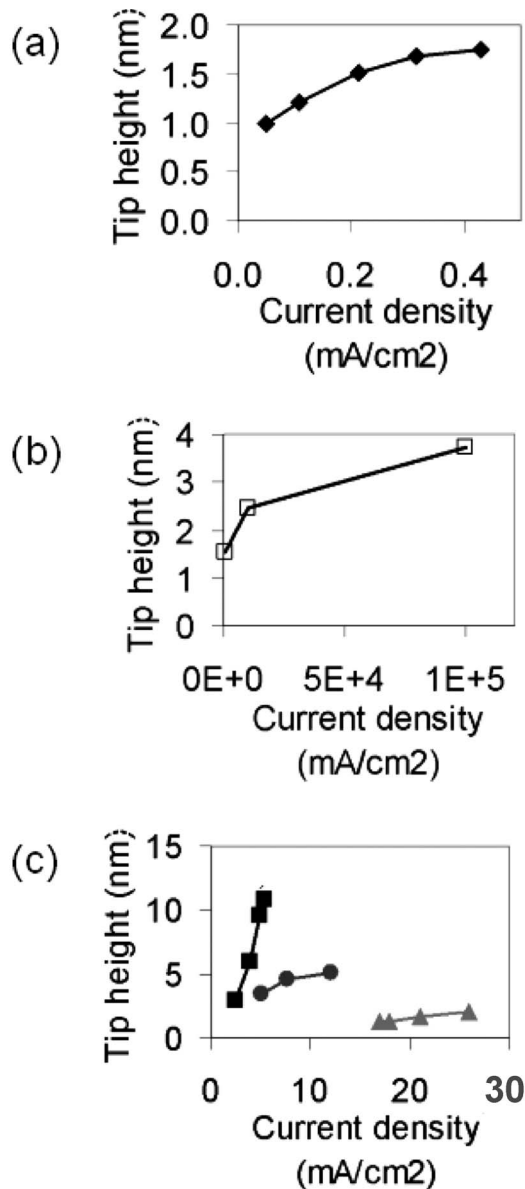


FIG. 8. Tip height as a function of the current density. Data are plotted in three graphs to present the different orders of magnitude and yet still use linear scales: (◆) diffusion pump (Christy, Ref. 2), (□)  $\text{SiH}_2\text{Cl}_2$  (Ichiashi and Matsui, Ref. 61), (■)  $\text{Os}_3(\text{CO})_{12}$  (Scheuer *et al.*, Ref. 60), (●)  $\text{Ru}_3(\text{CO})_{12}$  (Scheuer *et al.*, Ref. 60), and (gray triangle)  $\text{Pt}(\text{PF}_3)_4$  (Wang *et al.*, Ref. 62).

## IV. BEAM PARAMETERS

### A. Current density

#### 1. Height

Now that we have a (simple) growth model and know how to interpret it, we can discuss results from literature. In Figs. 8(a)–8(c)  $h$  as a function of  $J$  is plotted for five different experiments. The data are shown in three different graphs to present the different orders of magnitude and yet still use linear scales. Linear behavior is found for deposition with  $\text{Pt}(\text{PF}_3)_4$  and  $\text{Os}_3(\text{CO})_{12}$ , while for  $\text{Ru}_3(\text{CO})_{12}$ , diffusion pump oil, and  $\text{SiH}_2\text{Cl}_2$  the  $h$  saturates with increasing  $J$ . Based on the model discussed in Sec. III, this means that an e.l. regime was found for  $\text{Pt}(\text{PF}_3)_4$  and  $\text{Os}_3(\text{CO})_{12}$ , and a p.l. regime was found for  $\text{Ru}_3(\text{CO})_{12}$ , diffusion pump oil, and

$\text{SiH}_2\text{Cl}_2$ . The different results can be explained quantitatively to a (relatively) large extent. For instance, based on the results for  $\text{Ru}_3(\text{CO})_{12}$  where growth was p.l., one would expect that growth was p.l. for  $\text{Pt}(\text{PF}_3)_4$  too because  $J$  was largest in the latter case. However, the opposite is true. This can be explained by differences in  $\sigma_{(E)}$  and  $F$ . The amount of electrons needed for the dissociation of one  $\text{Pt}(\text{PF}_3)_4$  molecule is estimated<sup>62</sup> at  $1.8 \times 10^3$ , and for  $\text{Ru}_3(\text{CO})_{12}$  this was about 280.<sup>60</sup> The gas flux in the experiment with  $\text{Pt}(\text{PF}_3)_4$  was larger than in the experiment with  $\text{Ru}_3(\text{CO})_{12}$  ( $1 \times 10^{16}$  versus  $3 \times 10^{14}$  molecules  $\text{cm}^{-2} \text{s}^{-1}$ ). These two differences explain the two growth regimes. For the experiment with diffusion pump oil, the p.l. regime can be explained by the limited  $F$  (about  $5 \times 10^{11}$  molecules  $\text{cm}^{-2} \text{s}^{-1}$ ). In the experiment with  $\text{SiH}_2\text{Cl}_2$  a significantly larger precursor flux was used (in the order of  $10^{16}$  molecules  $\text{cm}^{-2} \text{s}^{-1}$ ),<sup>61</sup> but because  $J$  was a factor of  $10^5$  times larger than for the other experiments, growth was still p.l. The only case for which a quantitative explanation is difficult to give is  $\text{Os}_3(\text{CO})_{12}$ . For  $\text{Os}_3(\text{CO})_{12}$ ,  $h$  was higher [see Fig. 8(c)] and  $F$  was lower than for  $\text{Ru}_3(\text{CO})_{12}$ ,<sup>60</sup> but the growth was still in the e.l. regime. The higher  $h$  indicates that either  $\sigma_{(E)}$  or  $N$  was larger. If  $F$  was lower,  $N$  can only be larger if the sticking coefficient was higher. One would expect that both a higher  $\sigma_{(E)}$  and a higher sticking coefficient would lead to a p.l. regime, but the linear dependency on current density indicates that the growth is e.l.. An explanation was not given by the authors.

Measurements of  $V_{\text{deposit}}$  as a function of  $I$  are shown in Figs. 9(a) and 9(b). For all data points  $t_{\text{dwell}}$  was 120 s. For the experiment with tetra-ethoxy-silane<sup>35</sup> (TEOS) (■) two things can be noticed for the change from 20 to 100 pA: (1)  $V_{\text{deposit}}$  is larger at 100 pA than that at 20 pA and (2)  $V_{\text{deposit}}$  saturates. This indicates that the growth regime changes from being e.l. to being p.l. between 20 and 100 pA. The same behavior, except now in extreme form, is observed for the deposition with dimethyl acetylacetonate gold ( $\text{Me}_2\text{-Au-acac}$ ) (●).<sup>15</sup> The increase in  $V_{\text{deposit}}$  is roughly linear for beam currents of about 2–200 pA, which indicates the e.l. regime. When a significantly larger amount of electrons (beam current of 6 nA instead of 200 pA) is supplied in the same time span,  $V_{\text{deposit}}$  saturates. This indicates the p.l. regime.

An entirely different behavior is observed for the experiment with contamination (▲).<sup>9</sup> For low beam currents (between 3 and 30 pA)  $V_{\text{deposit}}$  increases roughly linearly with increasing  $I$ . However, when  $I$  is increased above 30 pA (up to 200 pA),  $V_{\text{deposit}}$  decreases. A similar behavior was found for contamination growth for beam currents  $>25$  pA by Miura *et al.*<sup>38</sup> (not shown because the dwell times used were not reported). A decrease in  $V_{\text{deposit}}$  does not mean that material was removed from a deposit but that less material was deposited in the same dwell time.  $F$  was constant during the entire experiment, so the number of molecules arriving at the irradiated area was also constant. The decrease in  $V_{\text{deposit}}$  could be the result of a decrease in  $V_{\text{molecule}}$  at higher beam currents. Extrapolating  $R$  from low  $I$  (i.e., from the e.l. regime) to 200 pA, this would be a decrease in  $V_{\text{molecule}}$  in the order of  $10^3$ . Such a strong decrease is not very likely. There-

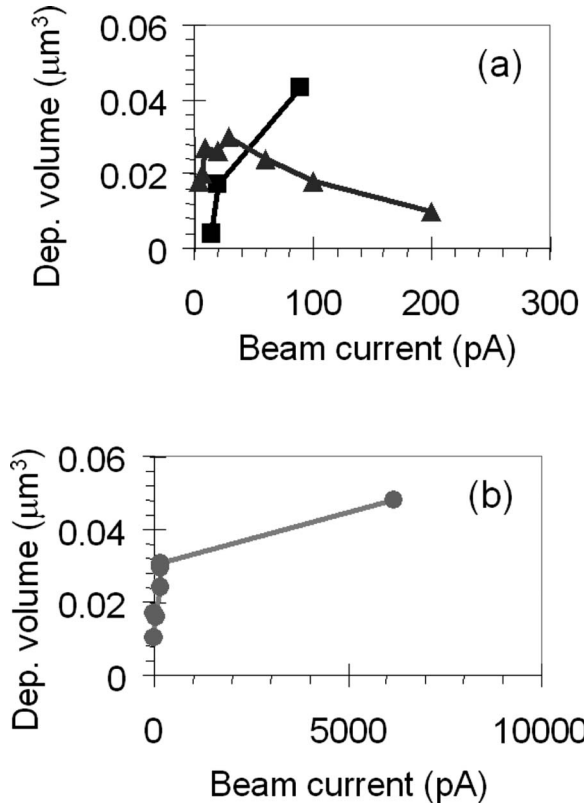


FIG. 9. Deposited volume as a function of beam current. The dwell time was 120 s in all cases: ( $\blacktriangle$ ) contamination (Schiffmann, Ref. 9), ( $\blacksquare$ ) TEOS (Perentes *et al.*, Ref. 35), and (gray circle)  $\text{Me}_2\text{-Au-acac}$  (Mølhave *et al.*, Ref. 15).

fore, this decrease cannot be explained anymore with the simplified model we used to describe the e.l. and p.l. regimes and we must turn to the more complicated model that includes the residence time  $\tau$ . As mentioned in Sec. III C, a decrease in  $\tau$  will lead to a decrease in  $R$  and therefore in  $V_{\text{deposit}}$

If all other conditions are kept constant during the experiment, a decrease in  $\tau$  can only be the result of an increase in temperature. This can be caused by e-beam induced heating. Beam induced heating is the result of energy transfer from the PEs to phonons in the substrate. The theoretical power  $P$  that is supplied by the e-beam to an irradiated target is

$$P = V_{\text{PE}} I, \quad (12)$$

with  $V_{\text{PE}}$  the acceleration voltage and  $I$  the beam current. In practice, the effect of this power input on the target temperature will depend on the amount of energy that is actually transferred (for instance, BSEs or SEs emitted from the target do not transfer their energy) and on the heat dissipation from the irradiated area to bulk. If the heat dissipation is larger than the power input, the temperature will not be affected. However, if the heat dissipation is less, the temperature will rise. There is some disagreement on the question whether beam induced heating plays a significant role in FE-BIP. Based on calculations, Li and Joy<sup>63</sup> assumed that beam induced heating has a negligible effect. Folch and Servat<sup>64</sup> came to the same conclusion based on experimental data. However, Bret *et al.*,<sup>65</sup> Randolph *et al.*,<sup>40</sup> and Utke *et al.*<sup>66</sup>

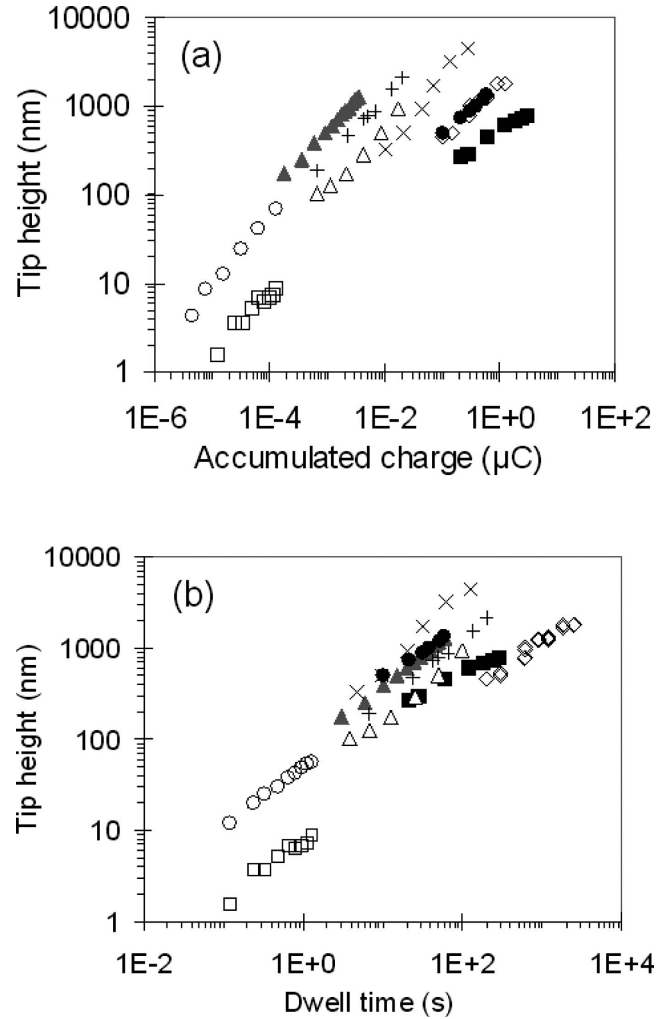


FIG. 10. (a) Deposit height as a function of accumulated charge. (b) Same data but now as a function of dwell time: (gray triangle)  $\text{Me}_2\text{-Au-acac}$  (Koops *et al.*, Ref. 67), ( $\bullet$ )  $\text{Me}_2\text{-Au-tfac}$  (Koops *et al.*, Ref. 25), ( $\blacksquare$ )  $\text{W}(\text{CO})_6$  (Koops *et al.*, Ref. 25), ( $+$ )  $\text{W}(\text{CO})_6$  (Kohlmann-von Platen *et al.*, Ref. 68), ( $\diamond$ )  $\text{W}(\text{CO})_6$  (Liu *et al.*, Ref. 69), ( $\triangle$ )  $\text{CpPtMe}_3$  (Hübner *et al.*, Ref. 70), ( $\times$ )  $\text{Co}_2\text{CO}_8$  (Lau *et al.*, Ref. 8), ( $\circ$ )  $\text{WF}_6$  (Hiroshima and Komuro, Ref. 71), and ( $\square$ ) contamination (Hiroshima and Komuro, Ref. 71).

assumed that the increase in temperature can be as much as 60–80 °C for tip depositions. The sharp decrease in growth efficiency for contamination in Fig. 9(a) ( $\blacktriangle$ ) is certainly consistent with the behavior that is expected when there is significant beam induced heating.

Until now, we have discussed measurements of  $h$  as a function of  $J$  (Fig. 8) and  $V_{\text{deposit}}$  as a function of  $I$  (Fig. 9). The growth of deposits is often characterized by measuring  $h$  as a function of  $Q$  or  $t_{\text{dwell}}$ . In practice, this is the same measurement. As mentioned in Sec. III B, the two plots give a different picture. Results from literature for the growth of tips are shown in Fig. 10 on a log-log scale [ $h$  versus  $Q$  in Fig. 10(a),  $h$  versus  $t_{\text{dwell}}$  in Fig. 10(b)]. There is not sufficient information available to explain the trends in Fig. 10 completely. It is also difficult to compare results obtained with different precursors, such as for  $\text{CpPtMe}_3$  ( $\triangle$ ) and  $\text{WF}_6$  ( $\circ$ ).<sup>71</sup> With information that is available, we will try to explain two trends. First of all, Fig. 10(a) shows that tips fabricated from  $\text{Me}_2\text{-Au-acac}$ <sup>67</sup> (gray triangle) and dimethyltrifluoro-acetylacetonate gold<sup>25</sup> ( $\text{Me}_2\text{-Au-tfac}$ ) ( $\bullet$ ) were

grown to the same height, but the  $Q$  required to obtain that height differs by two orders of magnitude. On the other hand, Fig. 10(b) shows that the same height was obtained in practically the same time span. Considering the chemical similarity of the precursors, it is expected that  $\sigma_{(E)}$  and  $V_{\text{molecule}}$  are similar. The gas flux was reported in different units ( $\text{Pa l s}^{-1}$  versus  $\text{Pa}$ ), so  $F$  cannot be compared. However,  $I$  is known for both experiments. In the experiment with  $\text{Me}_2\text{-Au-acac}$  a beam current of 60 pA was used, versus a beam current of 10 nA for the experiment with  $\text{Me}_2\text{-Au-tfac}$ . Since the same  $h$  was obtained in the same  $t_{\text{dwell}}$  this must mean that  $I$  was not the determining factor for the tip grown from  $\text{Me}_2\text{-Au-tfac}$ . In other words, the experiment with  $\text{Me}_2\text{-Au-tfac}$  was p.l. and a large part of the electrons was simply wasted, speaking from the point of view of growth efficiency.

Something similar can be said for the deposition with  $\text{W}(\text{CO})_6$ . PE energies used for the deposition were 20 keV (+),<sup>68,25</sup> 25 keV (■),<sup>25</sup> and 200 keV (◇).<sup>69</sup> The gas flux again cannot be compared (no numbers are given or different units are used). The only information available is the beam current. Kohlmann-von Platen *et al.*<sup>68</sup> used the lowest  $I$ , 100 pA, and had the highest growth efficiency (nm/C). The beam current in the experiment by Koops *et al.*<sup>25</sup> was 10 nA. Compared to Kohlmann-von Platen *et al.*,<sup>68</sup> this resulted in a growth efficiency of about 500 times smaller [Fig. 10(a)], while the  $t_{\text{dwell}}$  to reach the same  $h$  was only about five times longer [Fig. 10(b)]. The difference of a factor of 100 is a strong indication that the experiment by Koops *et al.*<sup>25</sup> was p.l. Liu *et al.*<sup>69</sup> used a beam current of 0.5 nA. Compared to the experiment by Kohlmann-von Platen *et al.*,<sup>68</sup> the growth efficiency is a factor of 50 times smaller and it took about 10 times longer to reach the same  $h$ . This leaves a factor of 5 to be explained. Possibly, the difference is due to the higher PE energy, growth was p.l., or  $V_{\text{molecule}}$  decreased during the deposition.

Enough information is available from the articles to compare results from Figs. 9 and 10(a). This is done in Fig. 11. A comparison with Fig. 10(b) is not possible because the data in Fig. 9 were obtained by keeping  $t_{\text{dwell}}$  constant. When trying to compare the data in Fig. 11, we have to keep in mind that the time dependence is different for both types of data. The measurements from Fig. 9 (shown in black in Fig. 11) were obtained by varying the  $I$  for a constant  $t_{\text{dwell}}$  while the measurements from Fig. 10 (shown in gray in Fig. 11) were obtained by varying  $t_{\text{dwell}}$  for a constant  $I$ . Therefore, when a black curve has a negative slope [such as for contamination (▲) or for  $\text{Me}_2\text{-Au-acac}$  (●)], it does not mean that material was removed, but it means that  $h$  decreased when  $I$  was increased for a constant  $t_{\text{dwell}}$ . From the negative slopes, it is observed that the growth regimes in the experiments where  $I$  was varied (black curves) were all p.l. at the highest beam currents.

## 2. Width

Concerning the lateral growth, it is consistently reported that increasing  $I$  leads to an increase in  $d_{\text{deposit}}$ <sup>15,38,68,72</sup> with  $d_{\text{deposit}}$  increasing proportionally to  $\sqrt{I}$ .<sup>15,68</sup> However, as men-

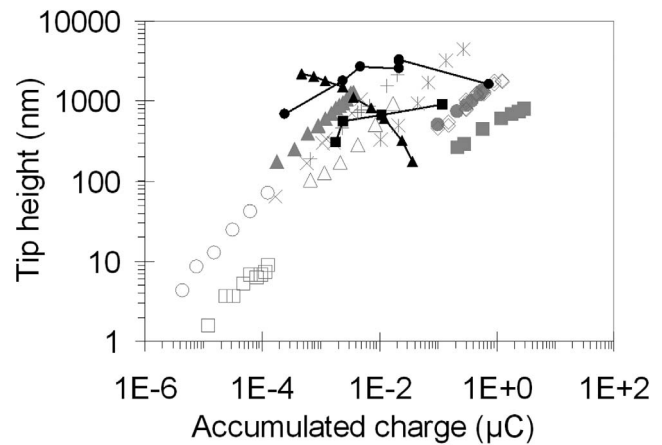


FIG. 11. Data from Figs. 9(a) and 9(b) superimposed on Fig. 10(a) to compare the effect of beam current and dwell time: (gray triangle)  $\text{Me}_2\text{-Au-acac}$  (Koops *et al.*, Ref. 67), (gray circle)  $\text{Me}_2\text{-Au-tfac}$  (Koops *et al.*, Ref. 25), (gray square)  $\text{W}(\text{CO})_6$  (Koops *et al.*, Ref. 25), (+)  $\text{W}(\text{CO})_6$ , 20 kV (Kohlmann-von Platen *et al.*, Ref. 68), ( $\Delta$ )  $\text{CpPtMe}_3$  (Hübner *et al.*, Ref. 70), (x)  $\text{Co}_2\text{CO}_8$  (Lau *et al.*, Ref. 8), ( $\circ$ )  $\text{WF}_6$  (Hiroshima and Komuro, Ref. 71), ( $\square$ ) contamination (Hiroshima and Komuro, Ref. 71), ( $\blacktriangle$ ) contamination (Schiffmann, Ref. 9), ( $\blacksquare$ ) TEOS (Perentes *et al.*, Ref. 35), and ( $\bullet$ )  $\text{Me}_2\text{-Au-acac}$  (Mølhave *et al.*, Ref. 15).

tioned in Sec. III B,  $d_{\text{beam}}$  also increases with  $I$  proportionally to  $\sqrt{I}$  (to a first approximation). This implies that  $d_{\text{deposit}}$  depends on  $d_{\text{beam}}$  rather than on  $I$ . This is confirmed by Beaulieu *et al.*,<sup>72</sup> who reported that the lateral growth rate is independent of  $I$ .

Not only is  $d_{\text{deposit}}$  dependent on  $d_{\text{beam}}$ ; there is also a distinct dependence on  $Q$ . To keep matters simple, we consider the growth of tips (by keeping the beam in a stationary position on the sample). It is consistently measured that (1) the  $d_{\text{deposit}}$  increases with increasing  $d_{\text{beam}}$  and (2) the development of  $d_{\text{deposit}}$  as a function of  $t_{\text{dwell}}$  consists of a fast increase, followed by saturation.<sup>6,9,68,72-74</sup> Experimental results are shown in Fig. 12(a); the inset shows a blow-up of the very early growth stage. A similar trend was found by Liu *et al.*<sup>69</sup> (not shown). The deposit diameter is always larger than the PE beam diameter.

A model for this lateral broadening of tips was suggested by Silvis-Cividjian *et al.*<sup>56</sup> At the start of the deposition process, the e-beam is focused on a fixed spot on a flat surface. SEs are being emitted from the substrate around the irradiated point and dissociate adsorbed precursor molecules. As the deposit starts to grow, SEs continue to be emitted from the substrate, but emission from the deposit itself will also occur. The electrons exit from all sides of the deposit and cause deposition on all sides of it. Since the SEs have a certain escape length, deposition can occur outside the trajectories of the PEs. This is the initial growth stage where  $d_{\text{deposit}}$  increases rapidly. Once  $d_{\text{deposit}}$  is about equal to the  $d_{\text{beam}}$  plus twice the SE escape length, the lateral growth stops. Figure 12(b) shows a typical result from a Monte Carlo simulation. The lines indicate the time evolution of the cross-sectional tip profiles.

In Sec. II C, we have seen that it is not clear what the relative contribution of the PEs, BSEs, and SEs is to the growth. The results of the model by Silvis-Cividjian *et al.*,<sup>56</sup> which takes into account only dissociation by SEs, are quali-

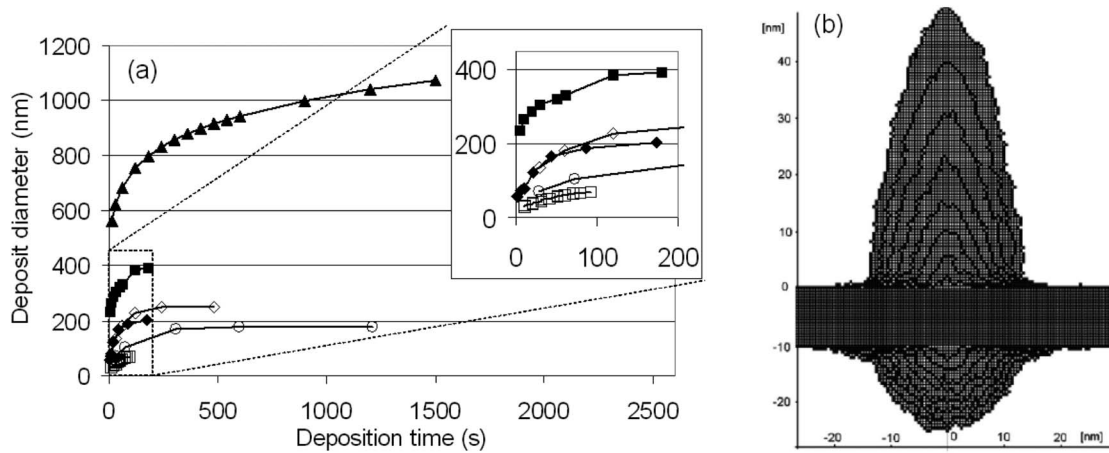


FIG. 12. The development of the width of an e-beam deposited structure. (a) Experimental results. Inset shows the width development for short times. (b) Result from a Monte Carlo simulation. The lines indicate the time evolution of the cross-sectional profiles. From Ref. 56, Copyright © (2002) by Elsevier. Reprinted with permission from Elsevier: (▲) MeCpPtMe<sub>3</sub> (Beaulieu *et al.*, Ref. 72), (○) TEOS (Perentes *et al.*, Ref. 35), (□) W(CO)<sub>6</sub> (Kohlmann-von Platen *et al.*, Ref. 68), (□) Fe(CO)<sub>5</sub> (Shimojo *et al.*, Ref. 74), (◆) CpPtMe<sub>3</sub> (Hübner *et al.*, Ref. 70), and (◇) contamination (Schiffmann, Ref. 9).

tatively consistent with the experimentally observed lateral growth behavior. In the Monte Carlo simulation by Fowlkes *et al.*,<sup>57</sup> a dissociation cross section was used that also takes into account the contribution of PEs and BSEs. Analysis of tip growth behavior showed that the vertical growth is due mostly to direct dissociation by PEs and the lateral growth is due mostly to SEs. As the tip grows longer, its sidewall surface area becomes larger and the amount of SEs that cross the substrate-vacuum interface (and contribute to the lateral growth) increases. Therefore, although the real cross section for dissociation is unknown, it seems reasonable to assume that the lateral broadening is due mostly to dissociation by SEs.

Deposits with a small width can be fabricated by using a small beam and stopping the deposition process before lateral widening occurs. In that case, a dot is deposited instead of a high aspect ratio tip. Stopping the growth process in its initial stage influences also the height of the deposits, so in this regime it is not possible to control the aspect ratio independently of the width of the deposit merely with the accumulated charge. Sub-10-nm structures have been fabricated with widths of 8,<sup>75,76</sup> 5,<sup>77</sup> 4,<sup>78</sup> 3.5,<sup>79</sup> 1.5,<sup>80</sup> and even 1.0 nm.<sup>81</sup> While for large deposits the deposited mass is identical every

time the experiment is repeated, a significant variation in mass is found for the very smallest deposits. Van Dorp *et al.*<sup>82</sup> deposited arrays of sub-5-nm dots on an *a*-C substrate with a constant dwell time per array. A typical array is shown in Fig. 13(a) (an annular dark field image obtained in a STEM). It is observed that the intensity of the dots (which is proportional to the deposited mass) is not constant over the array; some of the dots are very bright while other dots are barely visible. When the average deposit mass is determined for each array, a linear dependency on the dwell time is found [Fig. 13(b)]. In Fig. 13(c), the distribution of deposited masses is shown for these arrays. The scaling of the arbitrary units for the deposited mass is identical for Figs. 13(b) and 13(c). Negative values are the result of background subtractions used to determine the deposited mass from the STEM images. As the dwell time decreases, the width of the distribution of masses increases (relative to the average deposited mass) and the distributions become skewed. This behavior is consistent with the Poisson statistics. The Poisson theory describes the probability that an event occurs during a particular interval given an expected number of discrete occurrences. In other words, these experiments suggest that the

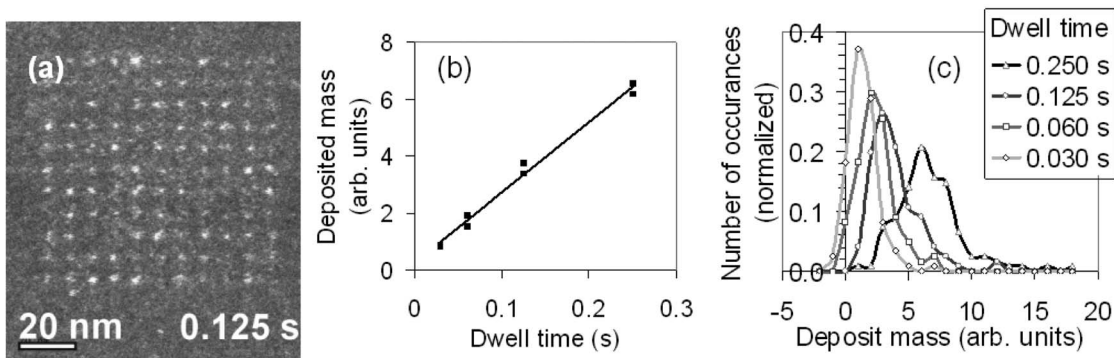


FIG. 13. (a) Annular dark field (ADF) image of an array of sub-5-nm dots. Although the dwell time was constant (0.125 s) for all the dots in the array, it is observed that the dot intensity (equal proportionally to the deposited mass) is not constant. (b) The average mass per array as a function of dwell time. (c) The distribution of masses for the different dwell times. The scaling of the arbitrary units for the deposited mass is identical for (b) and (c).

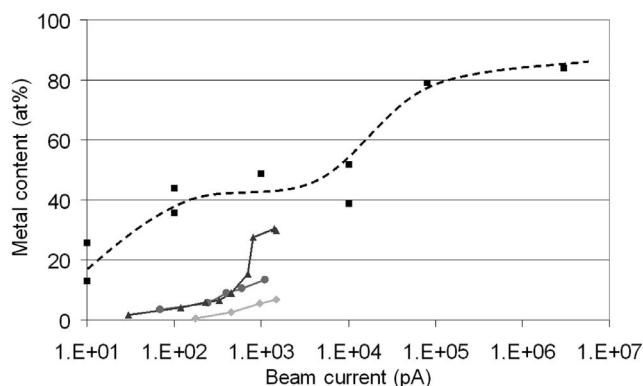


FIG. 14. The metal content as a function of the beam current. Lines are drawn to guide the eye: (■)  $\text{Co}_2(\text{CO})_8$  (Utke *et al.*, Ref. 7), (▴)  $\text{Me}_2\text{-Au-tcac}$  (Weber *et al.*, Ref. 29), (○)  $\text{CpPtMe}_3$  (Weber *et al.*, Ref. 85), and (◇)  $\text{Mo}(\text{CO})_6$  (Weber *et al.*, Ref. 85).

deposition process consists of discrete dissociation events and this becomes visible during the nucleation stage of a deposit.

The difficulty with these high-resolution experiments is that the precise experimental conditions are not well known, especially since deposition is done under non-UHV conditions ( $10^{-3}$  mbar). For the micrometer-sized tips we discussed earlier, this is less relevant since for nearly the entire growth process the deposit surface is the determining factor, not the substrate surface. For the high-resolution experiments, the growth is terminated in the nucleation stage and the substrate surface and its chemical condition play a major role.

### 3. Composition and morphology

For nearly all experiments with metal-containing precursors, the metal content increases with increasing beam current. Results for  $\text{Mo}(\text{CO})_6$ ,  $\text{CpPtMe}_3$ , and  $\text{Me}_2\text{-Au-tfac}$  (Refs. 29 and 83–85) and  $\text{Co}_2\text{CO}_8$  (Ref. 7) are shown in Fig. 14. The metal content for deposits of  $\text{Me}_2\text{-Au-acac}$  and dimethyl-hexafluoro-acetylacetonate gold ( $\text{Me}_2\text{-Au-hfac}$ ) show a similar dependency on beam current as  $\text{Me}_2\text{-Au-tfac}$ . An increase in the Co content with beam current was also reported in Ref. 8.

The increase in the metal content with beam current that is observed in Fig. 14 can be due to two parallel processes. First, with an increase in beam current, the time frame in which the deposit is exposed to a specific amount of accumulated charge decreases. As we have seen earlier, this can lead to a shift from e.l. to p.l. regime. Related to this, the increase in beam current can induce an increase in the desorption of fragments of (initially only partially dissociated) precursor molecules. This can lead to higher concentrations of nonvolatile (among others metal) components in the final deposit. Another mechanism is e-beam induced heating. As we have seen in Sec. IV A 1, there are indications that beam induced heating can lead to a significant rise in temperature for tip depositions. A raise in temperature may, for instance, facilitate the desorption of volatile species, as well as change the dissociation mechanism. We will discuss this in more detail below, where we present the dependence of the deposit morphology on the beam current.

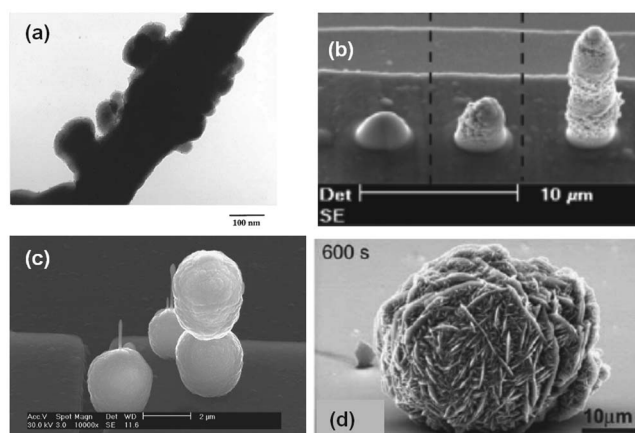


FIG. 15. Surface morphologies for high current deposits created with the beam in spot mode. (a) Deposits from  $\text{Mo}(\text{CO})_6$ . From Ref. 85. (b) Deposits from  $\text{hfac-Cu-VMTS}$ . From Ref. 86. (c) Deposits from  $[\text{Co}(\text{CO}_3)\text{NO}]$ . Reprinted with permission from Ref. 8. (d) Deposits from  $\text{Co}_2\text{CO}_8$ . Reprinted from Ref. 7. Copyright © 2003 by Elsevier. Reprinted with permission by Elsevier.

The morphology of tips can clearly be affected by the beam current. It is reported for tips deposited from  $\text{Me}_2\text{-Au-acac}$ ,  $\text{Me}_2\text{-Au-tfac}$ ,  $\text{Me}_2\text{-Au-hfac}$ , bis-hexafluoro-acetylacetonate copper [ $\text{Cu}(\text{hfac})_2$ ],  $\text{Mo}(\text{CO})_6$ , and  $\text{CpPtMe}_3$  that at low beam currents, the tips have a smooth shank and are completely amorphous. In contrast, tips deposited with high beam currents have an irregular shape and are polycrystalline, the crystallites being between 2 and 8 nm in size.<sup>85</sup> The transition between the two regimes was, for instance, around 60 pA for  $\text{Me}_2\text{-Au-tfac}$ . An example of the roughening of the Mo tip surface is shown in Fig. 15(a). Similar surface roughening was also observed for  $\text{hfac-Cu-VMTS}$  (Ref. 86) [Fig. 15(b)] and in a more extreme form for  $\text{Co}(\text{CO}_3)\text{NO}$  [Fig. 15(c)] and  $\text{Co}_2\text{CO}_8$  [Fig. 15(d)]. Note that all deposits in Fig. 15 were created with the beam in spot mode.

In an elaborate study, the development of the morphology during the growth of tips deposited from  $\text{Co}_2(\text{CO})_8$  was determined and was found to be quite complex.<sup>87</sup> At low beam currents (20 and 112 pA), the surface of the tips is smooth and the material consists of nanocomposite material (1–2 nm Co crystals embedded in an *a*-C- and O-rich matrix). The surface of the longer tips (dwell times of 300–600 s) is still smooth, but on the inside a crust and a core form at the bottom of the tips. This substructure of crust and core becomes more apparent for deposits from higher beam currents (1.1 and 10 nA), where it extends along the entire length of the tip (see Fig. 16). The crust, consisting of Co crystals, surrounds the nanocomposite core. When the beam current is increased further to 82 nA, the core/crust structure is absent and only Co-rich crystalline material is found. When the beam current is finally increased to 3  $\mu\text{A}$ , the surface becomes rough and the deposit consists of crystals with micrometer length growing in a whiskerlike shape toward the precursor source [see Fig. 15(d)].

The authors explained these results to a significant extent by e-beam induced heating. Taking into account the limited thermal conductivity of the deposit material, the heat dissipation from the tip to the substrate will be a determining

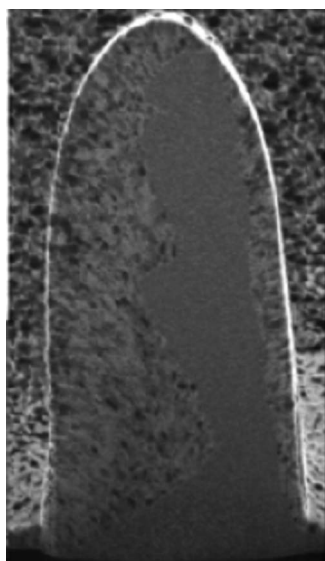


FIG. 16. Core-crust structure in a tip grown from  $\text{Co}_2(\text{CO})_8$ . From Ref. 87. Copyright © 2005 by Wiley-VCH Verlag GmbH & Co. KGaA. Reprinted with permission by Wiley-VCH Verlag GmbH & Co. KGaA.

factor for the temperature of the tip. At low beam currents and when the tip is still short, the heat dissipation will be sufficient to keep the tip at room temperature. However, when the tip length or the beam current increases, the temperature of the tip will be raised above room temperature. At 82 nA, the estimated temperature rise is nearly 1 degree, which increases to more than 30 degrees at 3  $\mu\text{A}$  for the described experimental conditions. The desorption of volatile species can be facilitated by the higher temperature, leading to a higher metal content. Apart from this, the dissociation mechanism can change at higher temperatures.  $\text{Co}_2(\text{CO})_8$  normally has an endothermic decomposition reaction occurring around 100 °C, which is above the estimated temperature reached in tips at the highest beam current. However, this thermal decomposition temperature can be significantly lowered if the activation energy for decomposition is lowered by autocatalytic effects. In this example, deposited Co would act as catalyst for the decomposition of  $\text{Co}_2(\text{CO})_8$ . A similar behavior has been observed for  $\text{Fe}(\text{CO})_5$  and  $\text{Cr}(\text{CO})_6$ .<sup>88</sup> These autocatalytic effects can bring the thermal decomposition temperature to within the temperature range reached during the described experiments. A similar combination of temperature rise and autocatalytic effect is expected to be the cause for the development of the deposit from  $\text{Co}(\text{CO})_3\text{NO}$ .

The roughening that was observed at the highest beam currents for  $\text{Me}_2\text{-Au-acac}$ ,  $\text{Me}_2\text{-Au-tfac}$ ,  $\text{Me}_2\text{-Au-hfac}$ ,  $\text{Cu}(\text{hfac})_2$ ,  $\text{Mo}(\text{CO})_6$ ,  $\text{CpPtMe}_3$ , and  $\text{hfac-Cu-VMTS}$  may be due to crystallization. As a result of the increase in temperature, volatile fragments desorb more easily and the (increased amount of) metal rearranges into small crystals. The fact that the roughening was observed for quite different precursors indicates again that e-beam induced heating can play a significant role during deposition.

There are also examples where the effect of the beam current is not fundamentally different from the effect of the accumulated charge. For instance, the deposition of Ni-

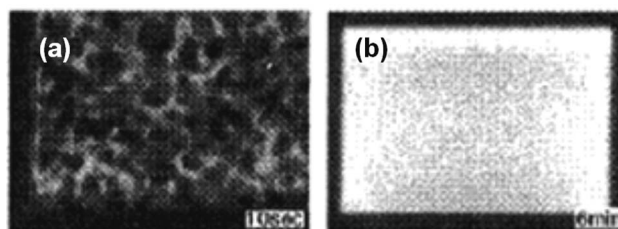


FIG. 17. The effect of accumulated charge on the morphology of squares deposited from  $\text{Ni}(\text{C}_5\text{H}_5)_2$  at  $-85^\circ\text{C}$ . (a) At a low accumulated charge, a porous, open structure is formed. (b) At higher accumulated charges, a closed, solid film is formed. From Ref. 76. Copyright © 2001 by World Scientific Publishing Co. Reprinted with permission by World Scientific Publishing Co.

containing squares on a carbon substrate (kept at  $-85^\circ\text{C}$ ) from  $\text{Ni}(\text{C}_5\text{H}_5)_2$ .<sup>76</sup> At a low accumulated charge, the squares were open, porous structures and the deposited material formed a network with (relatively) large openings [Fig. 17(a)]. Upon continued irradiation, the porous structures closed to form (nearly) solid films [Fig. 17(b)]. Structures created with different beam currents but with a similar accumulated charge were in a similar state of transition from an open structure to a closed film. The fact that accumulated charge and beam current were interchangeable indicates that the accumulated charge is the only parameter relevant for the deposition behavior under these specific conditions. An explanation for the formation of the open structures was not given.

#### 4. Density

Another property that can be measured as a function of the beam current is the deposit density. The density of tips deposited from tetramethyl ortho-silicate (TMOS),  $\text{hfac-Cu-VMTS}$ , and  $\text{Co}_2\text{CO}_8$  has been measured for beam currents of 0.1, 1, and 100 nA.<sup>66</sup> It was found that the density of the deposit from TMOS is independent of the beam current used. For deposits from  $\text{hfac-Cu-VMTS}$  both the density and the metal content increased with increasing beam current. Tips created with a current of 1 nA had a rough surface. For  $\text{Co}_2\text{CO}_8$ , a similar behavior was observed. See Table I for a summary of the results. The bulk density is 8.96  $\text{g cm}^{-3}$  for Cu and 8.90  $\text{g cm}^{-3}$  for Co.

The independence of the density and composition of deposits from TEOS led the authors to the conclusion that the decomposition is fully due to dissociation by electrons and that thermal effects are absent. The TEOS precursor molecule dissociates thermally at about 580 °C, which is much higher than the calculated temperature rise for a beam cur-

TABLE I. The effect of increasing beam current on the density and metal content of deposits from  $\text{hfac-Cu-VMTS}$  and  $\text{Co}_2(\text{CO})_8$ . From Ref. 66. Higher beam currents lead to a higher density and metal content for both precursors. Bulk density are 8.96  $\text{g/cm}^3$  (Cu) and 8.90  $\text{g/cm}^3$  (Co).

Beam current (nA)	Metal content (at. %)		Total deposit density ( $\text{g/cm}^3$ )	
	Cu	Co	Cu	Co
0.1	14	31	2.05	4.2
1	30	...	4.3	...
100	...	73	...	7.2

TABLE II. Results from measurements of the resistivity of deposited wires as a function of the beam current.

Material	Author(s)	Ref.	Highest resistivity (beam current)	Lowest resistivity (beam current)
CpPtMe <sub>3</sub>	Weber <i>et al.</i>	29	5.5 Ω cm (200 pA)	1 Ω cm (660 pA)
Me <sub>2</sub> -Au-acac, Me <sub>2</sub> -Au-tfac, and Me <sub>2</sub> -Au-hfac	Koops and co-workers	83–85,89	400 Ω cm (100 pA)	2 × 10 <sup>-2</sup> Ω cm (900 pA)
Mo(CO) <sub>6</sub>				2 × 10 <sup>-3</sup> Ω cm (···)
Co <sub>2</sub> (CO) <sub>8</sub>	Lau <i>et al.</i>	8	5 Ω cm (183 pA)	1.6 × 10 <sup>-4</sup> Ω cm (10.7 nA)
W(CO) <sub>6</sub>	Kohlmann-von Platen <i>et al.</i>	90		2 × 10 <sup>-2</sup> Ω cm (1000 pA)
Fe <sub>3</sub> (CO) <sub>12</sub>	Brük <i>et al.</i>	91	10 <sup>3</sup> Ω cm (11 pA)	4 × 10 <sup>-2</sup> Ω cm (232 nA)

rent of 1 nA (about 87 °C). The rough surface in the case of the Cu deposits and the large increase in metal content for the Co deposits indicate thermally assisted deposition (see also Sec. IV A 3).

### 5. Conductivity

Consistent with the increase in metal content, the resistivity of wires deposited with the e-beam decreases with increasing beam current. The relevant data are summarized in Table II and a typical example of the dependency is shown in Fig. 18(a).

Koops and co-workers<sup>29,83–85,89</sup> only gave specific details for experiments with Me<sub>2</sub>-Au-tfac but mentioned a similar behavior for the other two gold precursors. A wide spread in resistivities for constant beam currents was found for Co<sub>2</sub>(CO)<sub>8</sub> deposits and this was attributed to the scan method used to fabricate the Co-containing wires. More details on this aspect can be found in Sec. V E 2.

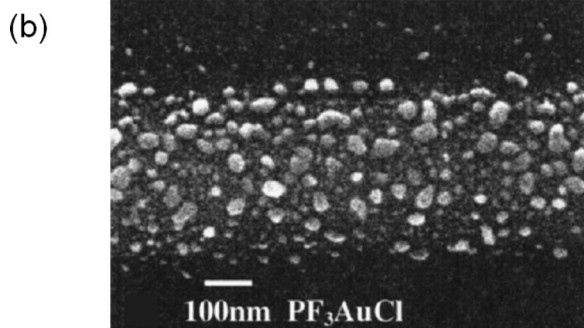
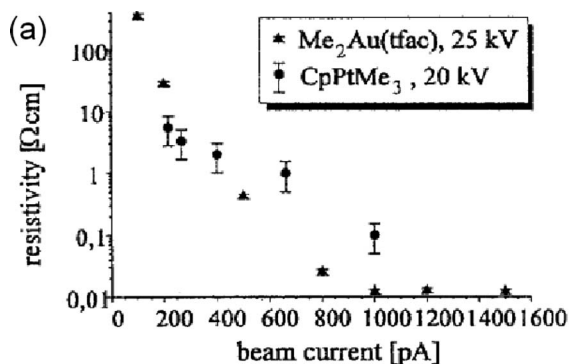


FIG. 18. (a) A typical example of the dependence of the resistivity of deposited wires on the beam current. From Ref. 89. Copyright © 1996 by Elsevier. Reprinted with permission by Elsevier. (b) Grains of gold deposited from Au(PF<sub>3</sub>)<sub>3</sub>. The grains were found for all beam currents, so changes in resistivity as a function of beam current are the result of grain percolation. From Ref. 92.

For nearly all precursors the resistivity behavior as a function of the beam current is related to the metal content. As shown in Fig. 14, the metal content consistently increases with increasing beam current. This is also consistent with the *I*-*V* characteristics, which were determined after deposition at different temperatures for the platinum and the gold wires. The gold wires deposited with the high beam current show Ohmic behavior. At lower beam currents, the gold wires contain less metal and show nonlinear characteristics, probably Poole–Frenkel conduction or activated tunneling. The platinum wires have a lower metal content than the gold wires (see Fig. 14) and show only the nonlinear behavior. An exception to this rule is the experiment with AuCl(PF<sub>3</sub>)<sub>3</sub>.<sup>92</sup> This precursor yielded pure gold crystals, even at the lowest beam current. The resistivity of wires decreased with increasing beam current, which is the result of better grain percolation (see Fig. 18). So this is effectively not so much the result of the beam current but rather the result of more accumulated charge.

When the conductivity of deposits is measured as a function of accumulated charge, the general trend is that the resistance decreases with increasing accumulated charge. This is, for instance, the case in measurements by Brük *et al.*<sup>91</sup> They found that the resistance of wires deposited from Fe<sub>3</sub>(CO)<sub>12</sub> decreases with increasing accumulated charge. However, since the dimensions of the deposits were not reported, it is not possible to elucidate the mechanism by which the resistance decreased. This can be the result of merely a larger wire cross section (a thicker wire can carry more current) or also of a change in resistivity. The latter case would imply an accumulated charge-dependent change in material properties.

A more complete experiment was performed with W(CO)<sub>6</sub>.<sup>73</sup> The electrical properties of the deposited wires were measured *in situ* for electron doses varying from 0.1 × 10<sup>5</sup> to 5 × 10<sup>5</sup> C m<sup>-2</sup>. A fixed potential was applied over the wire at regular intervals during the deposition. This gives the development of the current passed through the wire as a function of the total accumulated charge. For the various beam energies used, a constant trend was observed. Initially, the current increment per charge increment increased rapidly, after which the current increment stabilized to a constant value. In other words, the conductivity increases nonlinearly in the initial stage and shows a linear increase later on. The authors explained the initial nonlinear stage by a change in the structure of the wire. The wire starts as a discontinuous line of nuclei and evolves into a continuous wire. In the later

stage, when the wire has become continuous, the increase in conductivity is merely the result of an increase in wire cross section. This implies that the deposition mechanism remains unchanged during the growth and that it is independent of the accumulated charge.

An anomalously high decrease in resistivity is reported for squares deposited from  $WF_6$ .<sup>93</sup> The accumulated charge was varied by varying the pitch between the pixels. With a variation in accumulated charge of a factor of 16, the amount of deposited material increased by a factor of about 10 and the resistivity decreased from  $1.3 \times 10^3$  to  $8.4 \times 10^{-2} \Omega \text{ cm}$  (a factor of  $10^5$ ). An explanation for this behavior is not given.

## B. Electron energy

As was discussed in Sec. II C, experiments have shown that electrons with energies of about 5 to a few hundred eV contribute significantly to the growth of deposits. The relative contribution of high-energy electrons to the growth is less clear. It is tempting to think that  $\sigma(E)$  can be determined for a specific precursor by measuring the deposition yield as a function of the PE energy. This is, however, not as straightforward as it seems.

Relevant for the deposition yield is the amount, the energy, and the location of the electrons that cross the target-vacuum interface. For flat surfaces, the energy spectrum of emitted electrons (BSEs, SEs) remains almost unaffected by the PE energy,<sup>94</sup> except for PE energies close to the SE peak [see Fig. 19(a)].<sup>95</sup> The most significant change is in the total yield of emitted electrons, which increases sharply to a maximum with increasing PE energy, after which it slowly decreases [see Fig. 19(b)]. This increase is mostly due to an increase in the amount of SEs. For PE energies close to the SE peak, the energy spectrum becomes dominated by the PEs.

The total flux of electrons is the sum of the PEs and the total yield of emitted electrons. When the deposition yield changes with changing PE energy, this can be the result of two parallel effects: (1) a change in cross section for dissociation by the PEs and (2) a change in the amount of emitted electrons. Since we want to determine the first effect, we need to have a measure or a model for the second effect. In addition, the model needs to be very accurate because most of the emitted electrons are SEs and the effect of the change in cross section may be relatively small. Building such an accurate model is not easy and it is made more difficult by the fact that the spatial distribution of PEs and emitted SEs varies strongly as a function of location on the substrate. For deposition with a focused beam, the incident PEs are concentrated in a small area, while the SEs are distributed over a much larger region. This becomes even more complex when tips are deposited. The balance between SEs, BSEs, and PEs can shift during the evolution of the tip. Moreover, there is the difficulty that in a typical experiment the PE energy is not the only parameter that is varied. In SEMs the beam size and/or the beam current usually changes together with the acceleration voltage.<sup>96</sup>

In deposition experiments, occasionally the electron cur-

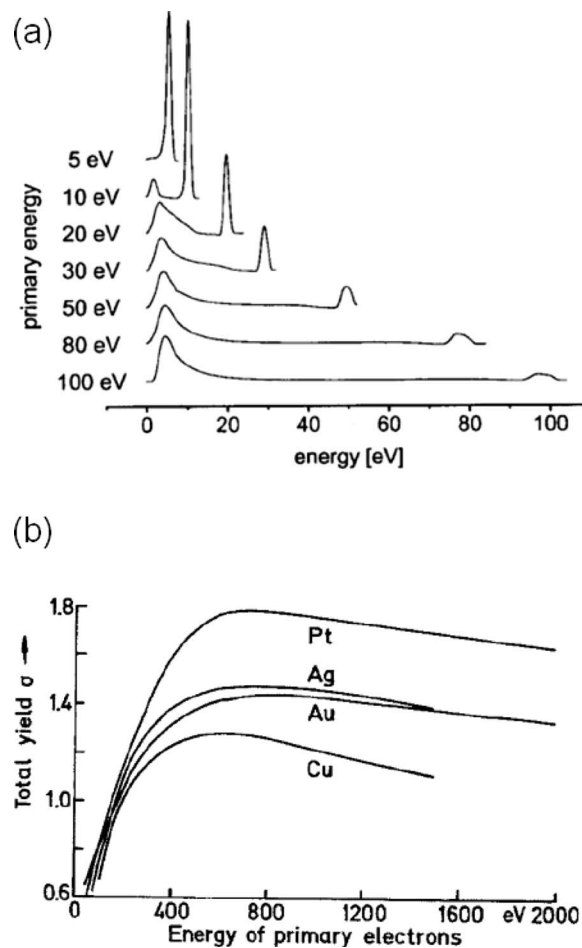


FIG. 19. (a) Energy spectrum of emitted electrons for various PE energies ranging from 5 to 100 eV. From Ref. 95. (b) Total yield of emitted electrons (BSEs and SEs) as a function of PE energy (from Ref. 43). Copyright © 1998 by Springer-Verlag. Reprinted with permission by Springer-Verlag.

rents are measured *in situ*,<sup>97,98</sup> but in general the yield of emitted electrons is not measured. Elaborate models are being developed<sup>57</sup> that can give valuable insight into how balances shift during deposit growth. However, it is still not straightforward to distinguish between the different mechanisms influencing the deposition process and to point out the prevailing one.

### 1. Height and width

Having put things in perspective, we will discuss results from experiments. Two types of behavior are observed when varying the PE energy. A decrease in deposit height with increasing PE energy is shown in Fig. 20(a)<sup>99–102</sup> and Fig. 20(b).<sup>103</sup> Data presented in some reports do not allow sufficient quantification to distinguish precisely this behavior but are consistent in the trend that the growth rate is higher at low voltages than at high voltages.<sup>16,22,72,104,105</sup>

A different type of behavior is shown in Fig. 21: An increase in the deposit height with increasing energy between 2 and 20 kV, after which the deposit height stays constant or shows a slight decrease.<sup>9,40,68,106</sup> In some cases,<sup>9,68</sup> this behavior is very consistent for different dwell times (seconds and minutes, respectively).

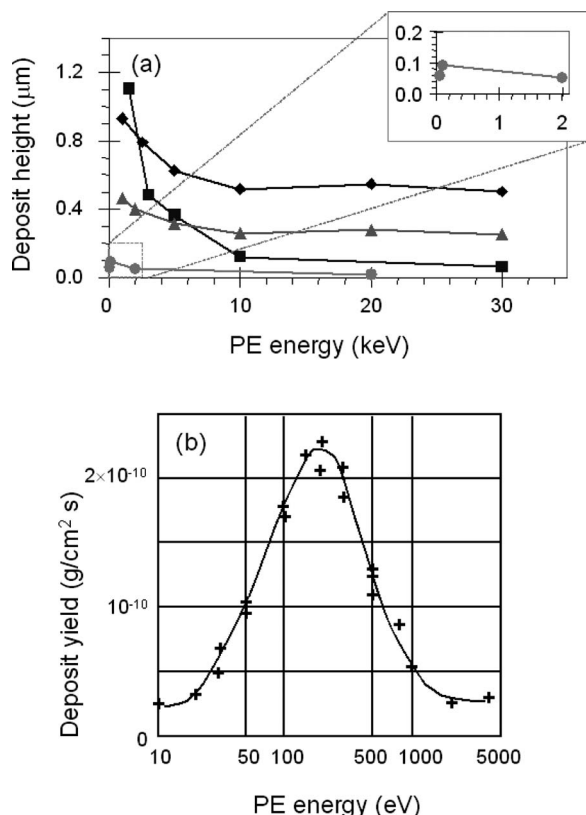


FIG. 20. (a) Deposit height as a function of the PE energy shows a similar dependence as the generation behavior of SEs. Inset shows the experiment by Hoyle *et al.* (Ref. 99) between 0.06 and 2 kV: (◆) Me<sub>3</sub>PtCp (Takai *et al.*, Ref. 100), (■) W(CO)<sub>6</sub> (Bauerdick *et al.*, Ref. 101), (gray triangle) Me<sub>3</sub>PtCp (Lipp *et al.*, Ref. 102), and (gray circle) W(CO)<sub>6</sub> (Hoyle *et al.*, Ref. 99). (b) The deposit yield in g cm<sup>-2</sup> s<sup>-1</sup> for diffusion pump oil as a function of PE energy. From Ref. 103.

The dependency of deposit height on PE energy in Fig. 20 seems to be consistent with the dependency of the yield of emitted electrons (BSEs and SEs) on PE energy in Fig. 19(b). Starting at PE energies of a few hundred eV, the deposition yield decreases strongly and becomes nearly constant for PE energies of 10–30 keV. This implies that in these experiments the deposit height was mainly dependent on the number of emitted SEs.

The results in Fig. 21 seem to be conflicting with this trend. An increase in the deposit height for higher PE ener-

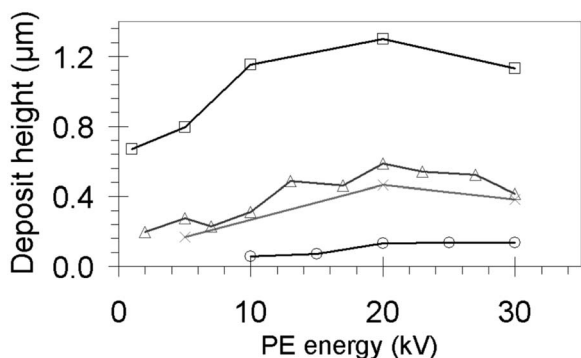


FIG. 21. Deposit heights as a function of PE energy: (□) contamination (Schiffmann, Ref. 9), (X) W(CO)<sub>6</sub> (Kohlmann-von Platen *et al.*, Ref. 68), (Δ) TEOS (Randolph *et al.*, Ref. 40), and (○) contamination (Miura *et al.*, Ref. 106).

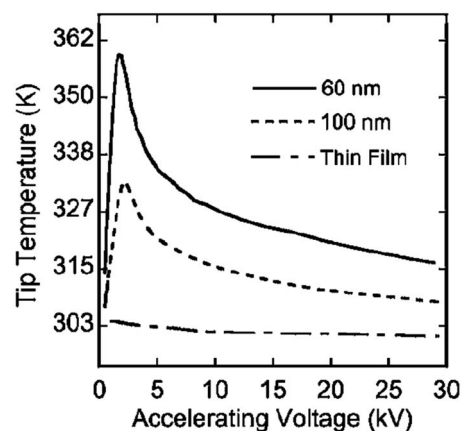


FIG. 22. Calculated temperature in tips (60 and 100 nm lengths) compared to a thin film. From Ref. 40.

gies is found, not a decrease. This can possibly be explained by the size of the interaction volume of scattered electrons in the target. As Weber *et al.*<sup>29</sup> pointed out, “the major difference when dealing with tips instead of flat substrates is the reduced scattering volume.” At high energies, the probability for a PE to exit the tip after a scattering event is significant because the tip is a high and narrow structure. At low energies, scattering occurs mostly within the tip, which can have e-beam induced heating as a result. Depending on the PE energy, the temperature rise can be as much as 50 °C, as becomes clear from a model by Randolph *et al.*<sup>40</sup> based on the effect suggested by Weber *et al.*<sup>29</sup> (see Fig. 22). Due to the temperature rise at lower PE energies, the residence time  $\tau$  of adsorbed precursor molecules decreases, which in turn leads to a lower vertical growth rate. This trend is consistent with the trend found in the experiments by Randolph *et al.*<sup>40</sup> (Δ, Fig. 21). The effect of beam induced heating would also explain the other results in Fig. 21. Kohlmann-von Platen *et al.*<sup>68</sup> (X, Fig. 21) deposited tips. For the experiments by Schiffmann<sup>9</sup> (□) and by Miura *et al.*<sup>106</sup> (○), we have already seen that beam induced heating most likely played a significant role during variations in the beam current (see Sec. IV A 1).

The trends in Fig. 21 may be explained with beam induced heating, but this explanation raises some questions for the trends observed in Fig. 20. Bauerdick *et al.*<sup>101</sup> (■, Fig. 20) and Beaulieu *et al.*,<sup>72</sup> Ding *et al.*,<sup>16</sup> and Croitoru *et al.*<sup>22</sup> (not shown) also deposited tips or dots and they measured a decrease in growth rate with increasing PE energy. This is in contradiction with the trend we would expect if the effect of beam induced heating was significant. For Bauerdick *et al.*,<sup>101</sup> this inconsistency can be explained by a different scan strategy. The tips were not grown by keeping the e-beam in a stationary position on the sample but by giving a series of short exposures. Between the exposures, there is time for the thermal energy to dissipate to the underlying substrate, so the effect of beam induced heating is expected to be much less. It is not possible to use this explanation for the results by Beaulieu *et al.*,<sup>72</sup> Ding *et al.*,<sup>16</sup> and Croitoru *et al.*<sup>22</sup> because they grew tips with the beam in spot mode. Due to lack of detailed information (local precursor pressure, beam currents used, etc.) this inconsistency remains unexplained. In con-

clusion, the combined model of (1) the correlation between deposition yield and SE yield and (2) beam induced heating seems to be valid for most experiments. However, it leaves some experimental results unexplained and the measurements are not sufficiently accurate to exclude the contribution from PEs to the growth.

As for the lateral dimensions, all measurements are influenced by the fact that the diameter of the PE beam changes with changing the electron energy. For the case where the beam diameter was measured, it was reported that there is little dependence of lateral dimension on e-beam energy.<sup>68</sup>

## 2. Composition and morphology

The results from articles reporting on the influence of the PE energy on the composition of deposits vary quite significantly. Details about the experiments are often not given, so the interpretation of the results is difficult. A clear influence of the PE energy was reported by Weber *et al.*<sup>29</sup> for a number of precursors [Me<sub>2</sub>-Au-tfac, Me<sub>2</sub>-Au-hfac, Me<sub>2</sub>-Au-acac, Mo(CO)<sub>6</sub>]. The metal content of tips increased with decreasing the PE energy. Numbers (compositions or PE energies) are not given. When irradiating condensed WF<sub>6</sub> layers in an Auger SEM, the dissociation rate was found to decrease with increasing beam energy.<sup>107</sup>

The behavior observed for the Au and Mo precursors was explained by the authors as resulting from “the cross section for inelastic scattering, which is increasing with decreasing electron energy.”<sup>29</sup> Most likely, they refer to the cross section for scattering of PEs, which is larger at lower PE energies. By this, they imply that the higher metal content of the tips at lower PE energies is the result of the larger abundance of SEs. In this picture, a decrease in PE energy is equivalent to increasing the accumulated charge per unit time. This mechanism would be consistent with the behavior observed for WF<sub>6</sub>.

In several other studies, no influence of the PE energy was found. Folch and Servat<sup>64</sup> reported that the composition of deposits from Me<sub>2</sub>-Au-hfac was constant for PE energies between 10 and 40 keV. For contamination deposits, the ratio between *sp*<sup>2</sup>- and *sp*<sup>3</sup>-bonded C was measured for PE energies between 3 and 20 keV.<sup>16</sup> Variations were below the uncertainty level of about 10% of the measurement technique [electron energy loss spectrometry (EELS)]. The diffraction patterns of 50 nm thick films deposited from W(CO)<sub>6</sub> obtained in the TEM showed no visible difference when fabricated with different beam energies.<sup>73</sup> Also the composition of rectangles deposited from (RhCl(PF<sub>3</sub>)<sub>2</sub>)<sub>2</sub> was found to be independent of the PE energy.<sup>108</sup>

The independence of the composition from PE energy for deposits Me<sub>2</sub>-Au-hfac found by Folch and Servat<sup>64</sup> is surprising since Weber *et al.*<sup>29</sup> did find a dependence for the same precursor.<sup>29</sup> According to Folch and Servat,<sup>64</sup> the observed lack of dependence “rules out the possibility that substrate heating by the impinging electrons plays a significant role in the deposition mechanism, as the heating effect increases with increasing energy.” It is not straightforward to see why this is so because it is not mentioned whether tips or squares are deposited. This would imply that in the results by

Weber *et al.*<sup>29</sup> e-beam induced heating *did* play a significant role. Keeping in mind the discussion in Sec. IV A 3 and the fact that Weber *et al.*<sup>29</sup> deposited tips, this sounds plausible. However, lack of information prevents conclusions that are more definite.

## 3. Conductivity

The inconsistency in the effect of the PE energy on the composition of deposits is also found for measurements of the conductivity. It was found for W(CO)<sub>6</sub> by Hoyle *et al.*<sup>99</sup> that the conductivity increases with decreasing energy (varied between 500 eV and 20 keV). This trend was confirmed for W(CO)<sub>6</sub> lines deposited with energies between 20 and 30 keV by Kohlmann-von Platen *et al.*<sup>90</sup> In contradiction with these results, the conductivity of lines deposited from trimethyl-platinum-methylcyclopentadienyl (MeCpPtMe<sub>3</sub>) decreased by a factor of 3 when the PE energy increased from 5 to 20 keV.<sup>109</sup>

These inconsistent results are difficult to explain. In all three cases, the deposits were created by scanning the pattern (lines or squares) a large number of times to obtain sufficient height. This, and the fact that low aspect ratio structures were used (instead of tips, for instance), makes the occurrence of e-beam induced heating in any of the experiments not very likely. Hoyle *et al.*<sup>99</sup> explained their results by assuming that SEs play a major role in the deposition process. At lower PE energies, precursor molecules undergo more collisions with electrons, increasing the desorption of volatile species and increasing the metal content. The same mechanism would have occurred for the Pt precursor, so that does not explain the difference. The contrasting results may be due to difference in precursor chemistry, but again, a mechanism is not easy to see.

## C. Conclusions

Regarding the vertical growth of deposits, measurements of the effect of the current density are mostly consistent with each other and with the existing growth model. The plot that gives most insight into the growth process is a measurement of *h* as a function of *J* (or *V*<sub>deposit</sub> as function of *I*). The e.l. and p.l. regimes can be identified and explained quantitatively (to some extent) for experimental results. An experiment with contamination indicates that a high *J* (or *I*) can lead to e-beam induced heating, which significantly affects the vertical growth rate. Often, the vertical growth is reported in terms of *h* as a function of *Q* or *t*<sub>dwell</sub>. For most of these cases, too much information is missing (such as the local precursor flux) to explain the observed behavior quantitatively and sometimes even qualitatively. Contradictory results were found for experiments where the influence of the PE energy on the vertical growth was studied. These contradictions could be explained largely with a combination of the growth model and beam induced heating, but this approach leaves some results unexplained. Unfortunately, there is not enough information available to find out why.

Concerning the lateral growth, this is consistently found to be independent of *J* and the PE energy. Instead, *d*<sub>deposit</sub> depends on *d*<sub>beam</sub> and on *Q* (for growth in the e.l. regime)

and shows a fast initial increase followed by saturation. This behavior can be explained by dissociation by SEs emitted from the growing deposit itself. Deposits with a  $d_{\text{deposit}}$  as small as 1.0 nm have been created by stopping the growth in the fast increase stage. At these dimensions, the number of molecules per deposit is so small that the effect of the counting statistics becomes visible.

For metal-organic precursors, an increasing  $J$  generally leads to an increase in metal content, conductivity, and density. Additionally, the deposit surface changes from smooth to rough. This is partially due to an increased degree of electron induced dissociation and partially due to a change in dissociation mechanism. At a high  $J$  beam induced heating can occur. If the precursor has a thermal decomposition temperature within the range of temperatures that can be reached by beam induced heating, the dissociation mechanism may not be merely electron induced but can also be thermally induced. For precursors with a thermal decomposition temperature well above temperatures reached with beam induced heating (such as TEOS), no effect of  $J$  is observed. Inconsistent results were found for the effect of the PE energy on the composition, morphology, and conductivity. It is suggested that beam induced heating or the amount of emitted SEs played a significant role during these experiments, but lack of information prevents definite conclusions.

## V. SCAN PATTERN AND SCAN STRATEGY

One of the advantages of EBID is that two-dimensional as well as 3D patterns can be defined. Apart from the prop-

erties of the beam (size, current, energy), the scan pattern as well as the scan strategy can have a significant influence on the deposit. A number of parameters are defined in the scan strategy. In the case of lines, for instance, the line length and the scan speed are most apparent parameters. Related to this is the period between subsequent visits of the same point on the substrate. This is known under several names: “repeat times,” “loop times,” “refresh times,” “line times,” or “delay times.” We will use the term loop time. Apart from these variables, the dose per scan can also be varied. For digital deflection systems, this is the number of pixels per line. These parameters can be interconnected (for instance, the scan speed and the loop time), so it requires some care to perform and describe experiments in such a manner that conclusions can be drawn from the results.

### A. Scan pattern

#### 1. Height and width

Until now, we have mainly discussed the deposition of tips by spot irradiation. Although this is perhaps conceptually the simplest deposition experiment, we have already seen that this can lead to a quite complex behavior. The fact whether the process is e.l. or p.l. can significantly influence the growth rate, the composition, and the morphology. Here we will see that it can also affect the height distribution of the deposit. In the extreme case, growth is p.l. almost directly from the start. An example is the use of residual gas as a (carbon) precursor. If a large beam is used, nonuniform

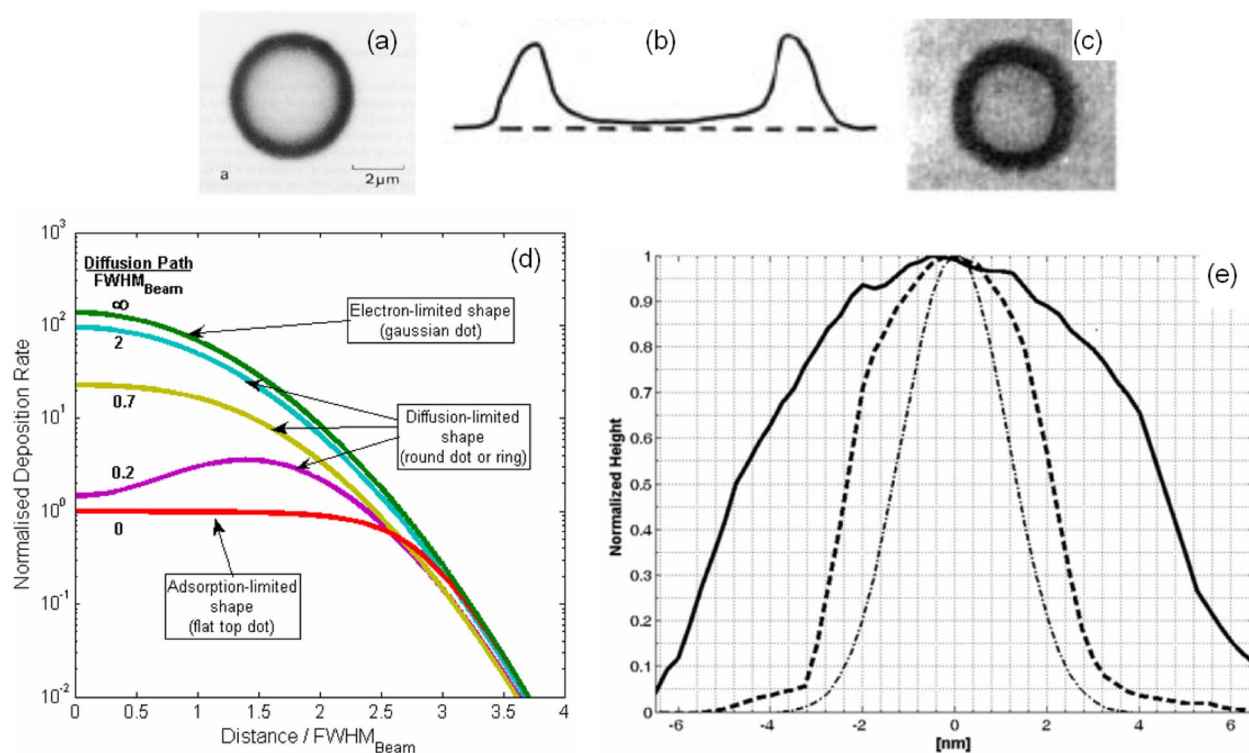


FIG. 23. (Color online) (a) Contamination ring as a result of broad beam illumination. From Ref. 111. Copyright © 1978 by Elsevier. Reprinted with permission by Elsevier. (b) Height profile and (c) contamination ring. From Ref. 110. (d) The growth rate as a function of the normalized distance with the beam in spot mode for different growth regimes, calculated from a continuum model. From Ref. 112. The p.l. regime is called diffusion limited. (e) Same as in (d) but now calculated from a Monte Carlo simulation. From Ref. 113. Copyright © 2007 by IOP Publishing Ltd. Reprinted with permission by IOP Publishing Ltd. The deposit profiles for the p.l. regime (—) and e.l. regime (— · —) are shown, together with the e-beam profile (— · —).

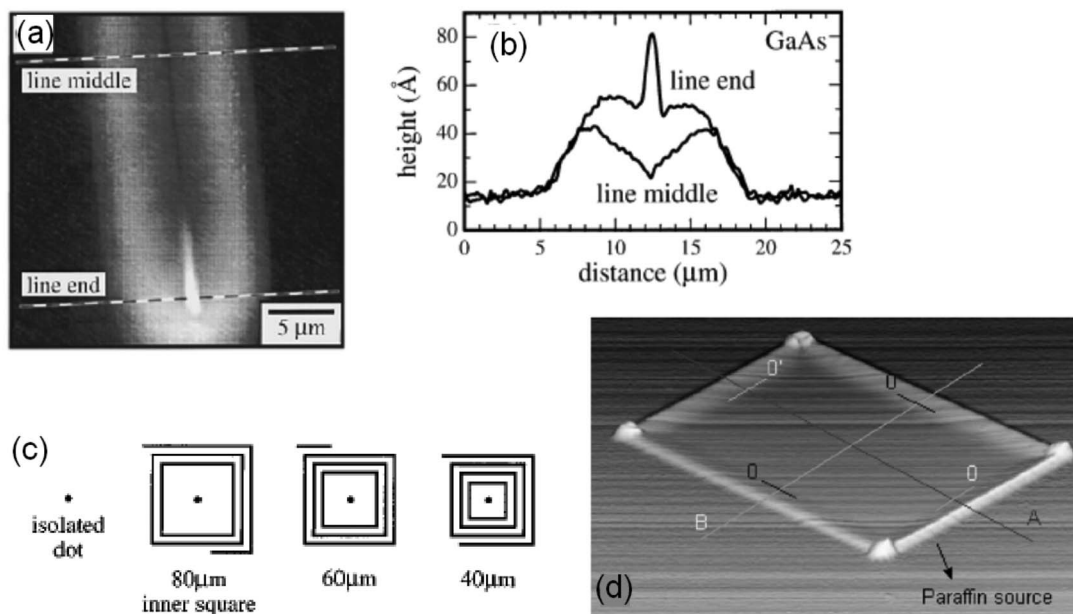


FIG. 24. Height profiles of deposits indicating that surface diffusion is the prevalent precursor supply mechanism. (a) AFM image of a line several micrometer wide. The line end has a different height profile than the line middle. (b) The absolute height profiles. (c) Test pattern to study the effect of surface diffusion. (d) Scanned square, where paraffin was used as precursor. (a)–(c) are from Ref. 114. (d) is from Ref. 16.

height distributions are found, as, for instance, reported by Fourie<sup>110</sup> and Reimer and Wächter.<sup>111</sup> They studied contamination growth in early electron optical systems. When irradiating a substrate with a beam with a diameter of some micrometers, deposition of carbon occurred only along the edge of the beam and not in the center. Typical deposit height profiles are shown in Figs. 23(a)–23(c).

The explanation for this behavior is as follows.<sup>111</sup> If  $gF/N_0 \ll \sigma J$  the area under the beam will quickly become depleted of mobile precursor molecules. The supply of new molecules will have to come from outside the irradiated area. If direct adsorption from the gas phase is the prevalent supply mechanism, all locations under the e-beam have an equal probability for adsorption (and dissociation). If surface diffusion is the prevalent supply mechanism, molecules will diffuse from the outside inwards and will be pinned down before they reach the center of the irradiated area. The fact that a ring structure is found indicates that (for these particular experimental conditions) surface diffusion was the prevalent supply mechanism.

The effect of the two growth regimes can be reproduced well with theoretical models. Results from a continuum model developed by Utke *et al.*<sup>112</sup> and a Monte Carlo simulation developed by Smith *et al.*<sup>113</sup> are shown in Figs. 23(d) and 23(e), respectively. The p.l. regime is called diffusion limited in Fig. 23(d). That the ring shape is not visible in Fig. 23(e) is probably because a very small beam diameter was used.

Similar results were later found experimentally in similar conditions for lines and squares. The middle sections of lines (deposited from contamination, several micrometer wide) showed a different height profile than the end sections.<sup>114</sup>

Figure 24(a) shows an atomic force microscopy (AFM)

image and Fig. 24(b) shows the height profiles. This indicates that the precursor supply is mainly by surface diffusion. The end sections have a larger area to draw hydrocarbons from than the middle section and therefore the end sections become higher than the middle section. The theory of supply by diffusion was tested with a dedicated experiment. Around a spot on the substrate, four lines were scanned that connected to make a square. The spot and the surrounding lines were irradiated in alternating sequence. While keeping the scan strategy (total accumulated charge, dwell times, loop times) constant for the dot in the middle, the influence of the presence and the length of the four lines was studied [see Fig. 24(c) for a schematic representation]. The height of an isolated dot was 209 nm, and this decreased to 139, 133, and 111 nm for squares of  $80 \times 80$ ,  $60 \times 60$ , and  $40 \times 40 \mu\text{m}^2$ , respectively. This result is consistent with the theory that the primary supply mechanism is diffusion over the surface.

The same conclusion was drawn by Ding *et al.*<sup>16</sup> after depositing squares using paraffin as a precursor. A small amount of paraffin was placed on a cleaned Si substrate and about  $35 \mu\text{m}$  away a square of several micrometer length and width was defined. The height profile of the resulting structure is shown in Fig. 24(d). The edges are thicker than the middle, and the four corners are again higher than the edges. This is consistent with the diffusion picture sketched above, where the supply of molecules is largest for the corners and smallest for the middle of the square.

## 2. Composition and morphology

We have seen strong indications in Sec. IV A 1 that e-beam induced heating can play a significant role in the deposition process. This happens when the energy input by the e-beam is larger than the energy dissipation from the

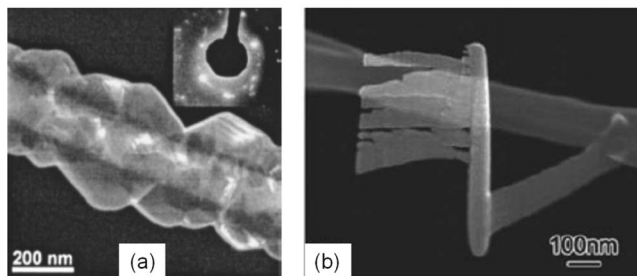


FIG. 25. (a) A self-standing rod after a point exposure at the end of the rod (not shown in the image). Initially, the rod consisted of an *a*-C-rich matrix with dispersed 2–5 nm Cu nanocrystals. As a result of the point the rod now consists of Cu crystals. From Ref. 115. (b) Structure deposited from  $W(CO)_6$  by Liu *et al.* (Ref. 116).

deposit, as we have seen for deposits created with the beam in spot mode. Further evidence for beam induced heating in other instances comes from an experiment by Utke *et al.*<sup>115</sup> Using hfac-Cu-VMTS as precursor, they created self-standing horizontal rods by scanning the beam (500 pA, 132 nm diameter) into vacuum from a copper substrate. The rods had a smooth surface, consisted of an amorphous C-rich matrix with dispersed 2–5 nm Cu nanocrystals, and had all precursor ligand elements (F, Si, O and C) present. The next step was to deposit a vertical tip at the end of the self-standing rod. Close to where the vertical tip was grown, the rod was fully transformed into >100 nm faceted Cu nanocrystals [Fig. 25(a)]. F, O, and Si had disappeared and the amount of C was greatly reduced. The explanation offered by the authors is that during the growth of the vertical tip, the amount of inelastic scattering becomes much higher than during the growth of the (relatively thin) self-standing rod simply because there is a larger volume of material under the beam. There will be a larger energy transfer from beam to target and due to the poor thermal conductivity there will be a temperature gradient over the rod. Near the vertical tip, the decomposition temperature of the precursor can be approached and faceted Cu crystals are the result.

Liu *et al.*<sup>116</sup> did a similar experiment, also with a 500 pA beam current but now with  $W(CO)_6$ , a PE energy of 200 keV, and a beam size of approximately 0.8 nm. They deposited self-standing sheets at the end of a pillar at the end of a self-standing rod [see Fig. 25(b)]. The entire deposit remains amorphous. Probably, the amount of energy transferred to the entire structure is much smaller than in the experiment by

Utke *et al.*<sup>115</sup> because the high-energy PEs have a much larger inelastic mean free path and scatter much less.

The composition of deposits from  $(RhCl(PF_3)_2)_2$  and  $(RhCl(CO)_2)_2$  appears to be unaffected by the scan pattern. Cicoira *et al.*<sup>108</sup> measured the composition for these precursors with Auger electron spectroscopy. Deposits were created with the beam (2 and 10 nA) in area mode and in point mode and analysis showed a homogeneous distribution of the elements, with a Rh content of around 60 at. %, indifferent of the scan pattern (or other parameters such as beam current or PE energy). Analysis of  $(RhCl(PF_3)_2)_2$  deposits by TEM and EELS confirmed this.<sup>117</sup>

## B. Scan strategy

### 1. Height and width

The scan strategy concerns parameters such as the dose per scan, dwell times, and loop times. Kohlmann-von Platen *et al.*<sup>90</sup> studied the effect of the dwell time and the loop time independently for depositions with the e-beam in spot mode. The precursor was  $W(CO)_6$  and the total accumulated charge per spot was kept constant. The deposit heights presented in Figs. 26(a) and 26(b) are normalized to a deposit height obtained with a continuous exposure (at the same accumulated charge). For a constant loop time, a decrease in dwell time from 150 to 20  $\mu$ s leads to an increased normalized yield from 1 to 2–2.5 [see Fig. 26(a)]. The decreasing yields at the longer dwell times are the result of “the progressing consumption of the adsorbate layer. The amount of decomposed precursor molecules per time unit is larger in the beginning than in later intervals of the dwell time.” In other words, the dissociation rate during an exposure period is not constant but decreases because the surface coverage  $N$  decreases. At a constant dwell time, an increase in loop time from 0 to 150  $\mu$ s leads to an increase in normalized height from 1 to around 2, respectively [Fig. 26(b)]. The higher yields at the longer loop times are due to the longer precursor replenishing times. The appearance of a saturation level for the yield indicates that  $N$  becomes constant at the higher loop times. At those loop times, the yield becomes independent of the dwell time.

Other studies where the loop time was varied confirm this proposed model. Similar behavior was found for squares deposited from TEOS (Ref. 118) and lines and dots depos-

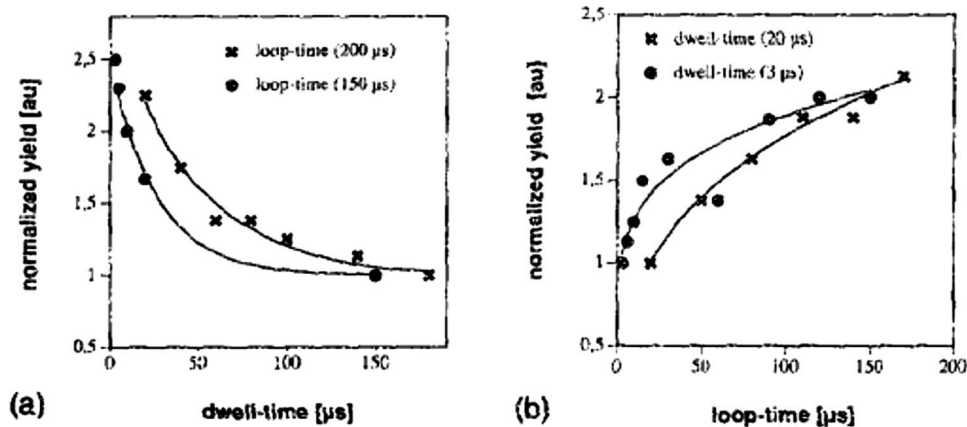


FIG. 26. The results from independent variations in the (a) dwell times and (b) loop times for tip deposits from  $W(CO)_6$ . The accumulated charge was kept constant. Yields were normalized to the yield of a tip deposited with a continuous exposure (at the same accumulated charge). From Ref. 90.

ited from contamination.<sup>114</sup> Beaulieu *et al.*<sup>72</sup> did not give exact numbers but did report that an increase in loop time by a factor of 4 gives an increase in vertical growth rate of a factor of 4. It is interesting that, for the different experiments, saturation of the deposition yield for the longer loop times occurs at different time scales. While saturation occurs in the order of 100–200  $\mu\text{s}$  in the experiments by Kohlmann-von Platen *et al.*,<sup>90</sup> Lipp *et al.*<sup>118</sup> found time scales of 10–20 ms and Amman *et al.*<sup>114</sup> found time scales in the order of 20 s. This must be due to differences in  $F$ . Amman *et al.*<sup>114</sup> used contamination as a precursor and are therefore dependent on surface diffusion as supply mechanism (see also Sec. IV A 1). Kohlmann-von Platen *et al.*<sup>90</sup> and Lipp *et al.*<sup>118</sup> both reported an  $F$  of  $10^{17}$  molecules  $\text{cm}^{-2} \text{s}^{-1}$ . The difference between the results by Kohlmann-von Platen *et al.*<sup>90</sup> and Lipp *et al.*<sup>118</sup> are possibly due to the sticking coefficients of the precursors [ $\text{W}(\text{CO})_6$  and TEOS, respectively].

Results are less consistent when the dwell time is varied. Sanchez *et al.*<sup>119</sup> mentioned (without giving absolute numbers) that short dwell times are beneficial for a high growth rate when scanning squares, similar to what Kohlmann-von Platen *et al.*<sup>10</sup> found. On the other hand, Lipp *et al.*<sup>118</sup> found that the effect on the deposition yield was less pronounced than in the experiments by Kohlmann-von Platen *et al.*<sup>90</sup> This may be because the dwell times may have been too short. The current density Lipp *et al.*<sup>118</sup> used was smaller than what Kohlmann-von Platen *et al.*<sup>90</sup> used (10 instead of 75  $\text{A cm}^{-2}$ ), which means that one would expect that depletion occurs at longer dwell times [i.e., the curve in Fig. 26(a) shifts to the right]. However, Lipp *et al.*<sup>118</sup> used shorter dwell times (0.5–2  $\mu\text{s}$ ), where depletion may not have occurred at all. Beaulieu *et al.*<sup>72</sup> reported that the dwell time did not appear to be significant at all. This can perhaps be explained by the fact that Beaulieu *et al.*<sup>72</sup> used dwell times in the range of 5–500 ms, much longer than in the experiments by Kohlmann-von Platen *et al.*<sup>90</sup> or Lipp *et al.*<sup>118</sup> It is possible that the deposition area was depleted from precursor molecules even at the smallest dwell times.

In some cases, the way the experiment is performed does not allow a full interpretation of the influence of dwell and loop times. For instance, when scanning a line with constant length and with constant total accumulated charge, the dose per scan (in  $\text{C m}^{-2}$ ) was varied.<sup>120</sup> Effectively, this results in the simultaneous variation in both the dwell time per point and the loop time. Another example is a variation in the “line dose” (in  $\mu\text{C cm}^{-1}$ ) without keeping the total accumulated charge constant.<sup>71</sup> The simultaneous variation in several parameters prevents the determination of the influence of individual parameters such as dwell and loop times.

There are two reports of a dependency of the line width on the dwell and loop times. For contamination lines, a decrease in the loop time leads to a different height profile.<sup>114</sup> Figure 27(a) shows profiles of lines written with loop times of 100.2, 30.6, 20.2, and 5.2 s (constant dwell time); a schematic is shown in Fig. 27(b). At the shorter loop times, the surface diffusion length is not sufficient to supply the central part of the line with contamination molecules and deposition only occurs at the edge of the structure. Beaulieu *et al.*<sup>72</sup>

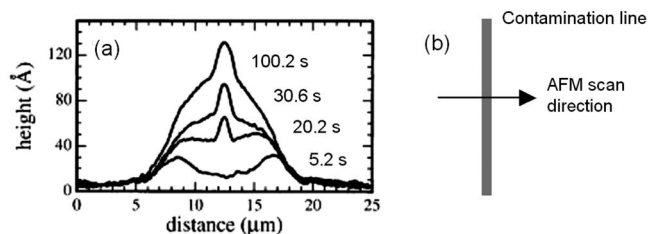


FIG. 27. (a) The height profiles of contamination lines deposited with different loop times (at constant dwell time). The loop times are indicated in the figure. From Ref. 114. (b) Schematic of the setup.

mentioned that a combined increase in dwell time and loop time gave a definite decrease in line width. However, since further details are not mentioned, it remains unclear why this is so.

## 2. Conductivity

Hoyle *et al.*<sup>120</sup> have written 30  $\mu\text{m}$  lines with  $\text{W}(\text{CO})_6$  with a total dose of  $5 \times 10^5$   $\text{C m}^{-2}$ , while the scan speed and corresponding number of scans were varied. Effectively, this results in a corresponding simultaneous variation in both the dwell time per point and the loop time. Measurements of the resistivity show two regimes. For fast scans (doses less than about 500  $\text{C m}^{-2}$ , relatively short dwell and loop times), a high resistivity deposit is found, while for slow scans (doses larger than about 5000  $\text{C m}^{-2}$ , relatively long dwell and loop times) a low resistivity is found. The authors described these two regimes as “electron-flux limited” and “gas-flux limited.” In the gas-flux limited regime, “each deposited molecule undergoes a larger number of electron collisions while at the surface, and this may result in additional desorption of CO” and therefore contribute to a lower resistivity.

This model is confirmed by experiments by Hiroshima and Komuro<sup>71</sup> for  $\text{WF}_6$  and Utke *et al.*<sup>121</sup> for  $\text{Me}_2\text{-Au-tfac}$ . Hiroshima and Komuro<sup>71</sup> reported that a single slow scan yielded a line with lower resistivity than 200 fast scans. Similarly, Utke *et al.*<sup>121</sup> kept the total line dose constant and tried a single slow pass (9  $\text{nm s}^{-1}$ ) versus  $6 \times 10^5$  fast passes (500  $\mu\text{m s}^{-1}$ ) per line. The resistivity is about 60 times higher for the fast scan (with relatively short dwell and loop times) than for the single slow scan (with relatively long dwell and loop times).

In conclusion, the trend seems to be that the effect of the scan strategy on the conductivity is dependent on the ratio between electrons and deposited molecules. If this ratio increases (more electrons per deposited molecule), the dissociation of molecules will be more complete and the conductivity will increase.

## C. Scan speed

If a line is scanned by the e-beam in a single pass and the scan speed is increased from 0  $\text{nm/s}$  onwards, a transition will be observed from pillar growth to line deposition. First studied by Koops *et al.*<sup>67</sup> and Mølhave *et al.*,<sup>122</sup> the evolution of the growth behavior is well presented in Figs. 28(a) and 28(b).<sup>123</sup> As the scan speed is increased (increasing from a to l), the structures become increasingly inclined. At the same time, a second deposit starts to grow on the substrate, which

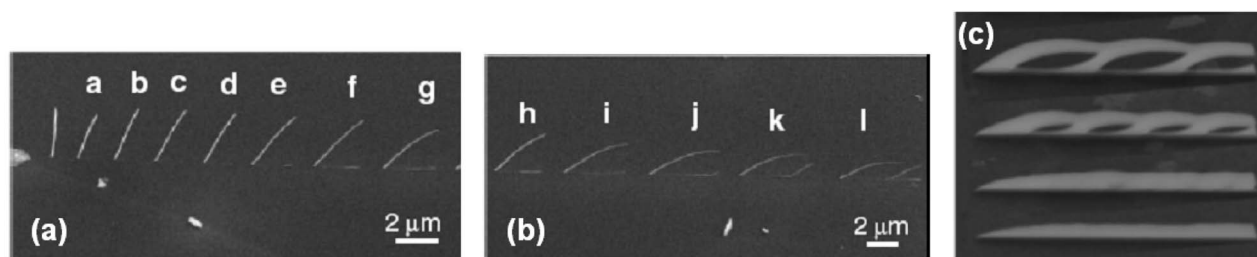


FIG. 28. [(a) and (b)] The inclination of tips as a function of the scan speed. From Ref. 123. At sufficiently large scan speeds, secondary deposits start to grow (starting from pillar e and f onwards). (c) At increased scan speeds, fencelike structures and finally solid lines are deposited. From Ref. 124.

becomes visible from pillar d or e onwards in Fig. 28(a). As the pillar becomes increasingly inclined, the second deposit can also “take off” from the substrate [illustrated by k and l in Fig. 28(a)]. If the scan speeds are increased even further, periodic fencelike structures and finally solid lines [see Fig. 28(c)] are deposited.<sup>124,125</sup> Based on an extensive study, it was found that the growth of these secondary structures and the periodic growth is caused by the decreasing precursor supply efficiency to the end of the inclined pillar. As a result of the increased diffusion path, the flux of precursor molecules reaching the end of the pillar decreases and the tip becomes thinner and narrower. From a certain scan speed onwards, the e-beam can penetrate the inclined pillar and create a second deposit on the substrate. As the primary pillar becomes thinner and thinner, more electrons penetrate and the vertical growth rate of the secondary structure increases. Finally, the primary and the secondary structure meet. The process then repeats itself. If the scan speed is increased, the thinning of the primary pillar and the growth of the secondary structure start earlier and the periodicity becomes smaller. Finally, a flat line is scanned.

A few other cases are known of secondary structures growing parallel to freestanding primary structures.<sup>122,126</sup> It is likely that this is caused by the PEs getting through to the underlying substrate.

The influence of the scan speed has also been studied for very high-resolution ( $<10$  nm width) self-standing structures. When the e-beam is scanned over a hole, a self-standing rod will grow. It is consistently reported that the width of the rods (dimension perpendicular to the e-beam and the scan direction) decreases with increasing speed of the e-beam.<sup>127,128</sup> See also Fig. 29(a). The width at scan speeds above  $\sim 10$  nm  $s^{-1}$  saturates at 7–10 nm. The width evolution of the rods is roughly similar to the evolution of dots as proposed by Silvis-Cividjian *et al.*<sup>56</sup> If the e-beam irradiates each position on the rod for a longer time, more SEs are emitted at the side of the rod and it becomes wider. The  $1/(\text{scan speed})$  relationship seems to indicate that the amount of material that is deposited per unit time remains constant for scan speeds up to 10 nm  $s^{-1}$ .

Apart from the width of the rods, the angle of inclination of the rods also appears to be dependent on the scan speed.<sup>127</sup> The angle between the substrate and rod decreases with increasing scan speed. For scan speeds of 0.8, 4, and 24 nm  $s^{-1}$ , the angles of inclination were  $+55^\circ$ ,  $0^\circ$ , and  $-15^\circ$ , respectively. The authors explained this with the (digitized) step sizes of the e-beam, which are made smaller when

the scan speed is decreased. It is assumed that a Gaussian shaped e-beam (0.8 nm diameter) creates Gaussian shaped deposits at each step of the e-beam. In Fig. 29(c), a schematic is depicted for three scan speeds: 0.8, 4, and 24 nm  $s^{-1}$ . At every new step, the beam is positioned somewhere on the slope of the already existing deposit. For a low, intermediate, or high scan speed, this position is above (position A), around (position B), or below (position C) the initial height of the substrate. Hence, the inclination of the rods is dependent on the scan speed. Similar results were found by Mølhave *et al.*<sup>122</sup> for depositions in an environmental SEM.

## D. Writing direction

### 1. Height

It has been observed that the writing direction with respect to the precursor source can be of influence on the vertical growth rate. The effect of the position of the gas nozzle was tested by depositing lines at a constant speed.<sup>129</sup> At the starting position of the line, a tip with constant height was deposited. The line was written from this tip toward the nozzle or from this tip away from the nozzle (see Fig. 30). Considerably more material was deposited when the beam was scanned toward the gas nozzle than when it was scanned away from the gas nozzle, although the final line height remains constant. This dependency of the vertical growth rate on the orientation with respect to the nozzle was also found for other patterns. The proposed explanation is that the coverage of precursor molecules is not constant over the surface of the tip. The side of the tip facing the gas nozzle has a higher coverage of precursor molecules than the side of the tip away from the gas nozzle. This shadowing effect causes the lower growth rate for the line that was written away from the gas nozzle. Estimations of the precursor coverage  $N$  in the shadowed areas based on the kinetic theory of gas quantitatively agree with the experimental results.

A similar dependency was observed in an experiment where the precursor supply was mainly by diffusion over the surface instead of through the gas phase.<sup>16</sup> A small amount of paraffin was placed on a Si wafer and used as a precursor for the deposition of a square about 35  $\mu\text{m}$  away. A complete AFM image of this square is shown in Fig. 24(d) and the height profile over line A in that figure is shown in Fig. 31. It shows that the side closest to the paraffin source (O) is higher than the side furthest away from the paraffin source (O').

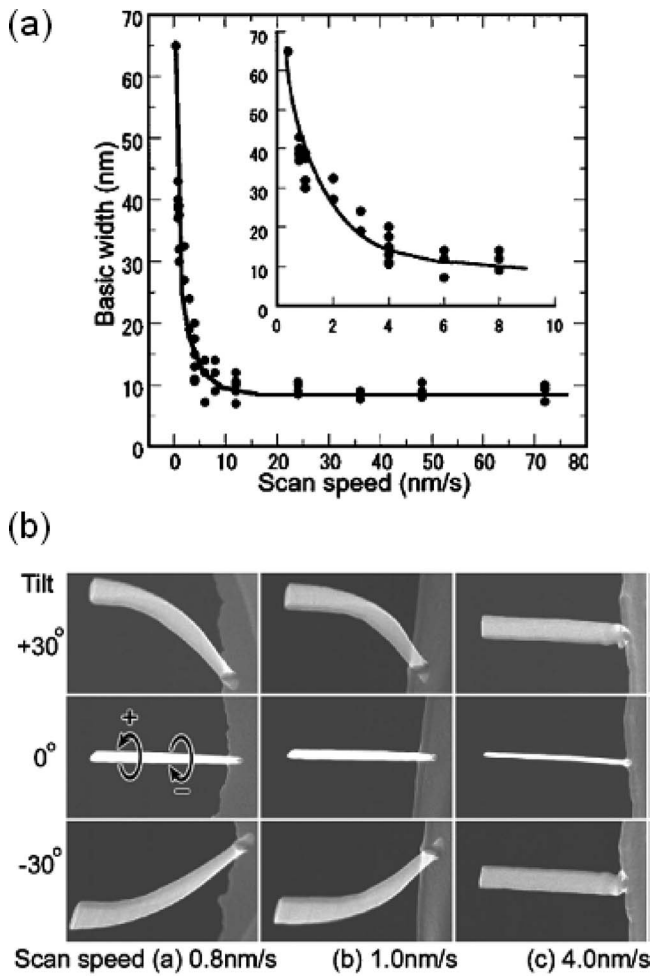


FIG. 29. (a) Width dependence of self-standing rods as a function of the scan speed. (b) The dependence of the angle of inclination on the scan speed. (c) Schematic of the effect of changing the scan speed. From Ref. 127.

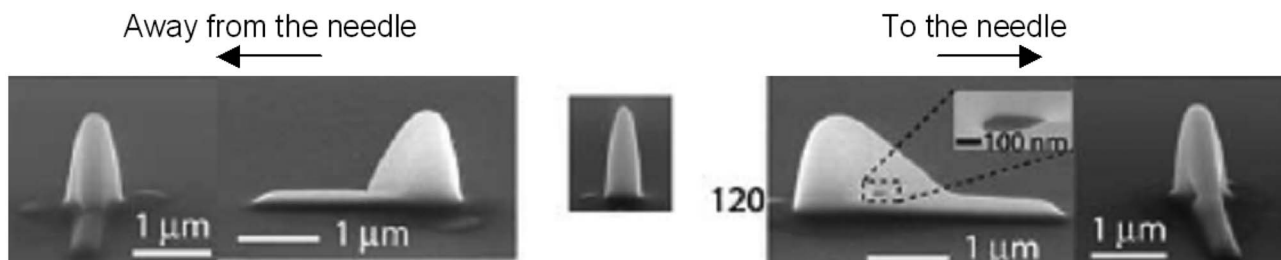


FIG. 30. The effect of the writing direction with respect to gas nozzle. A tip was deposited, followed by a line deposition. When the line was written away from the nozzle, significantly less material was deposited than when the line was written toward the nozzle. From Ref. 129. Copyright © 2005 by Elsevier. Reprinted with permission by Elsevier.

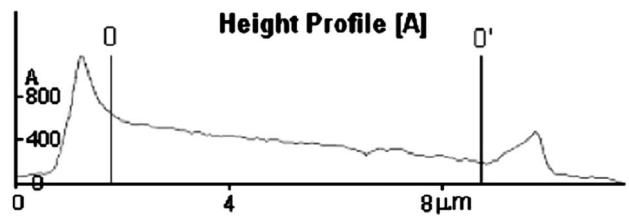


FIG. 31. Height profile of a square, demonstrating the influence of the direction of the precursor supply. The precursor source was located about 35 μm away, on the left side of O. From Ref. 16.

## 2. Composition and morphology

The position of the gas nozzle with respect to the deposit can influence the deposit morphology, as can be seen in lateral cross sections taken from tips deposited from  $\text{Co}_2(\text{CO})_8$ .<sup>87</sup> For the image in Fig. 32, the gas nozzle was positioned on the right side. A cobalt-poor region is found in the area toward the gas nozzle, consisting of Co nanocrystals embedded in a matrix of *a*-C. This cobalt-poor region is asymmetrically surrounded by a crust with larger Co grains (see also Fig. 16). In Sec. IIIB2, it was explained that the core/crust effect was probably due to e-beam induced heating. The authors suggested that the Co-poor region is directed toward the gas nozzle as a consequence of a cooling effect of the arriving precursor molecules. The cooling effect is absent on the side of the tip that is shadowed from the gas nozzle and there beam induced heating leads to the larger Co grains in the surrounding crust. The shadowing effects can also lead to void formation in tips deposited with a high beam current (82 nA).

## E. Proximity effects

### 1. Deposit location

A proximity effect is strictly speaking not really a parameter that can be varied, such as the beam current or the PE energy. However, a significant number of proximity effects have been reported until now for EBID, arising from different causes. Since these effects can significantly influence the final deposit shape or deposit distribution over the surface, we feel that a dedicated section is justified. Proximity effects are well known in resist based e-beam lithography. It is usually caused by BSEs and presents itself as an extra and unintentional exposure of the resist layer surrounding the irradiated areas. Several types of proximity effects have al-

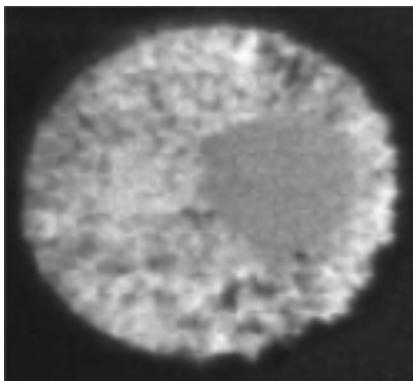


FIG. 32. Lateral cross section demonstrating the influence of the direction of the gas nozzle. A Co-poor region is found off center, on the side facing the precursor supply. From Ref. 87. Copyright © 2005 by Wiley-VCH Verlag GmbH & Co. KgaA. Reprinted with permission by Wiley-VCH Verlag GmbH & Co. KgaA.

ready been reported for EBID, where matters are more complicated because the irradiated targets are growing and therefore change in shape.

An effect similar to that in e-beam lithography, here called the “BSE proximity effect,” was reported by, for instance, Lau *et al.*,<sup>8</sup> Boero *et al.*,<sup>31</sup> and Edinger *et al.*<sup>26</sup> Extra deposition can be observed as a halo around the base of tips [Fig. 33(a)] or around lines [Fig. 33(b)]. In Fig. 33(b), the width of the halo was much larger on the SiO<sub>2</sub> than on the (prefabricated) pure Au pads. This is consistent with the larger backscatter range of the incident PEs for SiO<sub>2</sub> than for Au. Since the backscatter range is (among others) dependent on the energy of the incident PEs, working at low acceleration voltages is beneficial in reducing this proximity effect.

There is a proximity effect that is similar to the BSE proximity effect except for the fact that it causes parasitic deposition on larger length scales. It was observed when a tall tip was grown on a substrate on which small Si particles were scattered.<sup>65</sup> Parasitic deposition was observed in the entire area surrounding the tip but not in locations directly behind the Si particles [see Fig. 34(a)]. This excludes the BSE proximity effect since that causes radially decreasing yet uniform parasitic deposition. Here, the parasitic deposition is caused by the spraying of high-energy electrons that are scattered in the growing tip. These electrons have a much larger range than BSEs and will be blocked by obstacles in their path (such as Si particles). Although strictly speaking any electron that has undergone a scattering event and has an energy >50 eV is defined as a BSE, this effect is here called the “FSE proximity effect.” A few articles report parasitic deposition that can probably be attributed to this proximity effect. Zhang *et al.*<sup>130</sup> observed parasitic deposition on very thin electron transparent membranes, where the substrate is too thin for BSEs to play a significant role [see Fig. 34(b)]. Secondary ion mass spectroscopy (SIMS) performed by Gopal *et al.*<sup>109,131</sup> showed that Pt was distributed around a tall tip in an area many tens of micrometer wide [see Figs. 34(c) and 34(d)]. They explained this by thermally assisted diffusion of dissociated species over the surface. Under influence of beam induced heating of the grown tip, the lifetime of dissociated precursor molecules would then be sufficient to

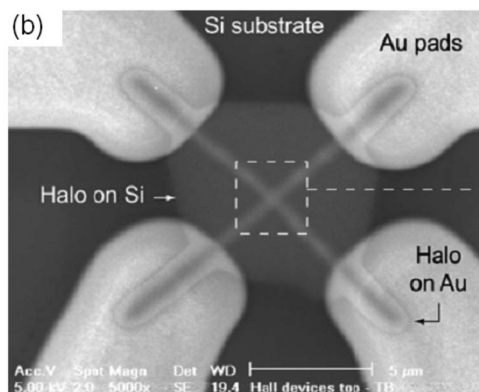
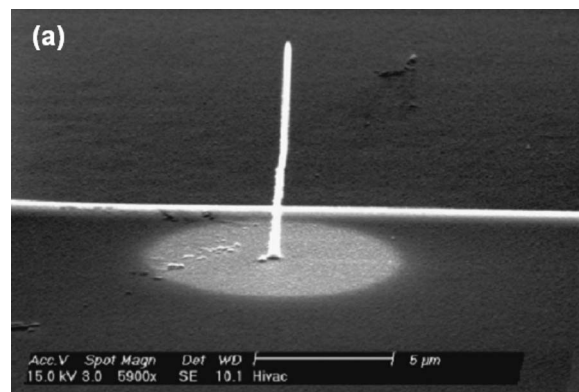


FIG. 33. Examples of a proximity effect as it is known in e-beam lithography. (a) A halo around a deposited tip. From Ref. 8. In the article, no comment is given on the presence of the white line in the image. (b) A halo around deposited lines. From Ref. 86. Reprinted with permission from author. The width of the halo is larger on the Si than on the Au.

diffuse over large distances. We think, in the light of the above-described experiments, that it is more likely that the parasitic deposition is the result of the FSE proximity effect.

Several authors reported a type of proximity effect where parasitic deposition occurred on already existing structures when new deposits were created in the close vicinity. This was found for self-standing rods,<sup>132,133</sup> dots,<sup>8</sup> and tips.<sup>122</sup> Aristov *et al.*<sup>133</sup> observed that the upper rod in Fig. 35(a) thickened as result of the fabrication of the lower rod, even though the deposition parameters were identical. Lau *et al.*<sup>8</sup> deposited an array of dots with constant dwell time and observed that the dots written earlier in the array were considerably thicker [Fig. 35(b), array written from top to bottom, left to right]. Aristov *et al.*<sup>133</sup> suggested that the extra deposition is caused by SE spraying from the structure that is being fabricated. This effect is here called the “SE proximity effect.” In reality, the energy of the electrons is not measured and in principle, this unintentional growth can also be caused by >50 eV electrons which are scattered or generated in the newly grown structure. It is therefore possible that there is no fundamental difference between the FSE and the SE proximity effects.

Hiroshima and Komuro<sup>71</sup> and Van Dorp *et al.*<sup>134</sup> reported studies on a proximity effect that is different from the proximity effects discussed until now in the sense that it affects the structures that are being written instead of the structures that are already present at the time of writing. The amount of

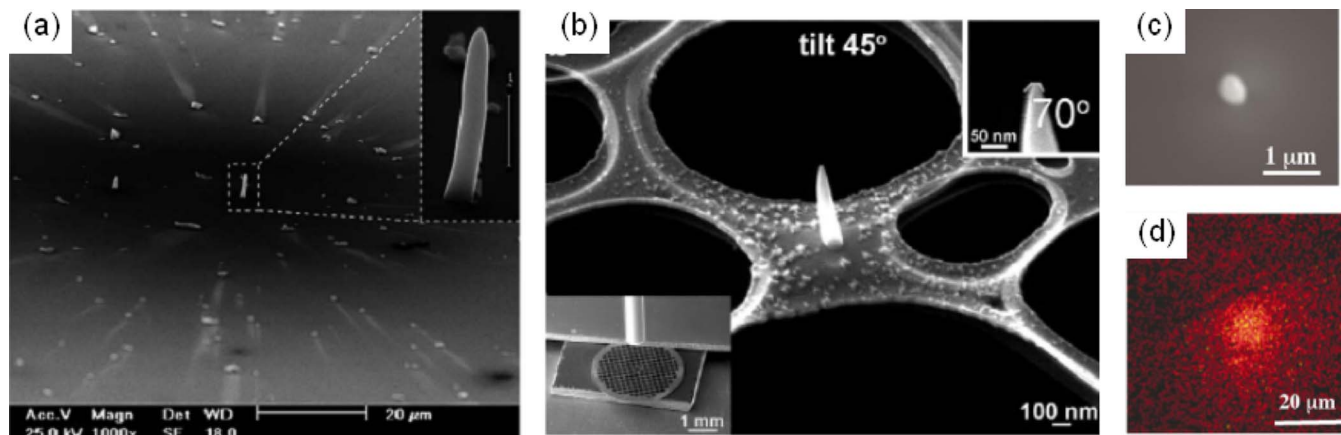


FIG. 34. (Color online) (a) The shadowing effect of PE scattering from a growing tip ( $[\text{IrCl}(\text{PF}_3)_2]_2$ ) can be observed behind the surrounding Si particles. From Ref. 65. Copyright © 2006 by Elsevier. Reprinted with permission by Elsevier. (b) Growth of Fe crystals around a growing tip, deposited from  $\text{Fe}(\text{CO})_5$ . From Ref. 130. Copyright © 2006 by Wiley-VCH Verlag GmbH & Co. KGaA. Reprinted with permission by Wiley-VCH Verlag GmbH & Co. KGaA. (c) SEM image of a tip deposited from a Pt precursor. (d) The SIMS map shows a wide spread of Pt deposition in the area surrounding the dot. From Ref. 109.

material that is deposited under the e-beam (excluding parasitic deposition as a result of the proximity effects described above) appears to be larger when the e-beam irradiates the side of an already existing structure than when it irradiates a flat area on the substrate. Hiroshima and Komuro<sup>71</sup> observed a surprisingly high vertical growth rate when depositing lines in a single slow line scan [Fig. 36(a)], while Van Dorp *et al.*<sup>134</sup> observed an increase in the amount of deposited material when writing parallel lines with constant dwell time at a spacing of roughly the same magnitude as the width of the lines [Fig. 36(b)]. The amount of deposited material is found to be proportional to  $1/\sin \alpha$ , where  $\alpha$  is the angle between the substrate and the e-beam. The effect is called here the “slope dependent proximity effect.” Van Dorp *et al.*<sup>134</sup> found a good (qualitative) correlation between the SE emission from the irradiated structure and the extra amount of growth due to the proximity effect. However, this does not necessarily imply that the extra deposition is caused by enhanced SE emission from the sidewall of the irradiated structure. When one pictures the adsorbed precursor molecules as a uniform adsorbent layer, the probability for dissociation by PEs increases with decreasing  $\alpha$  due to the enhanced path length through that adsorbent layer.

In general, the deposition is assumed to be primarily the result of dissociation by electrons. Experiments by Aristov *et al.*<sup>133,135</sup> indicated that surface plasmons can also contribute

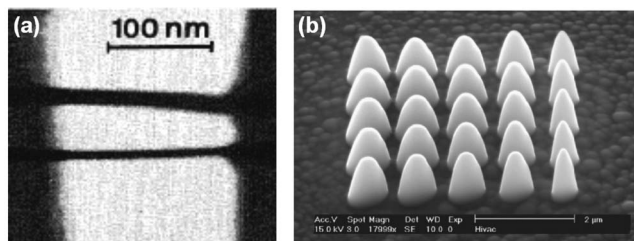


FIG. 35. Examples of the SE proximity effect. (a) During the writing of the second (lower) rod, the first (upper) rod became thicker. From Ref. 133. Copyright © 1992 by EDP Sciences. Reprinted with permission by EDP Sciences. (b) An array of dots, written from top to bottom, left to right. With the deposition of every new dot, previously written dots have become thicker. From Ref. 8.

to the growth of deposits. When positioning a stationary  $\sim 1$  nm beam about 35 nm away from the edge of an Fe film [circle in Fig. 37(a)], a protrusion grew away from the edge into the e-beam after an irradiation time of 160 s [Fig. 37(b)]. EELS measurements suggested that the protrusion consisted of carbon [solid spectrum in Fig. 37(c)]. When the EELS spectrum was recorded while the e-beam was positioned about 10 nm away from the protrusion, a peak of energy losses around 18 eV was observed [dotted spectrum in Fig. 37(c)]. This value is clearly different from the plasmon loss

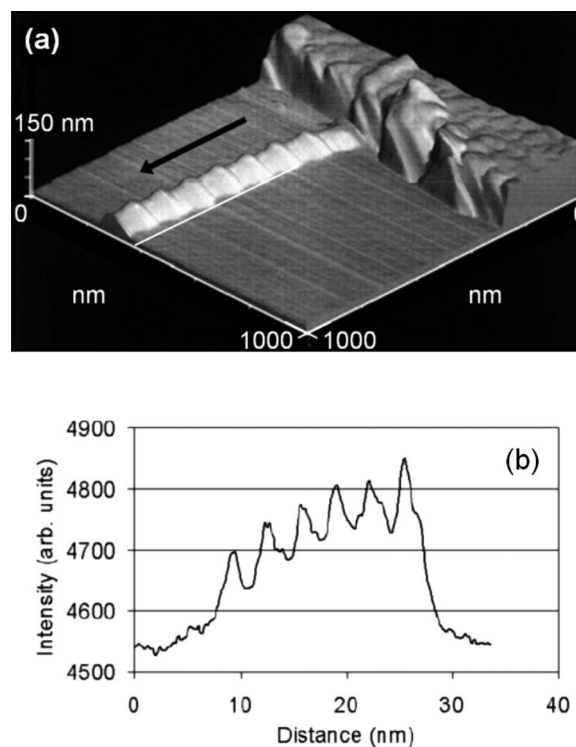


FIG. 36. (a) AFM image of a wire composed of stitched 80 nm long segments. At each start of each new stitch, extra material was deposited even though the accumulated charge was constant over the entire segments. From Ref. 71. Copyright © 1998 by IOP Publishing Ltd. Reprinted with permission by IOP Publishing Ltd. (b) Proximity effect as observed by Van Dorp *et al.*. Lines were written from left to right. From Ref. 134.

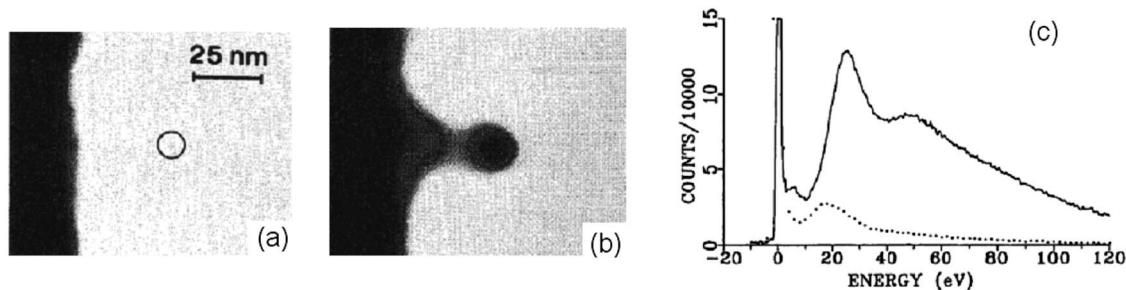


FIG. 37. An example of a proximity effect caused by surface plasmons. (a) Situation before and (b) after the e-beam was positioned in the circle. (c) The EELS spectrum when the e-beam is positioned on the protrusion (solid line) and 10 nm away from the protrusion (dotted line). The peak just below 20 eV is indicative of surface plasmons. From Ref. 133. Copyright © 1992 by EDP Sciences. Reprinted with permission by EDP Sciences.

energy for the carbon (25 eV) and indicates that surface plasmons (whose maximum energy for *a*-C is 17.7 eV) are responsible for the growth of the protrusion.

A proximity effect that is fundamentally different from all other types of proximity effect discussed until now was observed by several authors.<sup>122,135,136</sup> It was observed that (initially straight) tips can bend when a new deposit is fabricated in the direct vicinity. This deformation can also occur during irradiation without precursor gas present and the bending of the pillar is generally in the direction toward the irradiated neighboring area. Figure 38(a) shows two pillars that are bent plastically as a result of postdeposition irradiation. Mitsubishi *et al.*<sup>136</sup> concluded that the deformation was the result of charging. During the deposition of the second (lower) rod in Fig. 38(b), electrons are emitted from the second rod itself. This leads to positive charging of the second rod, while the first rod is negatively charged. The opposite charges lead to deformation. Repeating the writing of the same pattern on a conducting Au-coated carbon substrate showed that this deformation proximity effect did not appear [Fig. 38(c)]. This indicates that the bending and plastic deformation are caused by charging. Another strategy of avoiding the charging proximity effect is to use an alternating scan sequence, where the desired structures are grown simultaneously by scanning alternately.

## 2. Composition and resistivity

It is interesting to note that the composition of the parasitic deposits resulting from the different types of proximity effects can be quite different from the intended primary deposit. Lau *et al.*<sup>8</sup> found a lower Co concentration in the parasitic deposits that were the result of the BSE and/or the SE proximity effect. The parasitic deposits typically have about 8 at. % Co, whereas the primary deposit contains 35–45 at. % Co. The lower metal content in the parasitic deposits drastically influenced the measured resistivity of arches over two electrodes that were fabricated with EBID [Fig. 39(a)]. The arches were written by irradiating the two legs in alternating sequence with decreasing spacing. While irradiating one leg, parasitic material was deposited on the other. The measured resistivity decreased significantly when tips were deposited, from which the authors concluded that the parasitic deposit has caused the high resistivity of the arches. Consistent with these observations, Molhave *et al.*<sup>15</sup> found a lower metal content in the parasitic deposits of the SE proximity effect. A layer with very low gold content

formed on already deposited tips at the side that faced the irradiated spot nearby. In contrast to these findings, Zhang *et al.*<sup>130,138</sup> and Shimojo *et al.*<sup>74</sup> found the parasitic growth of bcc  $\alpha$ -Fe crystals when irradiating a small area on *a*-C membranes for prolonged dwell times (40–60 min) in the presence of  $\text{Fe}(\text{CO})_5$  [Fig. 39(b)]. The presence of deposits outside the irradiated primary area can be explained with the FSE proximity effect.

It is surprising that the metal content is lower in the parasitic deposit (compared to the primary deposit) when using  $\text{Co}_2(\text{CO})_8$  or  $\text{Me}_2\text{-Au-acac}$  and higher when using  $\text{Fe}(\text{CO})_5$ . For  $\text{Fe}(\text{CO})_5$ , Zhang *et al.*<sup>130</sup> explained this by the time dissociated molecules have to rearrange into a more energetically favorable position. Precursor molecules that are dissociated in the primary irradiation area (the growing tip) do not get enough time to rearrange because of the large number of PEs that impinge on a small area, and therefore the tip becomes amorphous. In the surrounding area, the current density on the substrate as a result of the FSE proximity effect is much less and dissociated precursor molecules get more time to rearrange.

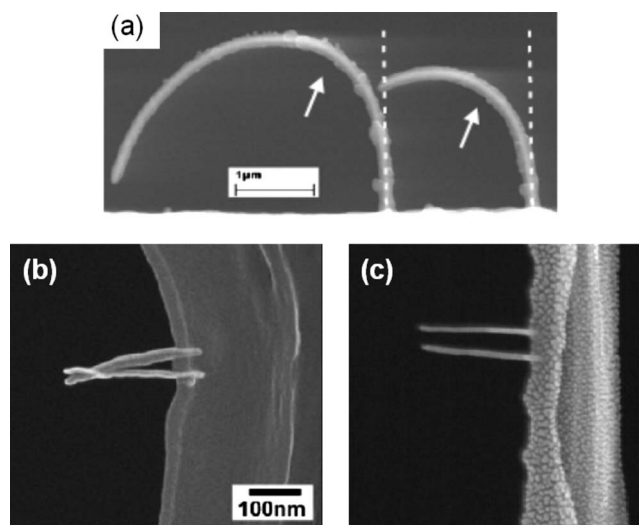


FIG. 38. (a) Deformation by postdeposition imaging. From Ref. 122. Copyright © 2004 by IOP Publishing Ltd. Reprinted with permission by IOP Publishing Ltd. (b) Deformation of the upper rod as a result of the fabrication of the lower rod. (c) The deformation in (b) can be prevented by writing the pillars in an alternating pattern or by using a conductive substrate. (b) and (c) are from Ref. 136. Copyright © 2006 by the Institute of Pure and Applied Physics. Reprinted with permission by the Institute of Pure and Applied Physics.

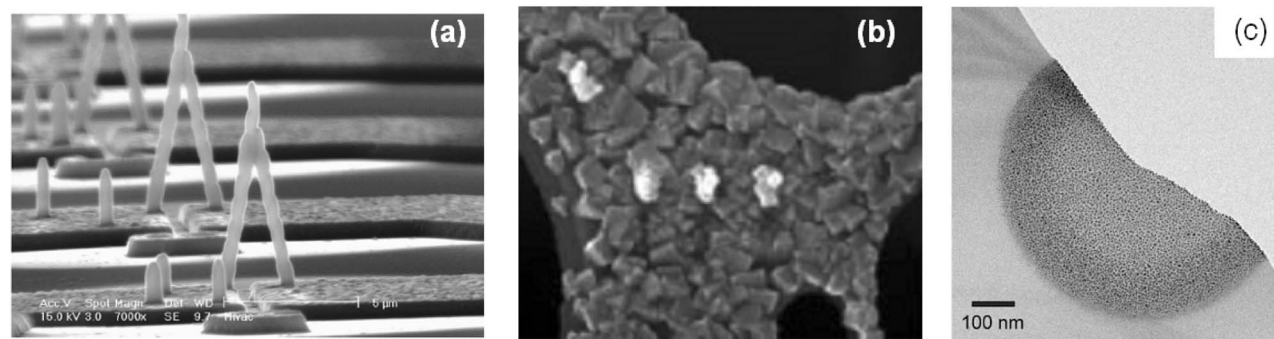


FIG. 39. (a) Measurement of the conductivity of deposits from  $\text{Co}_2(\text{CO})_8$ . From Ref. 8. (b) Around three intentionally deposited tips, the parasitic deposition of Fe crystals was found. From Ref. 130. Copyright © by Wiley-VCH Verlag GmbH & Co. KGaA. Reprinted with permission by Wiley-VCH Verlag GmbH & Co. KGaA. The precursor was  $\text{Fe}(\text{CO})_5$ . (c) Cluster formation for broad beam deposition from  $\text{Me}_2\text{-Au-acac}$ . From Ref. 137.

There is some evidence to support this mechanism.  $\text{Fe}(\text{CO})_5$  is known to thermally decompose at temperatures as low as room temperature<sup>139</sup> or autocatalytically in the presence of Fe.<sup>140</sup> In addition, an indication of the mobility of dissociated precursor molecules comes from an experiment by Ketheranathan *et al.*<sup>137</sup> with  $\text{Me}_2\text{-Au-acac}$  in a TEM. While irradiating the sample with a broad beam, cluster growth was observed in the bright field transmission images [Fig. 39(c)]. The clusters nucleated, increased in size, and sintered during the deposition process. This behavior suggests that dissociated precursor molecules diffuse over the surface to more energetically favorable positions. Similar mechanisms may have occurred during the parasitic depositions with  $\text{Fe}(\text{CO})_5$ .

For the Co and Au precursors, the mechanism might have been different. The thermal decomposition temperatures are well above room temperature and although autocatalytic decomposition has been reported for  $\text{Co}_2(\text{CO})_8$  (see also Sec. IIIB2), this still requires a temperature of about 60 °C.<sup>141</sup> This temperature was not reached for the parasitic deposits nor for the primary deposits (judging from the absence of anomalously high growth rates such as in Fig. 15). Therefore, the Co or Au content of the parasitic deposits is perhaps a base value, which can become higher in the primary deposit due to the higher current density (more electrons to induce the desorption of fragments) or due to modest beam induced heating.

## F. Conclusions

In experiments where the main precursor supply mechanism is diffusion, the central part of a pattern can become depleted of molecules and fresh precursor molecules diffusing inwards are dissociated on the edge of the pattern. These effects are well reproduced by a continuum model and a Monte Carlo simulation reported in literature. The deposit composition and morphology will only be affected by the scan pattern if e-beam induced heating occurs. Beneficial for a high vertical growth rate is a scan strategy where dwell times are short and loop times are long. Beneficial for a high conductivity is a scan strategy where dwell times are long and loop times are short. The two competing processes are on the one hand a high probability for an electron to dissociate a precursor molecule and on the other hand a large number of electrons per precursor molecule to achieve a high

degree of fragmentation. The deposit height profile will be affected if loop times are so short that the surface is not replenished and growth is p.l. This will result in deposition on the edge of the pattern, not in the central part.

If a line is scanned in a single pass and the scan speed is increased from 0  $\text{nm s}^{-1}$  onwards, a transition will be observed from pillar growth to line deposition. This transition involves the growth of periodic, fence-like structures. This behavior is explained by variations in the balance between the vertical growth rate and the length of the precursor diffusion path. For high-resolution self-standing deposits, the width and the inclination of the lines depend on the scan speed.

The writing direction with respect to the precursor source can affect the vertical growth rate for micrometer-sized deposits. The side of the structure facing the precursor source has the highest vertical growth rate. During deposition where beam induced heating occurs and the precursor is supplied by a gas nozzle, the arriving precursor molecules can have a cooling effect. This is shown to have an effect on the deposit morphology.

Six types of proximity effects are identified and explained. These effects cause parasitic deposition (on ranges varying from nanometers to tens of micrometers), affect the deposition rate of the primary deposit, or cause deformation of neighboring deposits. It is observed that the composition, morphology, and conductivity of parasitic deposits can be dramatically different from the primary deposit. There are indications that mechanisms such as beam induced heating and autocatalytic decomposition were involved, but conclusive evidence is missing.

## VI. ADDITIONAL CIRCUMSTANCES

### A. During experiments

#### 1. Substrate heating

*a. Height and width.* Substrate heating has been shown as early as 1960 to have a large influence on the vertical deposition rate. The deposit heights as a function of the temperature (at constant accumulated charge) are shown in Fig. 40. The overall trend is that the deposit height decreases with an increasing substrate temperature.

As discussed in Sec. III C, a higher temperature will lead to a smaller residence time  $\tau$ , hence a smaller probability that

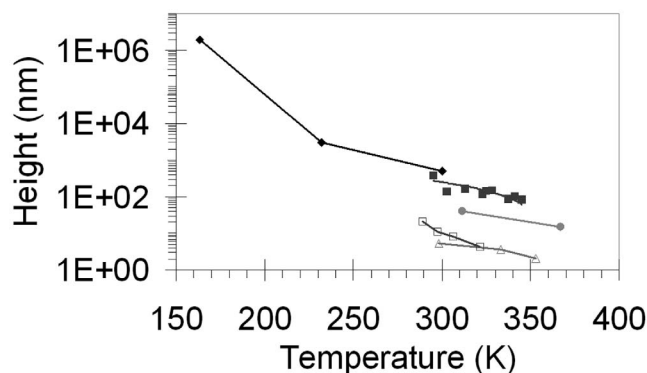


FIG. 40. Deposit height as a function of temperature: ( $\blacklozenge$ )  $\text{WF}_6$  (Matsui and Mori, Ref. 142), ( $\blacksquare$ )  $\text{WF}_6$  (Randolph *et al.*, Ref. 40), (gray circle) TMA (Ishibashi *et al.*, Ref. 143), ( $\square$ ) alkylnaphthalene (Ishibashi *et al.*, Ref. 143), and ( $\triangle$ ) contamination (Christy, Ref. 2).

a precursor molecule is dissociated. Hence, the deposit height decreases. This trend is consistent with nearly all reported results in Fig. 40 and qualitatively confirmed by some authors.<sup>11,25,144</sup> Li and Joy<sup>63</sup> showed that this model is valid only for a specific regime: the e.l. regime. For low beam currents (51 pA in this experiment) the deposition yield was only a function of  $\tau$ . At high beam currents (403 pA and higher) a p.l. regime was reached. The dissociation rate on the top of the tip was now a function not only of  $\tau$  but also of the diffusion length of precursor molecules and the spatial distribution of the electron emission sites on the tip sidewall.

Another factor that can complicate the deposition behavior at nonambient temperatures is the precursor chemistry. This is what Matsui and Mori<sup>142</sup> ( $\blacklozenge$ , Fig. 40) observed when they deposited W from  $\text{WF}_6$  on  $\text{SiO}_2$  in the temperature range of  $-110$  to  $160$  °C. For temperatures below  $50$  °C, the relatively simple relationship described above (a decrease in growth rate with an increase in temperature as a result of shorter residence times) was valid. However, at temperatures above  $50$  °C etching of the substrate occurred instead of deposition. The authors explained their results by assuming that the induced process involved both deposition and etching at all temperatures, and that the etching became the most influential process above  $50$  °C. The sensitivity of the precursor chemistry to the combination of substrate and precursor becomes clear from the fact that Li and Joy<sup>63</sup> did not observe any etching of the Si substrate by  $\text{WF}_6$  at temperatures above  $50$  °C.

If the substrate temperature is high enough, thermal decomposition can occur parallel to electron induced decomposition. For instance, for  $\text{Fe}(\text{CO})_5$  only electron induced decomposition is found at room temperature, while at  $250$  °C pure thermal decomposition is found. At an intermediate temperature ( $125$  °C), a combination of electron induced and thermal decomposition was found<sup>140</sup> and the deposition efficiency was anomalously high (40 molecules per PE). This appeared to be due to catalytic effects since small deposits continued to grow after the electron flux had stopped. Similar combinations of electron and thermally induced decomposition can also lead to the oriented growth of small crystals. When irradiating a Si(111) substrate, kept at temperatures between  $400$  and  $600$  °C, in the presence of  $\text{Fe}(\text{CO})_5$ , small iron silicide rods (length of  $10$ – $80$  nm, width

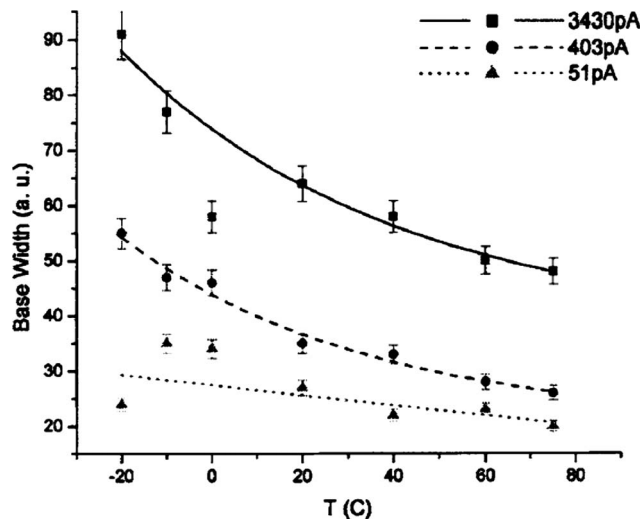


FIG. 41. Relative width of a tip as a function of temperature for different beam currents. From Ref. 63.

of  $5$ – $10$  nm) developed along step edges.<sup>145,146</sup> While the width of the rods stayed constant, the length of the rods increased with increasing dwell time.

Finally, at low temperatures condensation effects can occur. Ochiai *et al.*<sup>147</sup> observed that at a temperature of  $-12$  °C so much material (other than the intended film) was deposited that the pattern written with the e-beam could not be seen anymore. The authors mentioned that the condensation seems to be “enhanced by the e-beam irradiation” but gave no further details.

A direct influence of the temperature on the width of deposited pillars is not observed. Kohlmann-von Platen *et al.*<sup>68</sup> measured the dependence of the deposit width on substrate temperature but found no significant effect. Li and Joy<sup>63</sup> did observe an effect, but that was indirectly the result of the growth regime. At high beam currents, the top of the pillar becomes depleted of precursor molecules and diffusion over the sidewalls of the pillar becomes the main source of precursor supply to the top. At lower temperatures, many of the molecules diffuse onto the pillar but are dissociated before they reach the top. At higher temperatures, the diffusion speed increases and fewer molecules are dissociated on the sidewalls. As a result, the pillar width increases with decreasing temperature (see Fig. 41).

*b. Composition and morphology.* Nearly all experiments where the metal content of the deposit was studied as a function of the substrate temperature show a consistent trend: a higher temperature leads to a higher metal content. Figure 42 shows the results for  $\text{WF}_6$ ,<sup>142</sup>  $\text{Me}_2\text{-Au-tfac}$ ,<sup>85,148</sup>  $\text{Pt}(\text{PF}_3)_4$ ,<sup>62</sup> and trimethyl gallium (TMG) in combination with cracked  $\text{AsH}_3$ .<sup>144</sup>

This trend will be caused partially by the fact that the amount of adsorbed contamination (from the residual gas) decreases with temperature. Nevertheless, there are also precursor specific differences. The effect of substrate heating is very strong for the Au and Pt precursors. Wang *et al.*<sup>62</sup> suggested that the higher metal content at higher temperatures in their experiments is the result of the increased desorption of volatile groups. While electrons usually only affect the P–F bond (see also Sec. VIII B), the raised temperature could

increase the probability that the complete  $\text{PF}_3$  ligand is removed after electron impact. Another (possibly parallel) mechanism is that atoms or fragments that are separated after electron impact desorb more easily at higher temperatures and are not trapped in the deposit. A similar mechanism could perhaps also explain the strong increase in metal content as a function of temperature for the Au precursor and the somewhat smaller increase in metal content in the deposits from TMG and cracked  $\text{AsH}_3$ .

The effect of the temperature is rather weak for depositions with  $\text{WF}_6$ . F is hardly detected (2% or less) for the temperature range used in the experiment.<sup>142</sup> Apparently, F is volatile enough to desorb completely even at low temperatures, in contrast to fragments of precursors described above. The other components in the deposit are C and O, most likely originating from the residual gas.

*c. Conductivity.* If the general trend is that the metal content increases with increasing substrate temperature, then one would expect that the conductivity of deposits also increases. There are not many articles reporting measurements of the resistivity of the deposit as a function of the temperature during deposition, but the available reports are consistent with this hypothesis. A resistivity of  $10^{-4} \Omega \text{ cm}$  was measured for deposits from  $\text{Me}_2\text{-Au-tfac}$  at  $80^\circ \text{C}$ ,<sup>148</sup> while this was  $10^{-2} \Omega \text{ cm}$  at room temperature.<sup>29</sup> In another report, a decrease in resistivity of a factor of 2 was reported for the same precursor when the substrate temperature was increased from room temperature to  $60^\circ \text{C}$ .<sup>121</sup>

## 2. Tilting during deposition

In general, depositions are done with the sample surface perpendicular to the focused e-beam. There are two reports where the effect of tilting of the sample on the deposition rate has been measured. Using  $\text{Fe}(\text{CO})_5$  as a precursor, the deposition rate on a Au substrate was studied for two angles:  $90^\circ$  and  $30^\circ$  (angle between the beam and substrate). The deposition rate increased from  $8.5 \times 10^{-4}$  to  $1.2 \times 10^{-3}$  atoms/ $e^-$ , respectively, a factor of around 1.4.<sup>140</sup> Under the same conditions, the SE emission increased by a factor of 2. In another study, specific numbers were not men-

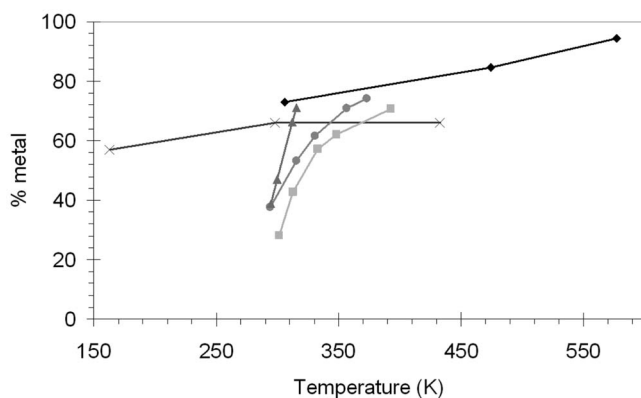


FIG. 42. The temperature dependence of the metal content: ( $\blacklozenge$ ) TMG and  $\text{AsH}_3$  (Takahashi *et al.*, Ref. 144), ( $\times$ )  $\text{WF}_6$  (Matsui and Mori, Ref. 142), (gray circle)  $\text{Me}_2\text{-Au-tfac}$  (Koops *et al.*, Ref. 148), (gray triangle)  $\text{Me}_2\text{-Au-tfac}$  (Weber *et al.*, Ref. 85), and (gray square)  $\text{Pt}(\text{PF}_3)_4$  (Wang *et al.*, Ref. 62).

tioned, but the deposition yield and the SE yield showed a similar dependence on the angle between the beam and specimen.<sup>102</sup>

These results are an indication that there is a correlation between the SE yield and the deposition yield. We have seen more indications of this in Secs. IV B 1 and V E 1, for instance. However, it needs to be remarked that, although there is a correlation, these experiments do not give direct evidence that the deposition is caused merely by the SEs. Similar to the argument used for the slope dependent proximity effect (discussed in Sec. V D 1), one can argue that the adsorbed precursor molecules form a layer covering the substrate. The length of the trajectory that the incident PEs travel through that layer increases with  $1/\sin \alpha$  which is roughly similar to the angular dependence of the SE yield.

## 3. Biasing sample during deposition

In an attempt to fabricate narrower structures, Yavas *et al.*<sup>149</sup> positively biased the sample to suppress the emission of SEs (no numbers given). The authors reported that the pillar width was not affected by the bias.

That the expected result was not obtained by biasing the sample is not surprising. The experiment was performed assuming that the SEs play a significant role in the deposition process. Supposing this assumption is correct, it is not straightforward to see how the bias would exactly influence the deposition process. In the first place, the emission of SEs may not have been suppressed. There is no electric field inside a conductor, so SEs will only be influenced by the electric field once they exit the sample. The bias affects the electron trajectories (redirecting them toward the sample) but does not suppress the emission of SEs. In practice, the deposit is not a perfect conductor, so the electric field will penetrate the deposit. However, it is not clear to what extent this will influence the emission of the SEs. In the second place, SEs may not even need to exit the substrate in order to dissociate an adsorbed precursor molecule. It is conceivable that DEA or DD is possible when SEs approach the adsorbed molecule from the bulk of the substrate without actually exiting the material. Therefore, without a better understanding of the influence of a bias on the SE behavior, this experiment is not very useful.

## B. Postdeposition treatment

### 1. Extra irradiation

Postdeposition treatments are usually applied to improve the properties of the deposit and to remove unwanted fragments. One way to do this is to expose the deposit to a high current beam after the precursor supply has been stopped. This extra exposure can have various effects, such as graphitization. When exposing *a*-C deposits from contamination in the SEM to an 80 keV beam in a TEM for several minutes, a significant part of the *a*-C was transformed into graphite.<sup>20</sup> Other types of morphological change are also possible: the surface of a tip ( $\sim 8 \mu\text{m}$  high, deposited from  $\text{hfac-Cu-VTMS}$ ) changed from smooth to rough when the apex of the tip was observed with a high current beam.<sup>86</sup> Interestingly, this change occurred over the entire surface of the tip even

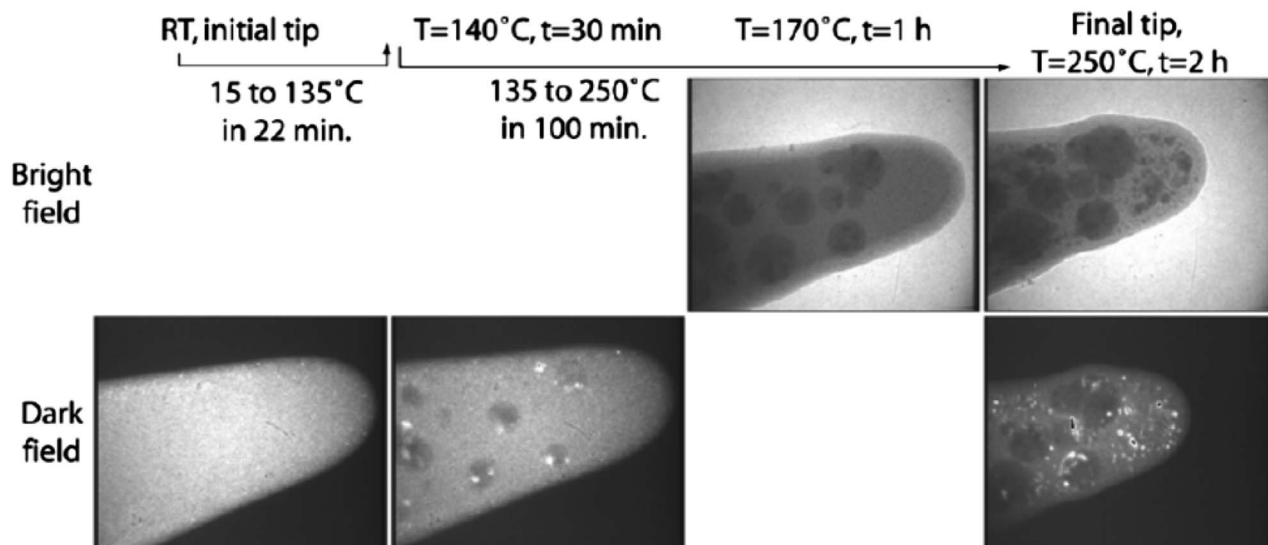


FIG. 43. Annealing of a rod deposited from hfac-Cu-VTMS. From Ref. 86. Reprinted with permission from author.

though only the top part was irradiated (the tip was viewed under a tilt angle of  $70^\circ$ ). Apart from affecting the morphology, postdeposition irradiation can also affect the conductivity. For deposits from  $\text{Fe}_3(\text{CO})_{12}$ , it was reported that “additional irradiation of high-resistance lines (preliminarily deposited at low beam current values) at high  $I$  values leads to a considerable increase in the conductivity of lines.”<sup>91</sup> Similar results were found for deposits from  $\text{W}(\text{CO})_6$ , where the resistivity decreased with a factor of 20.<sup>73</sup> Finally, postdeposition irradiation can be used to sculpt a deposit. A free-standing wire with about 10 nm width was grown in the SEM (from TEOS), after which the wire was exposed to a 200 keV high current e-beam in a TEM. The irradiation caused a relative increase in the Si content and a decrease in the width of the wire down to 1 nm before finally breaking.<sup>150</sup>

The effect of the extra exposure can be the result of several (parallel) mechanisms. It can be the completion of the (initially) partial decomposition of the precursors or the formation of volatile components with the help of residual background gases. The change in the morphology of the copper tip seems to indicate that the influence of e-beam induced heating can be significant because the bottom of the tip was affected without having been exposed (after deposition) to the e-beam. For the experiments in the TEM, knock-on damage by high-energy ( $>50$  keV) electrons is a likely mechanism behind the changes in properties especially since it strongly affects light elements in the target.

## 2. Annealing

*a. Composition.* Apart from an extra postdeposition exposure, the deposit properties can also be improved by annealing. Freestanding, amorphous rods [deposited from  $\text{Fe}(\text{CO})_5$  on Si] changed into single-crystal  $\alpha$ -Fe when annealed under UHV conditions at a temperature of  $600^\circ\text{C}$ .<sup>151–153</sup> Carbon and oxygen were hardly detected in the annealed rods and the shape remained almost unchanged. When repeating this procedure for deposits grown on a carbon grid, the deposits contained iron carbide or polycrystalline  $\alpha$ -Fe. Apparently,

material from the substrate moves into the final deposit during annealing. The incorporation of elements from the substrate was also found for thin  $a$ -C films deposited on Si(100) from ethylene. At temperatures above 1170 K, the  $a$ -C film turned into SiC.<sup>154</sup>

In other cases, crystals in an amorphous matrix are formed. After *in situ* annealing of self-standing deposits created from  $\text{Cr}(\text{CO})_6$ ,  $\text{W}(\text{CO})_6$ , and  $\text{Re}_2(\text{CO})_{10}$  nanocrystals ( $\sim 20$  nm in size) formed.<sup>155</sup> Electron diffraction of the crystals showed that the rhenium deposits contained pure Re crystals. For the other two materials, various phases were present, among others carbides. The growth of crystals was also found after the annealing of a rod deposit from hfac-Cu-VTMS.<sup>86</sup> Initially, the tip was smooth and showed uniform contrast, with the diffraction pattern showing mainly randomly oriented small Cu crystallites. Above temperatures of  $140^\circ\text{C}$ , larger Cu crystals formed. The tip morphology is shown in Fig. 43.

Crystallization is found not only for metals but also for carbon. When freestanding  $a$ -C rods are annealed in the presence of iron nanoparticles, the  $a$ -C can be converted into graphite.<sup>77,156,157</sup> An example is shown in the TEM micrographs in Fig. 44. At a temperature of  $650^\circ\text{C}$ , iron particles migrated into the nanorod and graphitized the carbon as they did so.

Finally, when nanoscale deposits are annealed, annealing can entirely destroy the structure. While this did not occur for the Fe deposit described above, it clearly occurred for a pattern consisting of Pt-containing dots. The dots were a few nanometers in size and when heated to a temperature of  $800^\circ\text{C}$ , it was found that the pattern completely deformed.<sup>158</sup>

*b. Conductivity.* For carbon structures that are graphitized during annealing, the conductivity clearly increases. Already in 1934, Steward<sup>1</sup> studied films deposited from contamination. When testing the conductivity with a telephone receiver, he found that the initially isolating film had become conducting after heating the platinum substrate “bright red *in vacuo*.” The amorphous carbon had most likely turned into

graphite. Similar results were found for graphitized nanorods, for which the resistivity decreased from  $68.9$  to  $5.2 \times 10^{-4} \Omega \text{ cm}$ .<sup>77</sup>

Positive results have also been found for metal-containing deposits. Deposits from  $\text{WF}_6$  showed an improvement of a factor of 10 when annealed at  $500^\circ\text{C}$  in a  $\text{H}_2$  atmosphere.<sup>159</sup> An improvement in conductivity of as much as three orders of magnitude was observed for deposits that were created with a low beam current. This is probably because in those particular deposits, the dissociation of the precursor molecules was less complete and relatively more precursor fragments desorbed. See also Fig. 45. Annealing was also beneficial for the conductivity of deposits from  $\text{CpPtMe}_3$ . For wires, annealing for 2 h at  $180^\circ\text{C}$  led to a drop by a factor of 3 in the resistance.<sup>89</sup> For tips used as emitters, the field emission current and the reliability of the emitters increased when annealing between  $400$  and  $750^\circ\text{C}$ .<sup>160</sup>

Annealing does not always improve the conductivity. For instance, annealing at  $170^\circ\text{C}$  for 10 min had no effect on wires deposited from  $\text{Fe}_3(\text{CO})_{12}$ .<sup>91</sup> The temperature may not have been high enough since annealing at  $600^\circ\text{C}$  did give an effect for similar Fe-containing deposits.<sup>151-153</sup> However, even at high temperatures, annealing does not necessarily lead to improved conductivity. Annealing of lines deposited from  $\text{Me}_2\text{-Au-tfac}$  or  $\text{Co}_2(\text{CO})_8$  at temperatures around  $300^\circ\text{C}$  gave dewetting instead of wetting: the lines separated into solidified droplets.<sup>104,121,161</sup> Apparently, the *a*-C matrix had oxidized and disappeared, leaving the (oxidized) metal grains.

### C. Conclusions

It is consistently reported that a higher substrate temperature during deposition leads to lower vertical growth rates. This is caused by shorter residence times of adsorbed precursor molecules. The lateral growth rate is only affected if the temperature leads to a change in the growth regime. If

the substrate temperature is in the order of the precursor thermal decomposition temperature, dissociation can be thermally induced parallel to being electron induced. This has been observed for a number of metal-organic precursors. The result is a higher metal content and a higher conductivity.

Experiments where the substrate is tilted during deposition indicate that there is a correlation between the deposition yield and the SE yield.

Postdeposition irradiation induces graphitization of *a*-C deposits, it can induce heating (thereby changing the deposit morphology from smooth to rough), the deposit conductivity can increase, and deposits can be sculpted.

Postdeposition annealing can graphitize *a*-C deposits and can improve the metal content for metal-containing deposits. Having said this, carbon appears to be an element that is difficult to remove by annealing. In most reported cases, carbon was generally still present in the deposit after annealing, often in the form of carbides. The formation of a carbide is unfavorable because it is a thermodynamically very stable compound. Another issue is the diffusion of substrate material into the deposit (observed for C, Si, and Fe) and the deformation of the structure. The conductivity generally improves provided the deposit stays intact and dewetting does not occur.

### VII. SUBSTRATE

Important for the understanding of the physics of the deposition process is whether the substrate is of any influence. An influence can either be expected for substrate-precursor interactions (e.g., adsorption) or for electron-substrate interactions (e.g., SE yields). The first type of interaction was suggested to explain experiments where thin films (tens of angstrom thick at most) were deposited from  $\text{WF}_6$ . It was found that the growth rate on Si is higher than on Au (at the same pressure).<sup>162</sup> According to the authors, the difference in growth rate is the result of a smaller adsorption

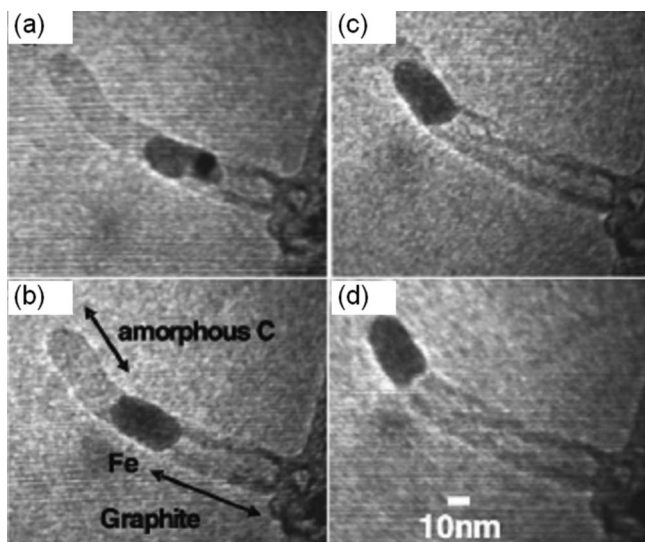


FIG. 44. Graphitization of carbon nanowire by an iron particle. The annealing temperature was  $650^\circ\text{C}$ . From Ref. 156. Copyright © 2004 by the American Physical Society. Reprinted with permission by the American Physical Society.

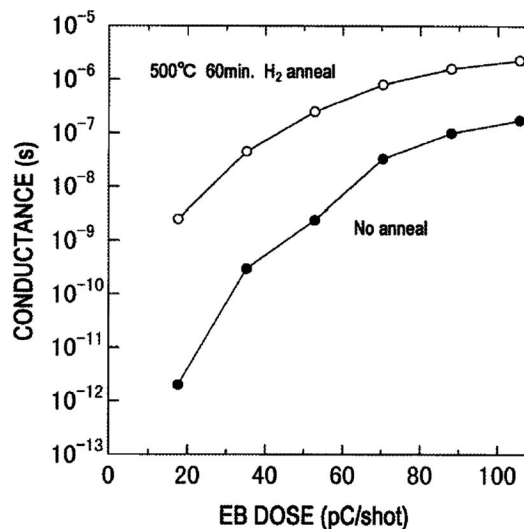


FIG. 45. The effect of annealing of wires deposited from  $\text{WF}_6$ . For wires deposited with a low beam current, the annealing has a stronger effect, up to as much as three orders of magnitude. From Ref. 159. Copyright © 1998 by IOP Publishing Ltd. Reprinted with permission by IOP Publishing Ltd.

coefficient of  $\text{WF}_6$  on Au than on Si. This seems likely since the SE yield is in general larger for Au than for Si.<sup>163</sup>

However, in most other studies, deposits are thicker and the relevant surface is the deposit surface, not the substrate surface. Therefore, in most cases, the electron-substrate interactions are dominant instead of the substrate-precursor interactions. The former become visible as differences in BSE and SE yields and in the spatial extent of the electron scattering in the substrate. Indications of the influence of BSE and SE yields come from experiments and simulations on, again, deposition on Au and Si. A Si sample was partially coated with a 500 nm layer of Au and deposition was performed over the edge of the Au layer with hfac-Cu-VTMS. The vertical growth rate was a factor of about 1.5 larger on the Au than on the Si.<sup>86</sup> This ratio compared well to calculated BSE yields for the two situations. Unfortunately, the deposition yields for a carbon precursor (acrylic acid) on the same substrate agree less well with the simulated BSE and SE yields. The author tentatively suggested a slightly different dissociation process (radical or ion assisted) but still assumed that the model is correct.

As far as the vertical growth rate is concerned, one would expect that the influence of the substrate is negligible when depositing tips. For most of the time, the interactions take place in the tip and not in the underlying substrate. This theory is confirmed by experiments where tips were deposited on Al, Ti, Cu, W, Mo, and Pb. There was no significant effect of the substrate on the vertical growth rate, composition, or morphology.<sup>86</sup> Contradicting results were found for the deposition of self-standing contamination rods. Different growth rates were observed for various substrates (among others Al, Ti, Cu, and W).<sup>164</sup> However, since the residual gas was used as precursor and cleaning procedures of the substrates were not described, the concentration of residual gas molecules on the samples may not have been constant. Furthermore, one would expect substrate effects to be very small because the majority of the relevant interactions occur on the growing self-standing rod, nearly completely away from the substrate.

Clearer examples of the influence of the substrate-electron interactions come from experiments where the deposit width is studied. For instance, when depositing contamination lines on GaAs and Si, significant shoulders on the lines were observed.<sup>114</sup> The width of the shoulders appears to be dependent on the substrate. Region 1 in Fig. 46(a) is the area where the PEs impinge on the GaAs substrate and region 2 indicates the range over which BSEs and SEs “interact with the substrate surface.” They calculated the spatial extent of BSE scattering in the substrate for GaAs and Si and indicated this with the dashed lines in Figs. 46(a) and 46(b), respectively. The calculated range is larger in Si than in GaAs, which is the result of the smaller density of Si. This coincides “fairly well” with the extent of region 2 for both samples. Furthermore, the measured height in region 2 is also less for Si than for GaAs, which is “consistent with the energy of the e-beam being scattered over a larger volume in the Si.” This is a similar effect to the BSE proximity effect described in Sec. IVE1 [see also Fig. 33(b)]. A similar dependency on the spatial distribution of electron scattering in

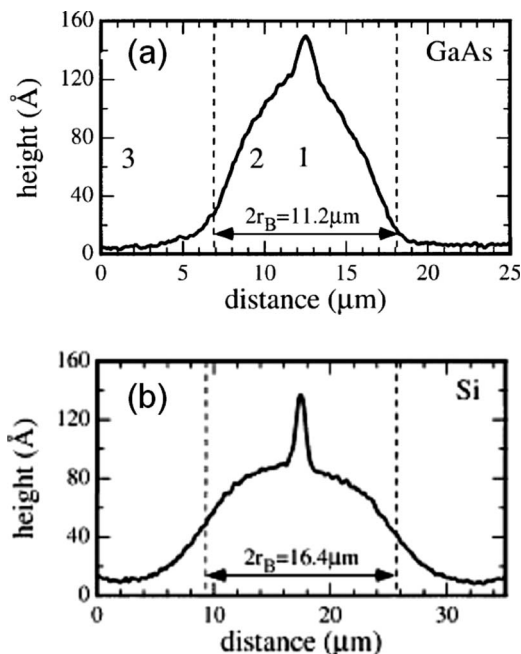


FIG. 46. Height profiles for line depositions on (a) GaAs and (b) Si. From Ref. 114.

the substrate was found for the diameter of tips. The diameter of tips deposited from  $\text{CpPtMe}_3$  on Si, Cu, and  $\text{SiO}_x$  substrates were 199, 146, and 49 nm, respectively, at identical accumulated charges.<sup>70</sup> These diameters “correspond with the main path length of those materials and the related proximity function.”

Regarding the influence of the thickness of the substrate, there seems to be no effect on the width of deposits. Dots were deposited from  $\text{W}(\text{CO})_6$  on areas that were transparent (thin) and nontransparent (thick) to 200 keV electrons of a Si(110) sample. The width of the dots was not significantly influenced by substrate thickness.<sup>165</sup> This was confirmed by Monte Carlo simulations.<sup>48,166</sup>

Apart from adsorption behavior or the spatial extent of electron scattering, the conductivity of the substrate is also found to be of influence on the deposition process. An example of this, the deformation proximity effect, was already discussed in Sec. VE 1. Depending on the conductivity of the substrate, already deposited structures were found to deform when new structures were grown in the neighborhood [see Figs. 38(b) and 38(c)]. Another example is the growth of dendritic structures on insulating substrates such as  $\text{Al}_2\text{O}_3$ ,<sup>167–170</sup> BN,<sup>171</sup> and tetragonal zirconia crystals.<sup>172</sup> The dimensions of the structures can vary by orders of magnitude [see Figs. 47(a) and 47(b)] and the formation was observed for metal-organic precursors [e.g.,  $\text{W}(\text{CO})_6$ ] and contamination. It is assumed that the dendritic growth is caused by charging of the sample. As a result of the charging, a local electric field is formed, which concentrates at convex areas. If the electric field is strong enough (estimated field strengths in the order of  $10^6$ – $10^7$  V m<sup>-1</sup>) precursor molecules in the gas phase are polarized and/or ionized and will follow deterministic instead of ballistic trajectories.<sup>171</sup> Similar growth was also observed for  $\text{W}(\text{CO})_6$  on 10 nm thick  $\text{Si}_3\text{N}_4$  membranes.<sup>173</sup> Arrays of dots were deposited in the STEM

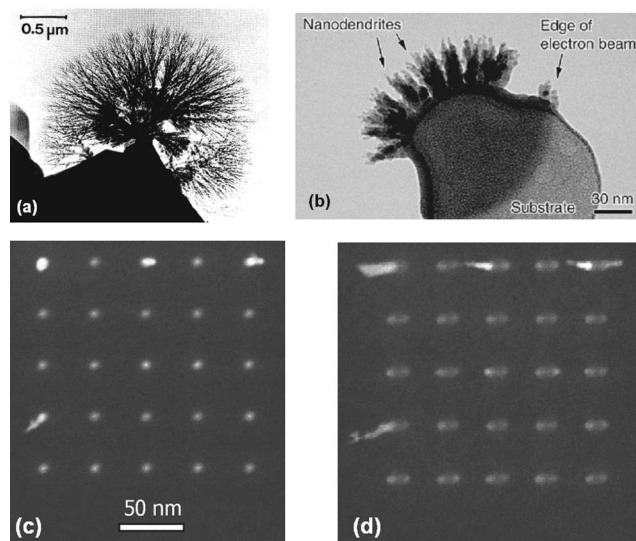


FIG. 47. Examples of the effect of an insulating substrate. (a) Dendritic growth from hydrocarbons on a BN crystal as result of broad beam illumination. From Ref. 171. Copyright © 1995 by the American Physical Society. Reprinted with permission by the American Physical Society. (b) Dendritic growth from  $W(CO)_6$  on  $Al_2O_3$  as a result of broad beam illumination. From Ref. 168. (c) An array of dots deposited from  $W(CO)_6$  on  $Si_3N_4$ . From Ref. 173. Copyright © 2007 by IOP Publishing Ltd. Reprinted with permission from IOP Publishing Ltd. (d) Same array as in (c) but now viewed under a tilt angle of  $20^\circ$ . The outliers are clearly higher than the average deposit and also show branching. From Ref. 173. Copyright © 2007 by IOP Publishing Ltd. Reprinted with permission from IOP Publishing Ltd.

[Fig. 47(c)]. When the sample was tilted, it became apparent that some of the dots were considerably higher than the average dots [Fig. 47(d)]. These outliers also showed branching in some cases. This, and the fact that the irregular growth was not observed close to conducting areas on the substrate, is a strong indication that charging played a significant role.

In conclusion, the substrate can affect the vertical growth rate. This can be due to changes in the adsorption behavior (for deposits several angstrom thick) and/or changes in the BSE and SE yields. The width of the deposits is found to be dependent on the spatial extent of the electron scattering in the substrate. The thickness of the substrate does not seem to affect the width of deposits. On insulating substrates, dendritic and irregular growth was observed, behavior that is most likely due to charging effects.

## VIII. PRECURSOR

### A. Introduction

The precursor molecules contain the material to be deposited and as such, it is a crucial factor in the deposition process. Many different precursors have been tried for EBID. Figure 48 shows that carbon precursors (residual gas, contamination in the electron optical system, or carbon precursors) are most widely studied.  $W(CO)_6$ ,  $Fe(CO)_5$ , and  $Me_3PtCp$  are the most popular metal-organic precursors and  $WF_6$  is the most frequently used inorganic precursor. Silvis-Cividjian and Hagen<sup>41</sup> presented a fairly complete list of the precursors used, together with references.

According to Hoffmann,<sup>174</sup> a suitable and useful precursor has a number of requirements: it needs to be a volatile compound at room temperature (either a gas, liquid, or

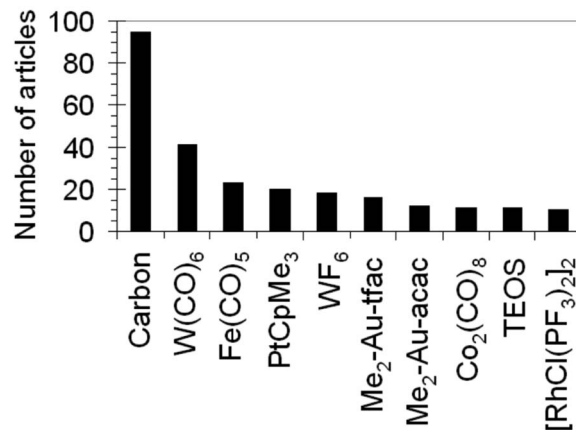


FIG. 48. Histogram of the number of articles that report on work on specific precursors. The ten most popular precursors are shown.

solid), it needs to decompose to the desired “product” in a fast, clean, and highly selective way (ideally without additional reactant gas), vacuum contamination (corrosion) should not occur, it needs to evaporate completely, fast, and without residue, it needs to be stable during storage and supply, and it is preferably nontoxic and not expensive. On top of these requirements, we have to keep in mind that deposition experiments usually take place in high vacuum conditions and not in ultrahigh vacuum conditions. This means that there is a background pressure of water or air in the order of  $10^{-6}$  mbar. Still we want to have pure deposits.

At the moment, none of the precursors used for EBID reach the desired level of performance. Frequently used stable compounds such as  $W(CO)_6$  or  $PtCpMe_3$  yield deposits that contain typically about 10% metal.  $WF_6$ , a stable compound that yields a higher concentration of metal (80%–100%), is an aggressive precursor that can damage electron optical equipment.<sup>175</sup>  $AuCl(PF_3)_3$  or  $D_2GaN_3$ , precursors that are known to yield pure deposits and are not aggressive, are very unstable and can be difficult or even dangerous to work with.<sup>176</sup> Moreover, a precursor such as  $AuCl_3$  does, in certain conditions, not yield any Au at all.<sup>177</sup> It can be safely stated that currently the main factor limiting the application of beam induced deposition in devices is the lack of control over the composition of the deposits. Despite the importance of a good understanding of the dissociation mechanism for the progress in FEBIP research, the subject receives a relatively small amount attention compared to the other parameters described in this review. Improvement is mainly tried through tweaking of the beam parameters (beam current, acceleration voltage) or postprocessing. The choice of precursor is mostly determined by the fact whether it is used often and whether it is readily available. Nearly all of the precursors used for deposition stem from the CVD world and there has been hardly any search for precursors dedicated to FEBIP.

### B. Precursor gas only

In order to make a start with the understanding of the dissociation mechanisms of precursors, systematic studies are required. There are a few such studies.

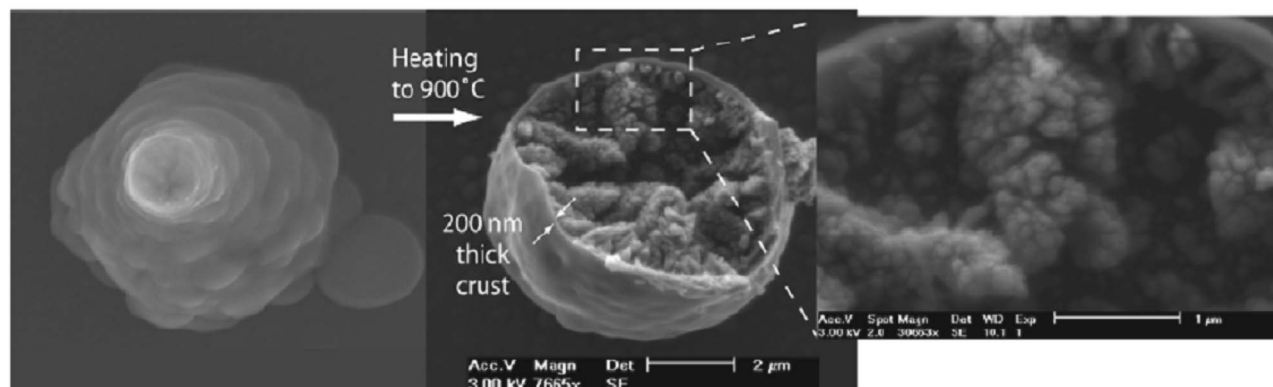


FIG. 49. Hollow pear shaped deposits from formic acid. From Ref. 86. Reprinted with permission from author.

A study was made of the composition of deposits from purely organic precursors (styrene, acrylic acid, propionic acid, acetic acid, and formic acid) and precursors containing fluorine, nitrogen, and chlorine (trifluoroacetic acid, acetonitrile, and  $\text{CCl}_4$ ). Analysis techniques used were energy dispersive x-ray (EDX), micro elastic recoil detection analysis ( $\mu\text{ERDA}$ ), micro Fourier transform infrared spectroscopy ( $\mu\text{FTIR}$ ), and micro-Raman. Surprisingly, the EDX,  $\mu\text{ERDA}$ , and  $\mu\text{FTIR}$  measurements show that the deposits from the purely organic precursors are all chemically very similar.<sup>86,178</sup> The composition is  $\text{C}_9\text{H}_2\text{O}$  (regardless of the stoichiometric composition of the precursor) and 90%–95% of the carbon is  $sp^2$  bonded (C–C) and 5%–10% is  $sp^3$  bonded (C–H). The micro-Raman measurements indicate that the carbon deposits consist of nanocrystalline graphite with cluster sizes around 2 nm. Similar results are found for the precursors containing the components F, N, and Cl. It was found that 90% of these specific components are lost during the deposition, either during precursor fixation or by continued irradiation of already deposited material during the deposition process. Analysis of deposits from two paraffins ( $\text{C}_{22}\text{H}_{46}$  and  $\text{C}_{24}\text{H}_{50}$ ) with EELS and Raman confirm these results.<sup>16</sup> Again, 80%–90% of the carbon atoms were  $sp^2$  bonded and Raman studies showed a similar amount of disorder in the carbon.

Regarding the growth rate and the growth behavior, significant differences were found between acrylic acid and styrene. With a similar precursor flux reaching the irradiated area, acrylic acid has a five times higher growth rate than styrene.<sup>178</sup> This is most likely due to the longer residence times of the acrylic acid molecules on the adsorption sites, which means that its sticking coefficient is higher. This is caused by the fact that acrylic acid is a polar molecule and can form H bonds, interactions that are much stronger than the van der Waals forces for styrene.

Another difference is the deposit smoothness. While most of the precursors yield a smooth deposit, the deposits from formic acid are sometimes (and not reproducibly) rough and have a hollow structure<sup>178</sup> (see Fig. 49). Apparently, electron induced desorption of volatile elements occurs inside the deposits after precursor fixation because these volatile elements are present in the precursor in a high ratio compared to the carbon [ $\text{C}/(\text{O}+\text{H})=\frac{1}{4}$ ].

In another comparative study, the composition of deposits from four Cu precursors was determined:  $\text{Cu}(\text{hfac})_2$ , hexafluoro-acetylacetonate copper dimethyl-1-hexen-3-yne ( $\text{hfac-Cu-MHY}$ ),  $\text{hfac-Cu-VTMS}$ , and hexafluoro-acetylacetonate copper dimethyl-butene ( $\text{hfac-Cu-DMB}$ ). For  $\text{Cu}(\text{hfac})_2$  and  $\text{hfac-Cu-MHY}$  stable compositions of 13%–14% Cu and 75%–80% C were found during sputtering cycles.<sup>125</sup> The Cu content for  $\text{hfac-Cu-VTMS}$  and  $\text{hfac-Cu-DMB}$  was estimated to be 15%–20% and 60%–70% C. The fluorine signal was not above the noise level. The authors concluded that the Cu content is not determined by the stoichiometric composition of the precursors but more by the thermodynamic precursor stability and the electron/precursor flux ratio. These results are mostly consistent with experiments where the composition of physisorbed multilayers and deposits from  $\text{hfac-Cu-VTMS}$  was studied. It was found that the electron bombardment mostly affects the fluorine- and oxygen-containing groups in the  $\text{hfac}$  ligands, while the  $\text{CH}_x$  groups from the VTMS and  $\text{hfac}$  ligands remain mostly unaffected.<sup>52</sup>

Two Rh precursors,  $(\text{RhCl}(\text{PF}_3)_2)_2$  and  $(\text{RhCl}(\text{CO})_2)_2$ , appear to have decomposition paths very similar to each other.<sup>108</sup> The composition for both precursors was independent on the accumulated charge, which indicates that the deposit is chemically quite stable. The Rh content was 60% and 56%, respectively, and the Cl content was 7% and 5%, respectively. The elements that are at the core of the precursor molecules are present in relatively high concentrations (19% P for the carbon-free precursor, 34% C for the carbon-containing precursor) and fluorine was not detected in either of the deposits. These experimental results are in contradiction with a theoretical model made for  $(\text{RhCl}(\text{PF}_3)_2)_2$ . Calculations based on density functional theory on the lowest energy pathways for decomposition indicate that the loss of the  $\text{PF}_3$  ligands is most favorable.<sup>179</sup> However, the e-beam induced deposits contain P and no F. Similar results were obtained for  $\text{Pt}(\text{PF}_3)_4$ . It was found that electrons mainly induce scissions of the P–F bond and not the removal of complete PF ligands as in the case for thermal decomposition in CVD. The discrepancy between results from EBID on the one hand and results from calculations and CVD on the other suggests that the electron induced dissociation is more complex than just a simple single-step process.

Few differences were observed between deposits from three Au precursors: Me<sub>2</sub>-Au-acac, Me<sub>2</sub>-Au-tfac, and Me<sub>2</sub>-Au-hfac. For all precursors, the deposit composition is 10% Au, 20% O, and 70% C for beam currents >900 pA.<sup>29</sup> Again, fluorine is not detected. This indicates that the decomposition mechanism is similar.

For the cases described above, the dissociation was electron induced. In some of the preceding sections, it has become clear that the contribution of thermal decomposition to the growth can be significant. In general, this is beneficial for the purity of the deposits, but in some cases the size and/or precise location of the deposit is more difficult to control. This was, for instance, observed when creating deposits with a large accumulated charge (Co<sub>2</sub>CO<sub>8</sub>) (Ref. 87) with high beam currents [Me<sub>2</sub>-Au-acac, Me<sub>2</sub>-Au-tfac, Me<sub>2</sub>-Au-hfac, Cu(hfac)<sub>2</sub>, Mo(CO)<sub>6</sub>, Me<sub>3</sub>PtCp, Co<sub>2</sub>CO<sub>8</sub>,<sup>87</sup> Co(CO<sub>3</sub>)NO,<sup>8</sup> hfac-Cu-VTMS (Ref. 86)] or in situations where the thermal conductivity of the deposit was low (hfac-Cu-VTMS).<sup>115</sup> Indications of autocatalytic effects were found for Fe(CO)<sub>5</sub>.<sup>138</sup> These thermal effects are clearly precursor dependent. As an example, no thermal effects have been observed for (RhCl(PF<sub>3</sub>)<sub>2</sub>)<sub>2</sub>, even though different scan patterns and deposition conditions have been tried.<sup>179</sup>

Despite the indications that thermal effects are involved, it is not so easy to link the above-mentioned effects to the thermal decomposition temperature. The precursors Co<sub>2</sub>(CO)<sub>8</sub> and hfac-Cu-VTMS showed thermally enhanced decomposition and have a low thermal decomposition temperature: 60 (Ref. 141) and 63 °C,<sup>125</sup> respectively. Fe(CO)<sub>5</sub> has demonstrated steady-state thermal decomposition even at -20 °C.<sup>139</sup> For these precursors, thermally assisted decomposition has been observed during deposition. As mentioned, thermally assisted decomposition was not observed for (RhCl(PF<sub>3</sub>)<sub>2</sub>)<sub>2</sub>, which also has a much higher thermal decomposition temperature (160 °C).<sup>180</sup> So far the trend is consistent, but this trend is contradicted by the thermal decomposition temperature of Co(CO<sub>3</sub>)NO and Me<sub>2</sub>-Au-hfac: 162 (Ref. 181) and 160 °C,<sup>182</sup> respectively.

Further evidence of the complexity of the dissociation process comes from studies on the proximity effects and the deposition on insulators. From the discussion of the various proximity effects in Sec. V E 2 it became apparent that the composition of parasitic deposits can be very different from the primary deposits. The composition of dendritic structures created on insulating substrates (discussed in Sec. VII) can also be very different from the usual, nondendritic deposits. For instance, deposits created from W(CO)<sub>6</sub> are usually nanocomposites,<sup>128</sup> with small W crystals in an *a*-C matrix. However, the dendritic structures obtained on insulating surfaces were pure bcc tungsten crystals.<sup>167</sup> In contrast, dendritic structures created on insulators from the Pt precursor were not pure Pt but nanocomposites.<sup>169</sup>

Such contradictions, together with the observations that (1) in some cases the stoichiometric composition of a precursor seems to be irrelevant for the deposit composition (for the mentioned C, Cu, and Au precursors) and (2) that electron induced dissociation does not necessarily follow either the theoretically calculated lowest energy pathway or the thermal decomposition path, show that the dissociation

mechanism is not as simple as one may initially expect. The results also show that further detailed studies into the precursor chemistry and dissociation mechanisms are required to be able to improve the deposit composition.

### C. Reactive gases

Although the precursor chemistry is complex enough when the precursor gas is the only gas, as became clear in Sec. VIII B, it is possible to influence the decomposition mechanism by mixing in additional gases, so-called reactive gases. The idea is that the reactive gas forms volatile components with unwanted fragments that otherwise remain on the sample after the dissociation of the precursor molecules. This prevents these fragments from polluting the deposit. Strictly speaking, nearly all experiments described in this review are done in the presence of a reactive gas. After all, the typical FEBIP system has a background vacuum of no better than 10<sup>-6</sup> or 10<sup>-7</sup> mbar, which is mostly due to the presence of water and air. Depending on the cleanliness of the system, carbon contamination will also be present. Therefore, during a typical FEBIP experiment, precursor molecules will be competing with, for instance, water molecules for surface adsorption sites and there will always be oxidizing components available to react with dissociation fragments.

However, there are a number of reports where the pressure of reactive gases was raised significantly above the background level. In a relatively simple example of precursor chemistry, the effect of mixing H<sub>2</sub> with WCl<sub>6</sub> during deposition was tested.<sup>142</sup> This made the W content increase from 95% to 100%, probably by the formation of HCl. Using a more complicated combination, Folch *et al.*<sup>183</sup> mixed 130 mTorr of Me<sub>2</sub>-Au-hfac with 3 Torr of H<sub>2</sub>O and with a mixture of 2 Torr of O<sub>2</sub> and 8 Torr of Ar. While the Au content of squares deposited without reactive gas was 2%–3% at most, this increased to 20% when H<sub>2</sub>O was added and increased to about 50% when the Ar/O<sub>2</sub> mixture was added. According to the authors, H<sub>2</sub>O or O<sub>2</sub> are ionized by the e-beam, react with the C from the deposits, and form CO<sub>2</sub> or CO. This would explain that the Ar/O<sub>2</sub> mixture has more effect than the H<sub>2</sub>O because there is more O present. Mølhave *et al.*<sup>15</sup> performed a similar experiment. They used a similar precursor (Me<sub>2</sub>-Au-acac, partial pressure not reported), mixed in 0.4–0.9 Torr H<sub>2</sub>O, and instead of depositing squares, they deposited tips and wires (see Fig. 50). The results are quite different. The Au content increased but not homogeneously distributed over the deposits. The gold was concentrated mostly in the core of the tips and wires, surrounded by a shell of amorphous carbonaceous material. This particular core-shell structure could only be fabricated in the presence of water; mixtures of H<sub>2</sub> and O<sub>2</sub> with the same amount of H and O as 0.8 Torr of H<sub>2</sub>O did not have such an effect. That the effect of H<sub>2</sub>O on the deposit composition is far from consistent becomes evident from experiments by Tseng.<sup>184</sup> Me<sub>3</sub>PtCp was mixed with H<sub>2</sub>O and no influence was found on the deposit composition.

Wang *et al.*<sup>62</sup> introduced O<sub>2</sub> during deposition from Pt(PF<sub>3</sub>)<sub>4</sub>, but the Pt content increased only by a small

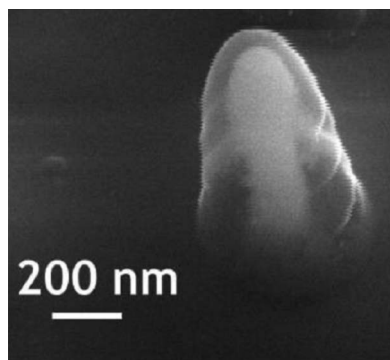


FIG. 50. Core-shell structure for a tip deposited from  $\text{Me}_2\text{-Au-acac}$  in the presence of  $\text{H}_2\text{O}$ . From Ref. 15. Copyright © 2003 by the American Chemical Society. Reprinted with permission by the American Chemical Society.

amount, from around 17% to around 22%. Better results were obtained by Fischer *et al.*,<sup>105</sup> who added oxygen during the deposition of  $\text{SiO}_2$  (precursor not mentioned) and were able to create carbon-free deposits.

#### D. Precursor pressure

It is consistently reported that higher gas pressures lead to higher growth rates.<sup>25,60,143,185</sup> In Fig. 51, the growth rate is plotted as a function of the current density for three different  $\text{Ru}_3(\text{CO})_{12}$  fluxes: (1)  $3 \text{ cm}^{-2} \text{ s}^{-1}$ , (2)  $1.5 \text{ cm}^{-2} \text{ s}^{-1}$ , and (3)  $0.9 \text{ cm}^{-2} \text{ s}^{-1}$ . As the precursor flux increases, so does the growth rate. In the initial stages, the growth is e.l. In the final stages, the growth is p.l.

A simulation has been developed to determine the local distribution of precursor molecules on the substrate for the supply from a gas nozzle typically used in FEBIP experiments. In the Monte Carlo simulation, molecular flow conditions are assumed. The distribution from the model is compared to the height distribution of impinging precursor molecules that are thermally dissociated on a heated substrate. A good quantitative agreement is found [see Fig. 51(b)].<sup>186</sup>

Some reports mention the existence of a minimum gas pressure required for deposition. A pressure threshold of  $8.6 \times 10^{-4} \text{ Pa}$  was found for deposition from  $\text{CrO}_2\text{Cl}_2$ .<sup>98</sup> Below this pressure, no Cr deposition was observed. It was found that etching of the (Cl-deficient)  $\text{CrO}_x\text{Cl}_y$  film occurred during postdeposition irradiation in the presence of  $\text{Cl}_2$ . The authors suggested that there are two competing processes during growth from  $\text{CrO}_2\text{Cl}_2$ : dissociation of  $\text{CrO}_2\text{Cl}_2$  and recombination of  $\text{CrO}_x\text{Cl}_y$  with Cl. How the presence of these two competing processes would lead to the observed pressure threshold does not become quite clear. Pressure thresholds were also found for  $\text{W}(\text{CO})_6$  ( $1 \times 10^{-6} \text{ Pa}$ ) and  $\text{Me}_2\text{-Au-acac}$  ( $5 \times 10^{-7} \text{ Pa}$ ).<sup>80</sup> Growth was not observed below these thresholds regardless of the beam current. The authors suggested that a requirement for deposit growth is the presence of stable nuclei on the substrate. Below the mentioned precursor pressures, “the nuclei will not grow.” This would indicate a nonlinearity of a type that has not yet been reported elsewhere. Another explanation for the pressure threshold could be again two competing processes: this time

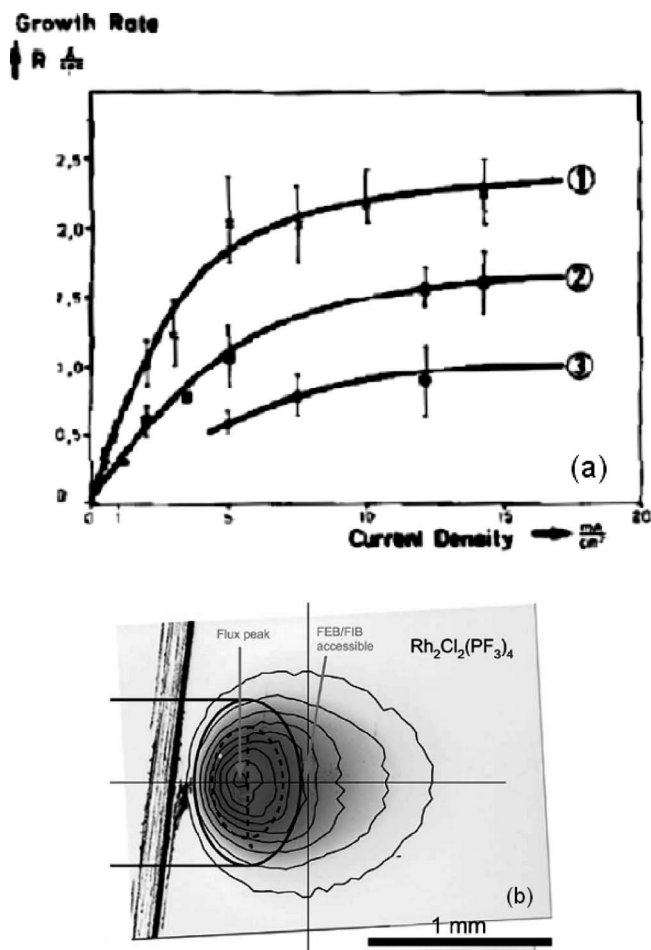


FIG. 51. (a) Growth rate as a function of the current density for three different  $\text{Ru}_3(\text{CO})_{12}$  fluxes. Precursor flux: (1)  $3 \text{ cm}^{-2} \text{ s}^{-1}$ , (2)  $1.5 \text{ cm}^{-2} \text{ s}^{-1}$ , and (3)  $0.9 \text{ cm}^{-2} \text{ s}^{-1}$ . From Ref. 60. Copyright © 1986 by Elsevier. Reprinted with permission by Elsevier. (b) Comparison of the impinging precursor distribution between experiment (gray scale height map) and simulation (isodensity contours). From Ref. 186. Copyright © 2006 by Elsevier. Reprinted with permission by Elsevier.

dissociation of precursor molecules and knock-on damage by the PEs. The PE energy was 200 keV and sputtering of the deposit nuclei by the PEs is conceivable.<sup>49</sup>

Morphological changes were observed for deposits from  $\text{Ni}(\text{C}_5\text{H}_5)_2$  as a function of the gas pressure (in the range of  $10^{-6}$ – $10^{-8}$  mbar) and substrate temperature (in the range of  $-103$  to  $-25$  °C). Depending on the precise conditions, uniform [Figs. 52(a) and 52(b)] or open structures [Figs. 52(c) and 52(d)] were found.<sup>76</sup> It appeared that the formation of uniform or open structures was determined by the ratio between the precursor partial pressure  $P_{\text{partial}}$  and the precursor equilibrium pressure  $P_{\text{equilibrium}}$  at the corresponding substrate temperature. Uniform deposits were formed for ratios  $P_{\text{partial}}/P_{\text{equilibrium}} < 1$  and open deposits were formed for  $P_{\text{partial}}/P_{\text{equilibrium}} > 1$ . How these conditions lead to the observed morphologies was not explained.

#### E. Conclusions

From the few systematic studies that have been performed, it becomes clear that electron induced decomposition is a complex process. It is consistently reported that the deposit composition is not directly dependent on the stoichi-

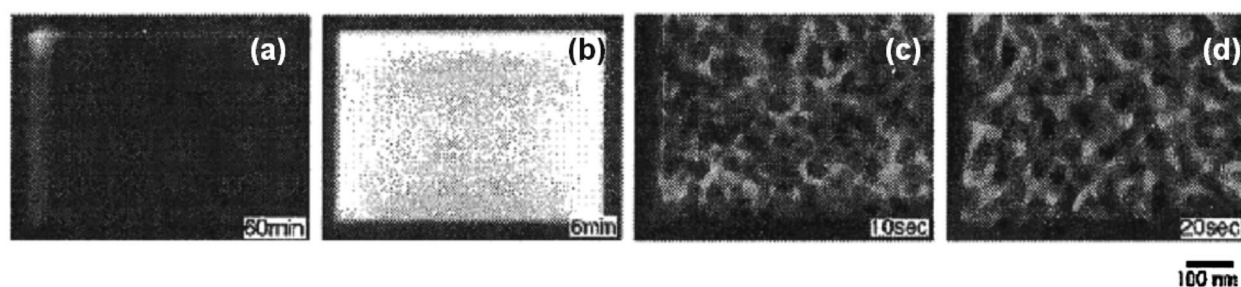


FIG. 52. The morphology of deposits from  $\text{Ni}(\text{C}_5\text{H}_5)_2$  was found to depend on the ratio between  $P_{\text{partial}}/P_{\text{equilibrium}}$ . The ratios  $P_{\text{partial}}/P_{\text{equilibrium}}$  are (a)  $1.7 \times 10^{-4}$ , (b)  $6.5 \times 10^{-4}$ , (c)  $1.8 \times 10^1$ , and (d)  $9.6 \times 10^2$ . From Ref. 76. Copyright © 2001 by World Scientific. Reprinted with permission by World Scientific.

ometric composition of the precursor. For five purely organic precursors, the composition is constantly  $\text{C}_9\text{H}_2\text{O}$ . Most of the carbon is  $sp^2$  bonded and a small fraction is  $sp^3$  bonded. For four Cu precursors, the Cu content is 10%–20% and a similar metal content is found for three gold precursors. Two Rh precursors, one having  $\text{PF}_3$  ligands and the other  $\text{CO}_2$  ligands, show similar decomposition paths. The elements at the core of the precursors (P and C, respectively) are present in relatively high concentrations. For all precursors, it is consistently reported that elements such as F, N, and Cl are removed almost completely from the deposit. Further evidence of the complexity of the dissociation process comes from studies on the proximity effects and the deposition on insulators. The composition of parasitic deposits and dendritic deposits can be very different from the primary deposits.

For the Cu precursors, it is concluded that the thermodynamic stability of the precursor and the electron/precursor flux ratio, rather than the stoichiometric composition, determine the final composition. For other precursors, this link is not so easy to see. For instance, the electron induced decomposition paths of the Rh precursors are very different from decomposition paths expected from calculations or thermal decomposition.

The influence of reactive gases is far from consistent. Adding  $\text{H}_2\text{O}$  to  $\text{Me}_3\text{PtCp}$  did not influence the deposit composition. Adding  $\text{H}_2$  to  $\text{WCl}_6$  or  $\text{O}_2$  to  $\text{Pt}(\text{PF}_3)_4$  gave only a minor increase in metal content. The only cases where a significant effect was reported were for  $\text{Me}_2\text{-Au-hfac}$  mixed with  $\text{O}_2$  and  $\text{Me}_2\text{-Au-acac}$  mixed with  $\text{H}_2\text{O}$ . The former gave an increase in Au content from a few to 20%; the latter resulted in a Au core surrounded by an  $a\text{-C}$  shell.

A model has been developed to determine the distribution of gas molecules on a substrate for a nozzle geometry and results are consistent with experimental results. Higher precursor pressures lead to higher growth rates and in some cases a pressure threshold for beam induced growth is reported.

## IX. CONCLUSIONS

In this review, the consistency of experimental results with each other and with existing models has been discussed. Most of the observed effects can be explained with available models. The lateral growth of deposits as a function of the accumulated charge is characterized by a rapid increase followed by saturation. Deposits as small as 1.0 nm can be

obtained by stopping the growth in the stage of rapid increase. At these small scales, the counting statistics of precursor molecules become visible as variations in the mass of the deposits. The vertical growth rate depends on the growth regime. In the e.l. regime, the deposit height is proportional to the current density. In the p.l. regime, the deposit height depends on the gas flux. The substrate mainly affects the deposit dimensions by the BSE and SE yields and the spatial extent of the electron scattering in the bulk.

E-beam induced heating can play a significant role during deposition. Whether heating occurs depends on the current density, the PE energy, the thermal conductivity of the deposit, and the extent to which the electron scattering is confined to the deposit. The temperature rise as a result of beam induced heating in specific cases is estimated to be about 50 °C. Apart from reducing the vertical growth rate, heating can induce a change from e.l. to p.l. growth. Additionally, it can lead to a change in the dissociation mechanism (see below). Similar effects are observed in experiments where the sample is heated during deposition. If the temperature reached during an experiment is in the order of the precursor thermal decomposition temperature, dissociation can be thermally induced parallel to being electron induced. This has been observed for a number of metal-organic precursors. The result is a deposit with a (relatively) high purity, high density, and high conductivity. This is the reason why high current densities are beneficial for the deposit properties; (1) a higher degree of electron induced fragmentation is obtained and (2) heating occurs. The lateral growth rate is only affected if the temperature leads to a change in growth regime.

Studies on the influence of the PE energy on the vertical growth, composition, morphology, and conductivity gave contradictory results. These contradictions could be explained largely with a combination of the growth model and e-beam induced heating, but this approach leaves some results unexplained. The scan pattern and scan strategy will mainly influence the deposit properties or the growth rate in the case that a change from the e.l. to the p.l. regime (or vice versa) is induced. For instance, short dwell times and long loop times are beneficial in obtaining a high growth rate. On the other hand, long dwell times and short loop times are beneficial in obtaining a high-conductivity deposit. Post-deposition irradiation induces growth of metal crystals in metal-containing deposits and increases the conductivity.

TABLE III. Checklist that would ideally be included in every article reporting on EBID experiments.

Growth conditions
Beam current
Beam energy
Beam diameter
Precursor
Local precursor flux
Residual gas pressure
Substrate

Postdeposition annealing can improve the metal content for metal-containing deposits, although the treatment generally does not completely remove carbon.

Regarding the precursor chemistry, it is consistently reported that the deposit composition is not directly dependent on the stoichiometric composition of the precursor. For Cu precursors, it is concluded that the thermodynamic stability of the precursor and the electron/precursor flux ratio are the main determining factors for the deposit composition. For other precursors, the electron induced decomposition paths can be very different from those expected from calculations or thermal decomposition. It is consistently reported that elements such as F, N, and Cl easily desorb during deposition. The influence of reactive gases is far from consistent. In a few cases, the metal content significantly improves; in other cases a minor or even no change is observed.

From this review, it becomes clear that several major issues remain. A problem that is encountered when interpreting all the results from literature is the lack of information on the precise experimental conditions. Especially the local gas flux is often not mentioned, while this is important for getting an estimate of the regime in which growth occurred. To be helpful for the understanding of EBID, each report should at least mention the precursor, local precursor flux (in units that allow a calculation of the number of molecules arriving at the irradiated spot per area per time unit), residual gas pressure, beam current, beam diameter, acceleration voltage, and substrate. Ideally, articles are accompanied by a measurement of the deposit height as a function of the current density (or deposited volume as a function of the beam current) to demonstrate the growth regime in which the experiment of interest took place. Table III shows an example of a checklist that can be used. The essential experimental details are given, together with a measurement of the deposit height as a function of the current density (or deposited volume as a function of the beam current, see Fig. 53) and an indication of the growth regime during the described experiments (the arrow in the plot).

Second, the limited understanding of electron induced precursor dissociation is an important issue. The situation in this review is perhaps typical: only about 10% of the pages are dedicated to the precursor chemistry. The precursor chemistry is one of the key factors determining the purity of the deposits and it is exactly the purity of the deposits that is the main limiting factor for a wider application of EBID. Now that elaborate continuum models and Monte Carlo simulations are being developed and a deeper understanding

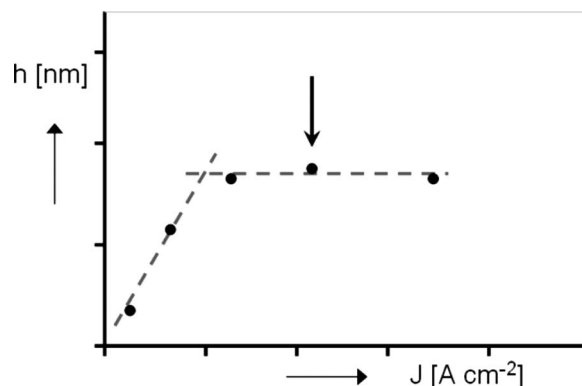


FIG. 53. Growth regime in which the experiment of interest (indicated with an arrow) took place.

of the interplay between physical mechanisms (such as electron scattering, beam induced heating, and the growth regimes) emerges, it is time to develop a better understanding of the precursor chemistry.

It was mentioned that the inconsistencies observed for variations in the PE energy cannot be fully explained. This may be related to the fact that the cross sections for dissociation are unknown. In several cases, a correlation between the vertical growth rate and the SE yield is observed (for variations in the PE energy, the slope dependent proximity effect, and the deposition on a tilted sample). This correlation suggests that the contribution of the SEs is dominant over the contribution of direct dissociation by the PEs, but it is not hard evidence. Hard evidence will be difficult to obtain since cross sections for SE generation and DI of molecules in the gas phase show a similar dependency on the PE energy. If there is a significant contribution of the PEs to the growth, this is expected to occur only in the area irradiated by the PEs. Perhaps the only way to get an indication of the contribution of the PEs is to model the growth of a tip for different PE energies. A comparison between the apex shapes from the model and from real experiments may give insight into the relative contributions of SEs and PEs.

To advance the understanding of EBID in a structural manner, Koops<sup>187</sup> proposed the development of a standardized experiment. In this experiment, deposition is performed under standard conditions with a standard precursor, which gives a common reference frame for future experiments. If inconsistencies still occur, they can be traced more easily to a specific difference between the experiments, thereby leading to a better understanding of the process. Finally, the development of FEBIP into a viable nanofabrication technique would benefit greatly from a “diamond,” a process that yields a deposit with properties that are widely applicable.<sup>187</sup>

## APPENDIX

This Appendix contains Tables IV–VI.

TABLE IV. Precursor names.

Material	Precursor	Full name
Al	TMA	Tri-methyl-aluminum Chloro(trifluorophosphine) gold
Au	AuCl(PF <sub>3</sub> ) <sub>3</sub>	Gold trichloride
Au	AuCl <sub>3</sub>	Gold trichloride
Au	Me <sub>2</sub> -Au-acac	Dimethyl acetylacetonate gold
Au	Me <sub>2</sub> -Au-tfac	Dimethyl-trifluoro- acetylacetonate gold
Au	Me <sub>2</sub> -Au-hfac	Dimethyl-hexafluoro- acetylacetonate gold
C	C <sub>6</sub> H <sub>5</sub> CHCH <sub>2</sub>	Styrene
C	CH <sub>2</sub> CHCOOH	Acrylic acid
C	CH <sub>3</sub> CH <sub>2</sub> COOH	Propionic acid
C	HCOOH	Formic acid
C	CH <sub>3</sub> COOH	Acetic acid
C	CH <sub>3</sub> C <sub>10</sub> H <sub>8</sub>	Alkyl-naphthalene
Co	Co <sub>2</sub> CO <sub>8</sub>	Dicobalt octacarbonyl
Co	(Co(CO) <sub>3</sub> )NO	Cobalt tricarbonyl nitrosyl
Cu	Cu(hfac) <sub>2</sub>	Bis-hexafluoro- acetylacetonate copper
Cu	hfac-Cu-VTMS	Hexafluoro-acetylacetonate copper vinyl-trimethyl- silane
Cu	hfac-Cu-DMB	Hexafluoro-acetylacetonate copper dimethyl-butene
Cu	hfac-Cu-MHY	Hexafluoro-acetylacetonate copper dimethyl- 1-hexen-3-yne
Cr	CrO <sub>2</sub> Cl <sub>2</sub>	Chromyl chloride
Cr	Cr(CO) <sub>6</sub>	Chromium hexacarbonyl
Fe	Fe(CO) <sub>5</sub>	Iron pentacarbonyl
Fe	Fe <sub>3</sub> (CO) <sub>12</sub>	Tri-iron dodecacarbonyl
GaAs	TMG and AsH <sub>3</sub>	Tri-methyl-gallium and arsine
GaN	D <sub>2</sub> GaN <sub>3</sub>	Perdeuterated gallium azide
Ir	(IrCl(PF <sub>3</sub> ) <sub>2</sub> ) <sub>2</sub>	Di- $\mu$ -chloro-tetrakis trifluorophosphine di-iridium
Mo	Mo(CO) <sub>6</sub>	Molybdenum hexacarbonyl
Ni	Ni(C <sub>5</sub> H <sub>5</sub> ) <sub>2</sub>	Nickelocene
Os	Os <sub>3</sub> (CO) <sub>12</sub>	Tri-osmium dodecacarbonyl
Pt	CpPtMe <sub>3</sub>	Trimethyl-platinum- cyclopentadienyl
Pt	MeCpPtMe <sub>3</sub>	Trimethyl-platinum- methylcyclopentadienyl
Pt	Pt(PF <sub>3</sub> ) <sub>4</sub>	Tetrakis trifluorophosphine platinum
Re	Re <sub>2</sub> (CO) <sub>10</sub>	Dirhenium decacarbonyl
Rh	(RhCl(PF <sub>3</sub> ) <sub>2</sub> ) <sub>2</sub>	Di- $\mu$ -chloro-tetrakis trifluorophosphine dirhodium
Rh	(RhCl(CO) <sub>2</sub> ) <sub>2</sub>	Tetracarbonyl di- $\eta$ - chloro dirhodium
Ru	Ru <sub>3</sub> (CO) <sub>12</sub>	Triruthenium dodecacarbonyl
Si	SiH <sub>2</sub> Cl <sub>2</sub>	Dichlorosilane
SiO <sub>x</sub>	TEOS	Tetra-ethoxy-silane
SiO <sub>x</sub>	TMOS	Tetramethyl ortho-silicate
W	W(CO) <sub>6</sub>	Tungsten hexacarbonyl
W	WF <sub>6</sub>	Tungsten hexafluoride
W	WCl <sub>6</sub>	Tungsten hexachloride

TABLE V. Symbols used.

Symbol	Unit	Meaning
$A_{\text{beam}}$	(cm <sup>2</sup> )	Area of the e-beam
$A_{\text{deposit}}$	(cm <sup>2</sup> )	Area of the deposit
$d_{\text{beam}}$	(cm)	Diameter of the e-beam
$d_{\text{deposit}}$	(cm)	Diameter of the deposit
$E_{\text{des}}$	(J)	Desorption energy
$F$	(cm <sup>-2</sup> s <sup>-1</sup> )	Precursor gas flux
$g$		Sticking factor
$h$	(nm)	Deposit height
$I$	(electrons s <sup>-1</sup> )	Current
$J$	(electrons s <sup>-1</sup> cm <sup>-2</sup> )	Total current density
$J_{\text{BSE}}$	(electrons s <sup>-1</sup> cm <sup>-2</sup> )	BSE current density
$J_{\text{PE}}$	(electrons s <sup>-1</sup> cm <sup>-2</sup> )	PE current density
$J_{\text{SE}}$	(electrons s <sup>-1</sup> cm <sup>-2</sup> )	SE current density
$k$	(m <sup>2</sup> kg s <sup>-2</sup> K <sup>-1</sup> )	Boltzmann constant
$\nu$	(s <sup>-1</sup> )	Vibrational frequency of an adsorbed molecule
$N$	(cm <sup>-2</sup> )	Precursor molecule coverage
$N_0$	(cm <sup>-2</sup> )	Available adsorption sites in a monolayer
$P_{\text{partial}}$	Pa	Precursor partial pressure
$P_{\text{equilibrium}}$	Pa	Precursor equilibrium pressure
$Q$	(C)	Accumulated charge
$R$	(cm/s)	Vertical growth rate
$\sigma_{(E)}$	(cm <sup>2</sup> )	Cross section for dissociation
$\sigma$	(cm <sup>2</sup> )	Integral value of $\sigma_{(E)}$
$t$	(s)	Time
$t_{\text{dwell}}$	(s)	Dwell time
$\tau$	(s)	Residence time
$T$	(K)	Temperature
$V_{\text{deposit}}$	(cm <sup>3</sup> )	Volume of a deposit
$V_{\text{molecule}}$	(cm <sup>3</sup> )	Volume of a deposited molecule

TABLE VI. Abbreviations.

Abbreviation	Short for
<i>a</i> -C	Amorphous carbon
BSE	Backscattered electron
DEA	Dissociative electron attachment
DD	Dipolar dissociation
DI	Dissociative ionization
FEBIP	E-beam induced processing
EELS	Electron energy loss spectrometry
e.l.	Electron limited
FSE	Forward scattered electron
PE	Primary electron
p.l.	Precursor limited
SE	Secondary electron
SEM	Scanning electron microscope
STEM	Scanning transmission electron microscope
TEM	Transmission electron microscope
UHV	Ultrahigh vacuum
UV	Ultraviolet

- <sup>1</sup>R. L. Stewart, *Phys. Rev.* **45**, 488 (1934).
- <sup>2</sup>R. W. Christy, *J. Appl. Phys.* **31**, 1680 (1960).
- <sup>3</sup>A. G. Baker and W. C. Morris, *Rev. Sci. Instrum.* **32**, 458 (1961).
- <sup>4</sup>B. Hübner and H. W. P. Koops, *Ultramicroscopy* **42-44**, 1519 (1992).
- <sup>5</sup>C. Schoessler and H. W. P. Koops, *J. Vac. Sci. Technol. B* **16**, 862 (1998).
- <sup>6</sup>I. Utke, P. Hoffmann, R. Berger, and L. Scandella, *Appl. Phys. Lett.* **80**, 4792 (2002).
- <sup>7</sup>I. Utke, T. Bret, D. Laub, Ph. Buffat, L. Scandella, and P. Hoffmann, *Microelectron. Eng.* **73-74**, 553 (2004).
- <sup>8</sup>Y. M. Lau, P. C. Chee, J. T. L. Thong, and V. Ng, *J. Vac. Sci. Technol. A* **20**, 1295 (2002).
- <sup>9</sup>K. I. Schiffmann, *Nanotechnology* **4**, 163 (1993).
- <sup>10</sup>M. Wendel, H. Lorenz, and J. P. Kotthaus, *Appl. Phys. Lett.* **67**, 3732 (1995).
- <sup>11</sup>C. Schössler, J. Urban, and H. W. P. Koops, *J. Vac. Sci. Technol. B* **15**, 1535 (1997).
- <sup>12</sup>K. Edinger, T. Gotszalk, and I. W. Rangelow, *J. Vac. Sci. Technol. B* **19**, 2856 (2001).
- <sup>13</sup>J. H. Kindt, G. E. Fantner, J. B. Thompson, and P. K. Hansma, *Nanotechnology* **15**, 1131 (2004).
- <sup>14</sup>P. Bøggild, T. M. Hansen, O. Kuhn, F. Grey, T. Junno, and L. Montelius, *Rev. Sci. Instrum.* **71**, 2781 (2000).
- <sup>15</sup>K. Mølhave, D. Nørgaard Madsen, A. M. Rasmussen, A. Carlsson, C. C. Appel, M. Brorson, C. J. H. Jacobsen, and P. Bøggild, *Nano Lett.* **3**, 1499 (2003).
- <sup>16</sup>W. Ding, D. A. Dikin, X. Chen, R. D. Piner, R. S. Ruoff, E. Zussman, X. Wang, and X. Li, *J. Appl. Phys.* **98**, 014905 (2005).
- <sup>17</sup>M. F. Yu, O. Lourie, M. J. Dyer, K. Moloni, T. F. Kelly, and R. S. Ruoff, *Science* **287**, 637 (2000).
- <sup>18</sup>T. Fukuda, F. Arai, L. Dong, and M. Nakajima, *Fifth World Congress on Intelligent Control and Automation* **701**, 2698 (2004).
- <sup>19</sup>T. Brintlinger, M. S. Fuhrer, J. Melngailis, I. Utke, T. Bret, A. Perentes, P. Hoffmann, M. Aboudira, and P. Doppelt, *J. Vac. Sci. Technol. B* **23**, 3174 (2005).
- <sup>20</sup>F. Banhart, *Nano Lett.* **1**, 329 (2001).
- <sup>21</sup>P. G. Li, A. Z. Jin, and W. H. Tang, *Phys. Status Solidi A* **203**, 282 (2006).
- <sup>22</sup>M. D. Croitoru, G. Bertsche, D. R. Kern, C. Burkhardt, S. Bauerdick, S. Şahakalkan, and S. Roth, *J. Vac. Sci. Technol. B* **23**, 2789 (2005).
- <sup>23</sup>Y. Tsukatani, N. Yamasaki, K. Murakami, F. Wakaya, and M. Takai, *Jpn. J. Appl. Phys., Part 1* **44**, 5683 (2005).
- <sup>24</sup>L. Rotkina, J. F. Lin, and J. P. Bird, *Appl. Phys. Lett.* **83**, 4426 (2003).
- <sup>25</sup>H. W. P. Koops, R. Weiel, D. P. Kern, and T. H. Baum, *J. Vac. Sci. Technol. B* **6**, 477 (1988).
- <sup>26</sup>K. Edinger, H. Becht, J. Bühr, V. Boegli, M. Budach, T. Hofmann, H. W. P. Koops, P. Kuschnerus, J. Oster, P. Spies, and B. Weyrauch, *J. Vac. Sci. Technol. B* **22**, 2902 (2004).
- <sup>27</sup>T. Liang, E. Frendberg, B. Lieberman, and A. Stivers, *J. Vac. Sci. Technol. B* **23**, 3101 (2005).
- <sup>28</sup>K. Murakami and M. Takai, *J. Vac. Sci. Technol. B* **22**, 1266 (2004).
- <sup>29</sup>M. Weber, M. Rudolph, J. Kretz, and K. W. P. Koops, *J. Vac. Sci. Technol. B* **13**, 461 (1995).
- <sup>30</sup>C. J. Edgcombe and U. Valdre, *Philos. Mag. B* **82**, 987 (2002).
- <sup>31</sup>G. Boero, I. Utke, T. Bret, N. Quack, M. Todorova, S. Mouaziz, P. Keijk, J. Brugger, R. S. Popovic, and P. Hoffmann, *Appl. Phys. Lett.* **86**, 042503 (2005).
- <sup>32</sup>C. P. Umbach, S. Washburn, R. A. Webb, R. Koch, M. Bucci, A. N. Broers, and R. B. Laibowitz, *J. Vac. Sci. Technol. B* **4**, 383 (1986).
- <sup>33</sup>P. Bøggild, T. M. Hansen, C. Tanasa, and F. Grey, *Nanotechnology* **12**, 331 (2001).
- <sup>34</sup>T. Ooi, K. Matsumoto, M. Nakao, M. Otsubo, S. Shirakata, S. Tanaka, and Y. Hatamura, *Proceedings of the IEEE Micro Electro Mechanical Systems (MEMS)*, 2000 (unpublished), p. 580.
- <sup>35</sup>A. Perentes, A. Bachmann, M. Leutenegger, I. Utke, C. Sandu, and P. Hoffmann, *Microelectron. Eng.* **73-74**, 412 (2004).
- <sup>36</sup>H. W. P. Koops, O. E. Hoinkis, M. E. W. Honsberg, R. Schmidt, B. Blum, G. Boettger, A. Kuligk, C. Liguda, and M. Eich, *Microelectron. Eng.* **57-58**, 995 (2001).
- <sup>37</sup>H. W. P. Koops, E. Munro, J. Rouse, J. Kretz, M. Rudolph, M. Weber, and G. Dahm, *Nucl. Instrum. Methods Phys. Res. A* **363**, 1 (1995).
- <sup>38</sup>N. Miura, H. Ishii, J. Shirakashi, A. Yamada, and M. Konagai, *Appl. Surf. Sci.* **113-114**, 269 (1997).
- <sup>39</sup>T. Mukawa, S. Okada, R. Kobayashi, J. Fujita, M. Ishida, T. Ichihashi, Y. Ochiai, T. Kaito, and S. Matsui, *Jpn. J. Appl. Phys., Part 1* **44**, 5639 (2005).
- <sup>40</sup>S. J. Randolph, J. D. Fowlkes, and P. D. Rack, *J. Appl. Phys.* **97**, 124312 (2005).
- <sup>41</sup>N. Silvis-Cividjian and C. W. Hagen, *Adv. Imaging Electron Phys.* **143**, 1 (2006).
- <sup>42</sup>S. J. Randolph, J. D. Fowlkes, and P. D. Rack, *Crit. Rev. Solid State Mater. Sci.* **31**, 55 (2006).
- <sup>43</sup>L. Reimer, *Scanning Electron Microscopy* (Springer-Verlag, Berlin, 1998).
- <sup>44</sup>N. Silvis-Cividjian, "Electron Beam Induced Nanometer Scale Deposition," Ph.D. thesis, Delft University, 2002.
- <sup>45</sup>T. Koshikawa and R. Shimizu, *J. Phys. D* **7**, 1303 (1974).
- <sup>46</sup>M. Kotera, *J. Appl. Phys.* **65**, 3991 (1989).
- <sup>47</sup>D. C. Joy, *Monte Carlo Modeling for Electron Microscopy and Microanalysis* (Oxford University Press, New York, 1995), and references therein.
- <sup>48</sup>C. W. Hagen, N. Silvis-Cividjian, and P. Kruit, *Scanning* **27**, 90 (2005).
- <sup>49</sup>R. F. Egerton, F. Wang, and P. A. Crozier, *Microsc. Microanal.* **12**, 65 (2006).
- <sup>50</sup>P. Rowntree, L. Parenteau, and L. Sanche, *J. Phys. Chem.* **95**, 4902 (1991).
- <sup>51</sup>E. H. Hirsch, *Br. J. Appl. Phys.* **11**, 547 (1960).
- <sup>52</sup>S. Mezheny, I. Lyubinetsky, W. J. Choyke, and J. T. Yates, *J. Appl. Phys.* **85**, 3368 (1999).
- <sup>53</sup>P. M. George and J. L. Beauchamp, *Thin Solid Films* **67**, L25 (1980).
- <sup>54</sup>P. Rowntree, *Chemical Processes of Electron Beam Induced Deposition*, Presented at the First International EBID Workshop, Delft, 2006 (unpublished).
- <sup>55</sup>M. A. Henderson, R. D. Ramsier, and J. T. Yates, *Surf. Sci.* **259**, 173 (1991).
- <sup>56</sup>N. Silvis-Cividjian, C. W. Hagen, L. H. A. Leunissen, and P. Kruit, *Microelectron. Eng.* **61-62**, 693 (2002).
- <sup>57</sup>J. D. Fowlkes, S. J. Randolph, and P. D. Rack, *J. Vac. Sci. Technol. B* **23**, 2825 (2005).
- <sup>58</sup>K. Mitsuishi, Z. Q. Liu, M. Shimojo, M. Han, and K. Furuya, *Ultramicroscopy* **103**, 17 (2005).
- <sup>59</sup>C. Tian and C. R. Vidal, *J. Phys. B* **31**, 895 (1998).
- <sup>60</sup>V. Scheuer, H. W. P. Koops, and T. Tschudi, *Microelectron. Eng.* **5**, 423 (1986).
- <sup>61</sup>T. Ichihashi and S. Matsui, *J. Vac. Sci. Technol. B* **6**, 1869 (1988).
- <sup>62</sup>S. Wang, Y. M. Sun, Q. Wang, and J. M. White, *J. Vac. Sci. Technol. B* **22**, 1803 (2004).
- <sup>63</sup>W. Li and D. C. Joy, *J. Vac. Sci. Technol. A* **24**, 431 (2006).
- <sup>64</sup>A. Folch and J. Servat, *J. Vac. Sci. Technol. B* **14**, 2609 (1996).
- <sup>65</sup>T. Bret, I. Utke, P. Hoffmann, M. Aboudira, and P. Doppelt, *Microelectron. Eng.* **83**, 1482 (2006).
- <sup>66</sup>I. Utke, V. Friedli, J. Michler, T. Bret, X. Multone, and P. Hoffmann, *Appl. Phys. Lett.* **88**, 031906 (2006).
- <sup>67</sup>H. W. P. Koops, J. Kretz, and M. Rudolph, *J. Vac. Sci. Technol. B* **11**, 2386 (1993).
- <sup>68</sup>K. T. Kohlmann-von Platen, J. Chlebek, M. Weiss, and K. Reimer, *J. Vac. Sci. Technol. B* **11**, 2219 (1993).
- <sup>69</sup>Z. Q. Liu, K. Mitsuishi, and K. Furuya, *J. Appl. Phys.* **96**, 3983 (2004).
- <sup>70</sup>U. Hübner, R. Plontke, M. Blume, A. Reinhardt, and H. W. P. Koops, *Microelectron. Eng.* **57-58**, 953 (2001).
- <sup>71</sup>H. Hiroshima and M. Komuro, *Nanotechnology* **9**, 108 (1998).
- <sup>72</sup>D. Beaulieu, Y. Ding, Z. L. Wang, and W. J. Lakey, *J. Vac. Sci. Technol. B* **23**, 2151 (2005).
- <sup>73</sup>P. Hoyle, J. Cleaver, and H. Ahmed, *J. Vac. Sci. Technol. B* **14**, 662 (1996).
- <sup>74</sup>M. Shimojo, W. Zhang, M. Takeguchi, M. Tanaka, K. Mitsuishi, and K. Furuya, *Jpn. J. Appl. Phys., Part 1* **44**, 5651 (2005).
- <sup>75</sup>A. N. Broers, W. W. Molzen, J. J. Cuomo, and N. D. Wittels, *Appl. Phys. Lett.* **29**, 596 (1976).
- <sup>76</sup>H. Jiang, C. N. Borca, B. Xu, and B. W. Robertson, *Int. J. Mod. Phys. B* **15**, 3207 (2001).
- <sup>77</sup>J. Fujita, M. Ishida, T. Ichihashi, Y. Ochiai, T. Kaito, and S. Matsui, *J. Vac. Sci. Technol. B* **21**, 2990 (2003).
- <sup>78</sup>P. A. Crozier, J. Tolle, J. Kouvetakis, and C. Ritter, *Appl. Phys. Lett.* **84**, 3441 (2004).
- <sup>79</sup>O. Guise, J. Ahner, J. Yates, and J. Levy, *Appl. Phys. Lett.* **85**, 2352 (2004).
- <sup>80</sup>M. Tanaka, M. Shimojo, M. Han, K. Mitsuishi, and K. Furuya, *Surf. Interface Anal.* **37**, 261 (2005).
- <sup>81</sup>W. F. Van Dorp, B. Van Someren, C. W. Hagen, P. Kruit, and P. A. Crozier, *Nano Lett.* **5**, 1303 (2005).
- <sup>82</sup>W. F. Van Dorp, B. Van Someren, C. W. Hagen, P. A. Crozier, and P. Kruit,

- Microelectron. Eng.* **83**, 1468 (2006).
- <sup>83</sup>H. W. P. Koops, J. Kretz, M. Rudolph, M. Weber, G. Dahm, and K. L. Lee, *Jpn. J. Appl. Phys., Part 1* **33**, 7099 (1994).
- <sup>84</sup>H. W. P. Koops, A. Kaya, and M. Weber, *J. Vac. Sci. Technol. B* **13**, 2400 (1995).
- <sup>85</sup>M. Weber, H. W. P. Koops, M. R. Rudolph, J. Kretz, and G. Schmidt, *J. Vac. Sci. Technol. B* **13**, 1364 (1995).
- <sup>86</sup>T. Bret, "Physico-chemical study of the focused electron beam induced deposition process," Ph.D. thesis, Ecole Polytechnique Fédérale de Lausanne, 2005.
- <sup>87</sup>I. Utke, J. Michler, P. Gasser, C. Santschi, D. Laub, M. Cantoni, P. A. Buffat, C. Jiao, and P. Hoffmann, *Adv. Eng. Mater.* **7**, 323 (2005).
- <sup>88</sup>R. R. Kunz and T. M. Mayer, *J. Vac. Sci. Technol. B* **6**, 1557 (1988).
- <sup>89</sup>C. Schöbller, A. Kaya, J. Kretz, and H. W. P. Koops, *Microelectron. Eng.* **30**, 471 (1996).
- <sup>90</sup>K. T. Kohlmann-von Platen, L.-M. Buchman, H.-C. Petzold, and W. H. Brünger, *J. Vac. Sci. Technol. B* **10**, 2690 (1992).
- <sup>91</sup>M. A. Bruk, E. N. Zhikharev, E. I. Grigor'ev, A. V. Spirin, V. A. Kal'nov, and I. E. Kardash, *High Energy Chem.* **39**, 65 (2005).
- <sup>92</sup>I. Utke, P. Hoffmann, B. Dwir, K. Leifer, E. Kapon, and P. Doppelt, *J. Vac. Sci. Technol. B* **18**, 3168 (2000).
- <sup>93</sup>M. Komuro and H. Hiroshima, *Microelectron. Eng.* **35**, 273 (1997).
- <sup>94</sup>H. Seiler, *J. Appl. Phys.* **54**, R1 (1983).
- <sup>95</sup>B. Völkel, A. Götzhäuser, H. U. Müller, C. David, and M. Grunze, *J. Vac. Sci. Technol. B* **15**, 2877 (1997).
- <sup>96</sup>S. Lipp *et al.*, S. Bauerdick *et al.*, D. Beaulieu *et al.*, M. D. Croitoru *et al.*, and K. T. Kohlmann-von Platen *et al.* report a change in beam current when changing the PE energy; P. Hoyle *et al.*, K. T. Kohlmann-von Platen *et al.*, S. J. Randolph *et al.*, K. I. Schifffmann *et al.*, and N. Miura *et al.* have performed their experiments at a constant beam current, but reported a change in the beam diameter when varying the PE energy.
- <sup>97</sup>T. Bret, I. Utke, A. Bachmann, and P. Hoffmann, *Appl. Phys. Lett.* **83**, 4005 (2003).
- <sup>98</sup>S. Wang, Y. M. Sun, and J. M. White, *Appl. Surf. Sci.* **249**, 110 (2005).
- <sup>99</sup>P. Hoyle, J. Cleaver, and H. Ahmed, *Appl. Phys. Lett.* **64**, 1448 (1994).
- <sup>100</sup>M. Takai, W. Jarupoonphol, C. Ochiai, O. Yavas, and Y. K. Park, *Appl. Phys. A: Mater. Sci. Process.* **76**, 1007 (2003).
- <sup>101</sup>S. Bauerdick, C. Burkhardt, R. Rudolf, W. Barth, V. Bucher, and W. Nisch, *Microelectron. Eng.* **67-68**, 963 (2003).
- <sup>102</sup>S. Lipp, L. Frey, C. Lehrer, E. Demm, S. Pauthner, and H. Ryssel, *Microelectron. Reliab.* **36**, 1779 (1996).
- <sup>103</sup>D. Kunze, O. Peters, and G. Sauerbrey, *Z. Angew. Phys.* **22**, 69 (1967).
- <sup>104</sup>K. L. Lee and M. Hatzakis, *J. Vac. Sci. Technol. B* **7**, 1941 (1989).
- <sup>105</sup>M. Fischer, H. D. Wanzelboeck, J. Gottsbachner, S. Mueller, W. Brezna, M. Schramboeck, and E. Bertagnolli, *Microelectron. Eng.* **83**, 784 (2006).
- <sup>106</sup>N. Miura, H. Ishii, A. Yamada, and M. Konagai, *Jpn. J. Appl. Phys., Part 2* **35**, L1089 (1996).
- <sup>107</sup>D. A. Bell, J. L. Falconer, Z. Lü, and C. M. McConica, *J. Vac. Sci. Technol. B* **12**, 2976 (1994).
- <sup>108</sup>F. Cicoira, P. Hoffmann, C. O. A. Olsson, N. Xanthopoulos, H. J. Mathieu, and P. Doppelt, *Appl. Surf. Sci.* **242**, 107 (2005).
- <sup>109</sup>V. Gopal, E. A. Stach, V. R. Radmilovic, and I. A. Mowat, *Appl. Phys. Lett.* **85**, 49 (2004).
- <sup>110</sup>J. Fourie, *Optik (Jena)* **44**, 111 (1975).
- <sup>111</sup>L. Reimer and M. Wächter, *Ultramicroscopy* **3**, 169 (1978).
- <sup>112</sup>I. Utke, V. Friedli, and J. Michler, "Resolution and Growth Regimes in Focused Ion and Electron Beam Induced Processing," *J. Vac. Sci. Technol. B* (submitted).
- <sup>113</sup>D. A. Smith, J. D. Fowlkes, and P. D. Rack, *Nanotechnology* **18**, 265308 (2007).
- <sup>114</sup>M. Amman, J. Sleight, D. Lombardi, R. Welser, and M. Deshpande, *J. Vac. Sci. Technol. B* **14**, 54 (1996).
- <sup>115</sup>I. Utke, A. Luisier, P. Hoffmann, D. Laub, and P. A. Buffat, *Appl. Phys. Lett.* **81**, 3245 (2002).
- <sup>116</sup>Z. Q. Liu, K. Mitsuishi, and K. Furuya, *Appl. Phys. A: Mater. Sci. Process.* **80**, 1437 (2005).
- <sup>117</sup>F. Cicoira, K. Leifer, P. Hoffmann, I. Utke, B. Dwir, D. Laub, P. A. Buffat, E. Kapon, and P. Doppelt, *J. Cryst. Growth* **265**, 619 (2004).
- <sup>118</sup>S. Lipp, L. Frey, C. Lehrer, B. Frank, E. Demm, S. Pauthner, and H. Ryssel, *J. Vac. Sci. Technol. B* **14**, 3920 (1996).
- <sup>119</sup>E. J. Sanchez, J. T. Krug II, and X. S. Xie, *Rev. Sci. Instrum.* **73**, 3901 (2002).
- <sup>120</sup>P. Hoyle, M. Ogasawara, and J. Cleaver, *Appl. Phys. Lett.* **62**, 3043 (1993).
- <sup>121</sup>T. Utke, B. Dwir, K. Leifer, F. Cicoira, P. Doppelt, P. Hoffmann, and E. Kapon, *Microelectron. Eng.* **53**, 261 (2000).
- <sup>122</sup>K. Møjlhave, D. Nørgaard Madsen, S. Dohn, and P. Bøggild, *Nanotechnology* **15**, 1047 (2004).
- <sup>123</sup>S. Okada, T. Mukawa, R. Kobayashi, J. Fujita, M. Ishida, T. Ichihashi, Y. Ochiai, T. Kaito, and S. Matsui, *Jpn. J. Appl. Phys., Part 1* **44**, 5646 (2005).
- <sup>124</sup>T. Bret, I. Utke, C. Gaillard, and P. Hoffmann, *J. Vac. Sci. Technol. B* **22**, 2504 (2004).
- <sup>125</sup>A. Luisier, I. Utke, T. Bret, F. Cicoira, R. Hauert, S.-W. Rhee, P. Doppelt, and P. Hoffmann, *J. Electrochem. Soc.* **151**, C535 (2004).
- <sup>126</sup>J. Y. Igaki, K. Kanda, Y. Haruyama, M. Ishida, Y. Ochiai, J. Fujita, T. Kaito, and S. Matsui, *Microelectron. Eng.* **83**, 1225 (2006).
- <sup>127</sup>Z. Q. Liu, K. Mitsuishi, and K. Furuya, *J. Appl. Phys.* **96**, 619 (2004).
- <sup>128</sup>M. Han, K. Mitsuishi, M. Shimojo, and K. Furuya, *Philos. Mag.* **84**, 1281 (2004).
- <sup>129</sup>T. Bret, I. Utke, and P. Hoffmann, *Microelectron. Eng.* **78-79**, 307 (2005).
- <sup>130</sup>W. Zhang, M. Shimojo, M. Takeguchi, R. C. Che, and K. Furuya, *Adv. Eng. Mater.* **8**, 711 (2006).
- <sup>131</sup>V. Gopal, V. R. Radmilovic, C. Daraio, S. Jin, P. Yang, and E. A. Stach, *Nano Lett.* **4**, 2059 (2004).
- <sup>132</sup>J. P. Martin and R. Speidel, *Optik (Jena)* **1**, 13 (1972).
- <sup>133</sup>V. Aristov, N. Kislov, and I. Khodos, *Microsc. Microanal. Microstruct.* **3**, 313 (1992).
- <sup>134</sup>W. F. Van Dorp, S. Lazar, C. W. Hagen, and P. Kruit, *J. Vac. Sci. Technol. B* **25**, 1603 (2007).
- <sup>135</sup>V. V. Aristov, A. Y. Kasumov, N. A. Kislov, O. V. Kononenko, and V. N. Matveev, *Nanotechnology* **6**, 35 (1995).
- <sup>136</sup>K. Mitsuishi, M. Shimojo, M. Takeguchi, M. Tanaka, and K. Furuya, *Jpn. J. Appl. Phys., Part 1* **45**, 5517 (2006).
- <sup>137</sup>S. Ketharanathan, R. Sharma, and J. Drucker, *J. Vac. Sci. Technol. B* **23**, 2403 (2005).
- <sup>138</sup>W. Zhang, M. Shimojo, M. Takeguchi, and K. Furuya, *J. Mater. Sci.* **41**, 2577 (2006).
- <sup>139</sup>F. Zaera, *Langmuir* **7**, 1188 (1991).
- <sup>140</sup>R. R. Kunz and T. M. Mayer, *Appl. Phys. Lett.* **50**, 962 (1987).
- <sup>141</sup>G. A. West and K. W. Beeson, *Appl. Phys. Lett.* **53**, 740 (1988).
- <sup>142</sup>S. Matsui and K. Mori, *J. Vac. Sci. Technol. B* **4**, 299 (1986).
- <sup>143</sup>A. Ishibashi, K. Funato, and Y. Mori, *J. Vac. Sci. Technol. B* **9**, 169 (1991).
- <sup>144</sup>T. Takahashi, Y. Arakawa, M. Nishioka, and T. Ikoma, *J. Cryst. Growth* **124**, 213 (1992).
- <sup>145</sup>M. Tanaka, F. Chu, M. Shimojo, M. Takeguchi, K. Mitsuishi, and K. Furuya, *J. Mater. Sci.* **41**, 2667 (2006).
- <sup>146</sup>M. Tanaka, M. Han, M. Takeguchi, F. Chu, M. Shimojo, K. Mitsuishi, and K. Furuya, *Jpn. J. Appl. Phys., Part 1* **44**, 5635 (2005).
- <sup>147</sup>Y. Ochiai, J. Fujita, and S. Matsui, *J. Vac. Sci. Technol. B* **14**, 3887 (1996).
- <sup>148</sup>H. W. P. Koops, C. Schöbller, A. Kaya, and M. Weber, *J. Vac. Sci. Technol. B* **14**, 4105 (1996).
- <sup>149</sup>O. Yavas, C. Ochiai, M. Takai, Y. K. Park, C. Lehrer, S. Lipp, L. Frey, H. Ryssel, A. Hosono, and S. Okuda, *J. Vac. Sci. Technol. B* **18**, 976 (2000).
- <sup>150</sup>S. Frabboni, G. C. Gazzadi, and A. Spessot, *Appl. Phys. Lett.* **89**, 113108 (2006).
- <sup>151</sup>M. Takeguchi, M. Shimojo, and K. Furuya, *Nanotechnology* **16**, 1321 (2005).
- <sup>152</sup>M. Takeguchi, M. Shimojo, and K. Furuya, *Jpn. J. Appl. Phys., Part 1* **44**, 5631 (2005).
- <sup>153</sup>M. Shimojo, M. Takeguchi, M. Tanaka, K. Mitsuishi, and K. Furuya, *Appl. Phys. A: Mater. Sci. Process.* **79**, 1869 (2004).
- <sup>154</sup>O. Guise, H. Marbach, J. Levy, J. Ahner, and J. T. Yates, *Surf. Sci.* **571**, 128 (2004).
- <sup>155</sup>N. A. Kislov, I. I. Khodos, E. D. Ivanov, and J. Barthel, *Scanning* **18**, 114 (1996).
- <sup>156</sup>T. Ichihashi, J. Fujita, M. Ishida, and Y. Ochiai, *Phys. Rev. Lett.* **92**, 215702 (2004).
- <sup>157</sup>C. H. Jin, J. Y. Wang, Q. Chen, and L.-M. Peng, *J. Phys. Chem. B* **110**, 5423 (2006).
- <sup>158</sup>P. A. Crozier, private communication (2007).
- <sup>159</sup>M. Komuro, H. Hiroshima, and A. Takechi, *Nanotechnology* **9**, 104 (1998).
- <sup>160</sup>K. Murakami, N. Yamasaki, S. Abo, F. Wakaya, and M. Takai, *J. Vac. Sci. Technol. B* **23**, 759 (2005).

- <sup>161</sup>I. Utke, F. Cicoira, G. Jaenchen, P. Hoffmann, L. Scandella, B. Dwir, E. Kapon, D. Laub, Ph. Buffat, N. Xanthopoulos, and H. J. Mathieu, MRS Symposia Proceedings No. 706 (Materials Research Society, Pittsburgh, 2000), p. 307.
- <sup>162</sup>S. Matsui and I. Toshinari, *J. Vac. Sci. Technol. B* **7**, 1182 (1989).
- <sup>163</sup>D. C. Joy, A Database of Electron-Solid Interactions, <http://web.utk.edu/~srcutk/htm/interact.htm>
- <sup>164</sup>K. Ueda and M. Yoshimura, *Thin Solid Films* **464–465**, 331 (2004).
- <sup>165</sup>K. Mitsuishi, M. Shimojo, M. Han, and K. Furuya, *Appl. Phys. Lett.* **83**, 2064 (2003).
- <sup>166</sup>Z. Q. Liu, K. Mitsuishi, and K. Furuya, *Nanotechnology* **17**, 3832 (2006).
- <sup>167</sup>M. Song, K. Mitsuishi, M. Tanaka, M. Takeguchi, M. Shimojo, and K. Furuya, *Appl. Phys. A: Mater. Sci. Process.* **80**, 1431 (2005).
- <sup>168</sup>M. H. Song, K. Mitsuishi, and K. Furuya, *Mater. Sci. Forum* **475–479**, 4035 (2005).
- <sup>169</sup>G. Q. Xie, M. H. Song, K. Mitsuishi, and K. Furuya, *J. Mater. Sci.* **41**, 2567 (2006).
- <sup>170</sup>G. Q. Xie, M. H. Song, and K. Furuya, *J. Mater. Sci.* **41**, 4537 (2006).
- <sup>171</sup>F. Banhart, *Phys. Rev. E* **52**, 5156 (1995).
- <sup>172</sup>H. Z. Wang, X. H. Liu, X. J. Yang, and X. Wang, *Mater. Sci. Eng., A* **311**, 180 (2001).
- <sup>173</sup>C. W. Hagen, W. F. Van Dorp, and P. A. Crozier, *The Nucleation Stage in Electron Beam Induced Deposition*, Proceedings of EMAG '07, Institute of Physics Conference Series (IOP, Bristol, 2007).
- <sup>174</sup>P. Hoffmann, *Precursors for Focused Electron Beam Induced Deposition*, Presentation at the First International EBID Workshop, Delft, 2006 (unpublished).
- <sup>175</sup>D. A. Bell, C. M. McConica, J. L. Falconer, and Z. Lü, *J. Electrochem. Soc.* **141**, 2884 (1994).
- <sup>176</sup>P. Hoffmann and P. A. Crozier, private communication (2005).
- <sup>177</sup>M. Shimojo, S. Bysakh, K. Mitsuishi, M. Tanaka, M. Song, and K. Furuya, *Appl. Surf. Sci.* **241**, 56 (2005).
- <sup>178</sup>T. Bret, S. Mauron, I. Utke, and P. Hoffmann, *Microelectron. Eng.* **78–79**, 300 (2005).
- <sup>179</sup>P. Seuret, F. Cicoira, T. Ohta, P. Doppelt, J. Weber, and T. A. Wesolowski, *Phys. Chem. Chem. Phys.* **5**, 268 (2003).
- <sup>180</sup>P. Doppelt, V. Weigel, and P. Guinot, *Mater. Sci. Eng., B* **17**, 143 (1993).
- <sup>181</sup>A. R. Ivanova, G. Nuesca, X. Chen, C. Goldberg, A. E. Kaloyeros, B. Arkles, and J. J. Sullivan, *J. Electrochem. Soc.* **146**, 2139 (1999).
- <sup>182</sup>M. Hoshino, K. Kasai, and J. Komeno, *Jpn. J. Appl. Phys., Part 1* **31**, 4403 (1992).
- <sup>183</sup>A. Folch, J. Tejada, C. H. Peters, and M. S. Wrighton, *Appl. Phys. Lett.* **66**, 2080 (1995).
- <sup>184</sup>A. A. Tseng, *Nanofabrication: Fundamentals and Applications* (World Scientific, Singapore, 2007).
- <sup>185</sup>K. T. Kohlmann, L. M. Buchmann, and W. H. Brünger, *Microelectron. Eng.* **17**, 427 (1992).
- <sup>186</sup>I. Utke, V. Friedli, S. Amorosi, J. Michler, and P. Hoffmann, *Microelectron. Eng.* **83**, 1499 (2006).
- <sup>187</sup>H. W. P. Koops, *A Story About the Past and the Present of Electron Beam Induced Deposition*, Presented at the First International EBID Workshop, Delft, 2006 (unpublished).